# ANALYZING GROWTH, HYGROSCOPICITY AND CLIMATE EFFECTS OF ATMOSPHERIC PARTICLES AT THE ARM SGP SITE

A Dissertation

by

MANASI MAHISH

Submitted to the Office of Graduate and Professional Studies of
Texas A&M University
in partial fulfillment of the requirements for the degree of

DOCTOR OF PHILOSOPHY

| | |
|---|---|
| Chair of Committee, | Don Collins |
| Committee Members, | Sarah Brooks |
| | Renyi Zhang |
| | Qi Ying |
| Head of Department, | Ping Yang |

August 2017

Major Subject: Atmospheric Sciences

# ABSTRACT

Particle size and size resolved hygroscopicity distributions measured at the ARM SGP site from 2009 to 2012 were used to study new particle formation (NPF) and subsequent growth, variation in hygroscopicity and mixing state with time of day and year, upscatter fraction (β) and other optical properties, and the factors influencing estimates of the concentration of cloud condensation nuclei ($N_{CCN}$).

New particles were formed frequently between March and October in 2009, but those that formed grew faster from June to August. Usually particles between 12 nm and 22 nm grew faster in the afternoon when the gas phase precursor concentrations and photochemical reaction rates are expected to be higher. A two-component condensable gas model I developed describes the observed pattern, attributing daytime growth to higher concentration of hygroscopic inorganic and organic species and nighttime growth primarily to condensation of organics. Among three evaluated time-spans, the hygroscopicity parameter, *k*, was highest during the daytime and was relatively higher at night for particles <100 nm. It was also higher for particles < 100 nm during days and nights on which NPF events were observed. On average, particles at the small and large tails of the measured size range had higher *k* due to higher inorganic content. Among the 7 particle sizes the minimum hygroscopicity was observed at an intermediate size (~50nm), which is thought to have higher organic content. A similar pattern was observed in fitted and categorized GF distribution modes, with the additional observation of frequently nearly-hydrophobic particle modes throughout the size range.

Aerosol mixing state was quantified as the standard deviation (SD) of each GF distribution and a size-dependent threshold SD selected to roughly separate internal and external mixtures. The results show an increased frequency of internal mixtures during the daytime and during the summer when photochemistry and precursor emissions are highest.

The effect of aerosols on climate is connected to the fraction of incoming solar radiation scattered into the upward hemisphere and back into space, β, and to $N_{CCN}$. Calculated boundary layer β was highest around sunset and during winter. Aerosol optical properties including β were parameterized using size and GF distributions, solar position, and RH. $N_{CCN}$ for a supersaturation (S) range of 0.25 to 0.85% was calculated using a base model that incorporates all of the information from the size and GF distributions. The results of those base model estimates were compared to directly measured $N_{CCN}$, with average fractional errors of 0.21, 0.23, and 0.28 for 2010, 2011, and 2012, respectively. The results were then compared with estimates based on simplified treatment of the aerosol composition and mixing state. Among all simplifications considered, assuming the aerosol is an internal mixture with size-dependent soluble fraction was the best alternative for base model. The $N_{CCN}$ above 0.3% S was also parameterized reasonably well ($r^2 = 0.87$) using the integrated particle concentration between 50 and 500 nm and S.

# DEDICATION

I dedicate my dissertation to my son, who made me believe that small is BIG!

# ACKNOWLEDGEMENTS

I take this opportunity to thank my advisor Dr. Don Collins, whose constant guidance and support have led me to the right direction and helped greatly in achieving insight into my research. I am also grateful to have Dr. Qi Ying, Dr. Renyi Zhang, and Dr. Sarah Brooks as my committee members. I acknowledge the assistance from my research group, especially Chance Spencer and Nathan Taylor. Also I owe to Dr. Anne Jefferson for providing CCN data, Alison Tilp for helping me out in data archiving, and, ARM SGP personnel who look after our instruments at the site. Besides, there are so many other people who touched and shaped my life to make me what I am today. I cannot appreciate enough all my teachers from childhood, especially primary school principal Sabitri Sinha, secondary school teacher Chandana Dutta, and, tutor Tapas Garai, who believed in me and coached me without charging a penny. I also feel very fortunate to have friends who always stand by me during tough times. Finally, I thank my parents and my husband for their unconditional love, constant support and sacrifices.

# CONTRIBUTORS AND FUNDING SOURCES

## Contributors

This work was supervised by a dissertation committee consisting of Dr. Don Collins, Dr. Sarah Brooks and Dr. Renyi Zhang of the Department of Atmospheric Sciences and Dr. Qi Ying of the Department of Civil and Environmental Engineering.

All work for the dissertation was completed by the student, under the advisement of Dr. Don Collins of the Department of Atmospheric Sciences.

## Funding Sources

This research was supported by the office of biological and environmental research of the U.S. Department of Energy under grant DE-SC0016051 as part of the Atmospheric Radiation Measurement (ARM) climate research facility, an office of science scientific user facility

Its contents are solely the responsibility of the authors and do not necessarily represent the official views of the U.S. Department of Energy.

# NOMENCLATURE

| | |
|---|---|
| $A_{bulk,\ AS}$ | Bulk activation ratio of pure ammonium sulfate aerosol |
| $A_{Bulk,\ tot}$ | Bulk activation ratio |
| $A_{bulk,acc}$ | Bulk activation ratio of accumulation mode particles |
| ACSM | Aerosol Chemical Speciation Monitor |
| AN | Ammonium nitrate |
| AOD | Aerosol optical depth |
| AOS | Aerosol Observing System |
| AR | Activation ratio |
| ARM | Atmospheric Radiation Measurement |
| AS | Ammonium sulfate |
| $b_{back}$ | Backscattering coefficient |
| $b_{backscat}$ | Backscattering coefficient |
| BBOA | Biomass burning organic aerosol |
| BC | Black carbon |
| $b_{ext}$ | Extinction coefficient |
| $b_{h.back}$ | Hemispheric backscattering coefficient |
| $b_{scat}$ | Total scattering coeeficient |
| $b_{ups}$ | Upscattering coefficient |
| CCN | Cloud condensation nuclei |
| $CCN_C$ | Cloud condensation nuclei counter |

| | |
|---|---|
| CL | Condensation level |
| CLAP | Continuous light absorption photometer |
| CPC | Condensation particle counter |
| CSPHOT | Cimel sun photometer |
| D | Diameter |
| $D_{drop}$ | Droplet diameter |
| DMA | Differential mobility analyzer |
| DOE | Department of energy |
| DRH | Deliquescence RH |
| e | Actual vapor pressure |
| $e_s$ | Saturation vapor pressure |
| $f_i(\neq D)$ | Size-independent particle-type fractions |
| $f_i(D)$ | Size-dependent particle-type fractions |
| GF | Growth Factor |
| GF-PDF | Growth factor probability density functions |
| GHG | Greenhouse gases |
| GR | Growth rate |
| $H_2SO_4$ | Sulfuric acid |
| HGF | Hygroscopic growth factor |
| $h_{LCL}$ | Lifting condensation level height |
| HTDMA | Hygroscopic tandem mobility analyzer |
| k | Hygroscopicity parameter, kappa |

| | |
|---|---|
| $k_{org}$ | kappa of organics |
| MLH | Mixing Layer Height |
| MO-OOA | More-oxidized oxygenated organic aerosols |
| $MS_{hyg}$ | Hygroscopicity-based mixing state value |
| $N_{CCN}$ | Number concentration of cloud condensation nuclei |
| $N_{CN}$ | Number concentration of total particle |
| $N_{in}$ | Number concentration of insoluble particle |
| $N_{inorg}$ | Number concentration of inorganic particle |
| $N_{org}$ | Number concentration of soluble organic particle |
| NPF | New particle formation |
| NRMSE | Normalized Root Mean Square Error |
| OACOMP | Organic Aerosol Component |
| $org_{NR}$ | Non-refractory organics |
| PC | Principal component |
| PCA | Principal component analysis |
| PMF | Positive Matrix Factorization |
| RH | Relative humidity |
| S | Supersaturation |
| $S_c$ | Critical supersaturation |
| SD | Standard deviations |
| $SD_{10\%}$ | SD at 10% cumulative frequency |
| $SD_{int/ext}$ | Reference SD separating internal and external mixing state |

| | |
|---|---|
| $SD_{measurement}$ | SD from measurement |
| SF | Soluble fraction |
| SF(≠D) | Size-independent soluble fraction |
| SF(D) | Size-dependent soluble fraction |
| SGP | Southern Great Plain |
| SMPS | Scanning mobility particle sizer |
| SOA | Secondary organic aerosol |
| T | Air temperature |
| $T_d$ | Dew point temperature |
| VAP | Value Added Product |
| VOC | Volatile organic carbon |
| $V_{overall}$ | Particle volume concentration |
| $\beta$ | Upscatter fraction |
| $\Gamma$ | Dry adiabatic lapse rate |
| $\Gamma_d$ | Dew point lapse rate |
| $\theta_0$ | Solar zenith angle |
| $\varphi$ | Solar elevation |

TABLE OF CONTENTS

Page

LIST OF FIGURES

Page

LIST OF TABLES

Page

# CHAPTER I

# INTRODUCTION

The influence of atmospheric particles on climate can be broadly categorized into their direct and indirect effects. The direct effect describes attenuation of solar radiation due to scattering and absorption by particles. The indirect effect describes modification of cloud properties by those particles with size- and composition-dependent critical supersaturation ($S_c$) below the peak supersaturation, S, within a cloud. The extent of these effects depends on particle concentration, size, and composition.

Particles are introduced into the atmosphere either by direct emission or by formation of new particles (new particle formation or NPF), which follows from photochemical production of low volatility gas phase species. NPF and subsequent growth occur in diverse environments including coastal regions [*Weber et al*., 1998], urban environments [*Stanier et al.,* 2004], rural environments, forests [*Tunved et al.*, 2006; *Juuti et al.*, 2011; *Perrington et al.*, 2013], mountainous regions [*Weber et al.* 1997], and the Arctic [*Pirjola et al.* 1998]. Growth of the newly formed particles occurs primarily due to condensation of low volatility gases, with additional contributions from secondary growth channels such as coagulation and heterogeneous reactions [*Zhang et al.*, 2011]. Though sulfuric acid usually plays a key role in condensational growth [*Kuang et al*., 2007], semi-, low-, and extremely-low-volatile organic compounds can be even more important as, for example, is observed over the forested region of Hyytiälä, Finland [*Juuti et al.*, 2011]. The average growth rate of ultrafine particles is a function of

the particle size and the precursor concentration. Precursor concentration is usually higher around midday due to heightened photochemical activities. Combination of these two often causes daytime increase in growth rate in proportion with size for smaller particles [*Manninen et al*., 2010; *Juuti et al.*, 2011].

Particles composed of soluble inorganic species (e.g., ammonium, sulfate, nitrate, chloride) are generally more hygroscopic than those composed of organics, which exhibit a range in hygroscopicity with some being slightly hygroscopic [*Saxena and Hildemann*, 1996; *Zappoli et al.*, 1999; *Peng et al.*, 2001; *Svenningsson et al.*, 2006; *King et al.*, 2007; *Prenni et al.*, 2007; *Duplissy et al.*, 2008; *Smith et al.*, 2008; *Engelhart et al.*, 2008; *Gunthe et al.*, 2009; *Juranyi et al.*, 2009; *King et al.*, 2009; *King et al.*, 2010.; *Juuti et al.*, 2011] and others non-hygroscopic [*Abbatt et al.*, 2005; *Prenni et al.*, 2007]. Additionally, organic compounds can reduce water uptake of some inorganic species present in the same particles [*Cruz et al.*, 2000; *Dick et al.*, 2000; *Choi et al.*, 2002; *Hersey et al.*, 2009; *Meyer et al.*, 2009]. Despite this complex behavior, the effect of organics on the hygroscopicity of multi-component aerosols often can be explained by the simple ZSR mixing rule for RH > deliquescence RH (DRH) [*Jing et al.*, 2016; *Peng et al.*, 2016]. This enables use of measured hygroscopic growth factor (GF), which is the ratio of the size of a particle at high RH to its dry size, as a rough proxy for particle type [*McMurry and Stolzenburg*, 1989; *Zhang et al.*, 1993; *Gysel et al.*, 2007], with higher GF indicating a higher soluble inorganic content and lower GF indicating a higher content of organics and/or insoluble components such as soot and dust. The finding of higher GF in larger particles at various locations can thus be interpreted as the result of

higher inorganic fraction and lower GF in smaller particles as the result of higher organic fraction [*Gasparini et al.*, 2006; *Holmgren et al.*, 2014; *Levin et al.*; 2014]. GF data are also useful in categorization of aerosols in different hygroscopicity groups and in quantifying aerosol mixing state from growth factor probability density functions (GF-PDFs). *Holmgren et al.* [2014] reported use of such GF-PDFs to describe aerosol mixing state with a key finding that external mixtures are more frequent during autumn and winter for accumulation mode particles.

The temporal variation in aerosol hygroscopicity often displays a diel pattern, which may have different explanations based on site location. For instance, aerosol hygroscopicity was higher during the day in the boreal forest in Hyytiälä, southern Finland [*Ehn et al.*, 2007] mainly due to higher gas phase concentration of sulfuric acid, higher biogenic emissions, and active photochemistry. A similar pattern was observed at a polluted site in the North China Plain [*Liu et al.*, 2011], though the cause differed somewhat and was attributed largely to aerosol aging. A contrasting pattern of higher nighttime hygroscopicity linked with boundary layer dynamics and long range transport was observed at a high altitude site in Puy de Dôme, France [*Holmgren et al.*, 2014].

After growing to ~50 – 100 nm, particles impact the earth's radiative balance by absorbing and/or scattering sunlight and by acting as cloud condensation nuclei (CCN). Considering the great but uncertain impact they have on the atmosphere, it is important to directly measure and incorporate into models both their optical and cloud droplet forming properties. Aerosol optical properties are often derived using data from ground based instruments such as Cimel Sun Photometers (CSPHOT), Continuous Light

Absorption Photometers (CLAP), nephelometers, and micropulse and Raman lidars. Alternatively, Mie theory / Mie-Debye-Lorenz theory [*Bohren and Huffman*, 1983] can be used to describe the optical behavior of particles of known size and composition.

The CCN concentration ($N_{CCN}$) can be measured directly with CCN counters (CCNc), in which the sample stream is exposed to one or more pre-determined supersaturations inside a flow column [*Ross et al.*, 2003; *Rose et al.*, 2008; *Liu et al.*, 2011]. Even with recent availability of robust counters, direct measurement of $N_{CCN}$ is limited. Moreover, prediction of $N_{CCN}$ in models requires an understanding of the link between aerosol properties and $S_c$ that is not easily assessed from only measured concentrations. Thus, it can be both valuable and convenient to estimate it using measured or modeled aerosol characteristics. Early efforts employed the power law formula (i.e., $Cs^k$, where C and k are region based parameters) to calculate $N_{CCN}$ [*Twomey*, 1959; *Ji and Shaw*, 1998], though sometimes without much success [*Deng et al.*, 2013; *Jefferson et al.*, 2010]. Use of the bulk activation ratio (the ratio of measured $N_{CCN}$ at certain %S to measured total aerosol number concentration ($N_{CN}$)) has resulted in significant disagreement between measured and empirically derived $N_{CCN}$, because of variation in reference size range, chemical composition and S [*Pruppacher and Klett*, 1977; *Roberts et al.* 2002; *Rose et al.*, 2010; *Bougiatioti et al.*, 2009; *Deng et al.*, 2013]. Constraining the size range of $N_{CN}$ [*Ross et al.*, 2003; *Breed et al.*, 2002; *Deng et al.*, 2013] or assuming the particles are composed of pure salt improved the outcome to some extent [*Deng et al.*, 2013]. Several measured aerosol optical properties such as aerosol optical depth (AOD), extinction coefficient, and scattering coefficient have also

been used to estimate $N_{CCN}$ [*Ghan and Collins*, 2004; *Ghan et al.*, 2006; *Andrea et al.*, 2009; *Quaas et al.*, 2009; *Shinozuka et al.*, 2009; *Jefferson*, 2010; *Liu et al.*, 2011; *Wang et al.*, 2011; *Tao et al.*, 2012; *Grandey et al.*, 2013]. Although mathematically complex, Köhler Theory can be used to determine the $S_c$ of inorganic particles with known physico-chemical properties [*Köhler*, 1936]. Modification of Köhler Theory to include the effect of solubility and surface tension-reducing properties of organic species has broadened its applicability to more complex particle types [*Raymond and Pandis*, 2002, 2003; *Bilde and Svenningsson*, 2004; *Hartz et al.*, 2006; *Svenningsson et al.*, 2006, *Petters and Kreidenweis,* 2007, *Moore et al.*, 2011]. Studies suggest overestimation in $N_{CCN}$ when the aerosol is assumed to be in an internal mixture and underestimation when it is assumed to be in an external mixture [*Mircea et al.*, 2002; *Broekhuizen et al.*, 2006; *Rissler et al.*, 2006; *Roberts et al.*, 2006; *Medina et al.*, 2007; *Cubison et al.*, 2008; *Furutani et al.*, 2008; *Kuwata et al.*, 2008; *Quinn et al.*, 2008; *Shantz et al.*, 2008; *Wang et al.*, 2008; *Bougiatioti et al.*, 2009; *Chang et al.*, 2010; *Gunthe et al.*, 2009; *Lance et al.*, 2009; *Kammermann et al.*, 2010; *Roberts et al.*, 2010; *Rose et al.*, 2010; *Wang et al.*, 2010]. While inclusion of mixing state and chemical composition can greatly increase $N_{CCN}$ estimation accuracy [*Mircea et al.*, 2005; *Medina et al.*, 2007; *Stroud et al.*, 2007; *Cubison et al.*, 2008; *Lance et al.*, 2009; *Quinn et al.*, 2008; *Asa-Awuku et al.*, 2011], lack of detailed aerosol characteristics often limits their use.

My overall focus here is to thoroughly analyze the growth and hygroscopicity of aerosols at the Department of Energy's Southern Great Plains (SGP) site in Oklahoma, U.S. More specifically I have used the data to i) develop a simple two-component model

that is able to broadly categorize secondary aerosol precursors into inorganic and organic species, ii) quantify aerosol mixing state using a size dependent threshold standard deviation, iii) estimate optical properties using Mie theory, iv) estimate CCN concentration from modified κ- Köhler theory, and v) parameterize both the optical properties and CCN concentration using routinely measured aerosol properties.

# CHAPTER II

# SITE DESCRIPTION

The submicron size distributions and size-resolved hygroscopic growth distributions have been measured at SGP with a scanning mobility particle sizer (SMPS) and a hygroscopic tandem mobility analyzer (HTDMA), respectively. The instruments were housed in the Aerosol Observing System (AOS) trailer. Although this site is primarily a mixed land use area of cattle pastures and agricultural fields, transported air masses from other regions bring diversity in aerosol concentration and properties. The wind rose diagram from nearby Ponca City (Figure 1) shows that winds at the site are most frequently from the south and southeast and less frequently from the north. *Parworth et al.* [2015] described the seasonal distribution of air mass transport in 2011 - 2012 based on the NOAA HYSPLIT model. During the summer, winds were most often from the south and southeast, while during the winter they were largely from the north. Winds in the spring and fall were more variable. Air arriving from the south/southeast often has elevated sulfur dioxide ($SO_2$) originating from industrial processes and fuel combustion, nitrogen oxides ($NO_x = NO + NO_2$) from industrial processes and vehicle emissions, and secondary organic aerosol (SOA) and high concentrations of bases from local agricultural fields [*Hodshire et al.*, 2016]. Air arriving from the north primarily brings biogenic SOA and precursors and high concentrations of gas phase bases resulting from agricultural activities [*Hodshire et al.*, 2016], with lower concentrations

of $NO_x$ than with southerly winds. The site is far enough downwind of most major anthropogenic sources that the aerosol is diluted during transport [*Parworth et al.*, 2015].

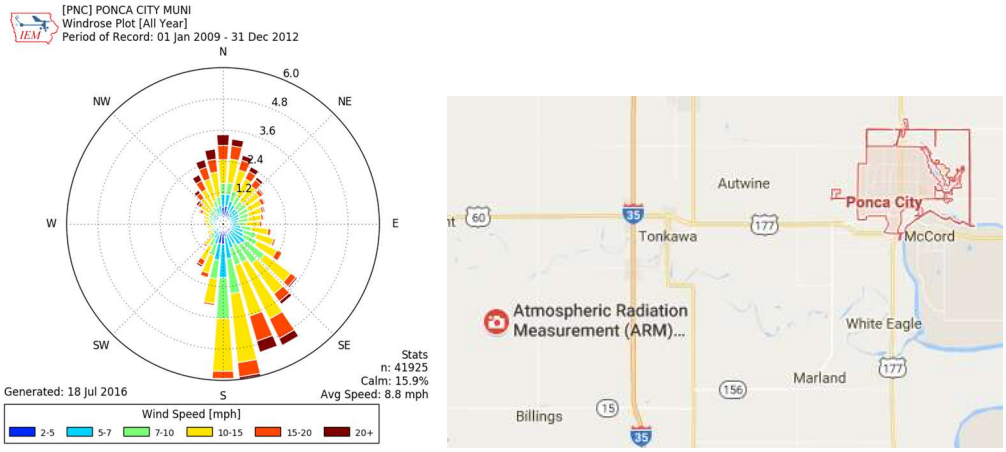


**Figure 1. Wind rose plot for Ponca City (~ 25 mile northeast of ARM SGP site), OK, from 2009-2012 (Source: http://mesonet.agron.iastate.edu) (left). Location of Ponca city and ARM SGP site (right).**

CHAPTER III

# ANALYSIS OF PARTICLE GROWTH AND HYGROSCOPICITY

## Introduction

Atmospheric aerosols affect the global climate directly by altering the radiation budget through scattering and absorbing the radiation and indirectly by acting as cloud condensation nuclei (CCN), that partially determine the cloud optical behavior, lifetime and overall precipitation pattern over a region. Formation of the secondary aerosol by gas to particle conversion and subsequent growth are frequently observed in the atmosphere [*Yli-Juuti et al*., 2011; *Perrington et al.*, 2013]. Particle growth occurs primarily due to condensation of low volatility gases, but can be impacted by other mechanisms too, e.g., coagulation, heterogeneous reaction etc. [*Zhang et al*., 2011]. For condensational growth, sulfuric acid is considered as the key precursor [*Kuang et al.*, 2007] for its higher gas phase concentration, lower saturation vapor pressure, and strong bonding with water and basic gas molecules [*Zhang et al.*, 2012]; though semi-volatile organic compounds can be more significant sometimes [*Smith et al.*, 2008]. The studies conducted over the forested region of Hyytiälä, Finland, suggest biogenic emission of monoterpene as the primary cause of new particle formation (NPF) and growth [*Yli-Juuti et al*., 2011]. The number of NPF events usually maximized in the spring coinciding with the timing of heightened emission of volatile organic carbon (VOC) and were rarely observed in the winter when the VOC concentration drops [*Maso et al*., 2005]. Typically the increased photochemical oxidation and VOC concentration help the aerosols to grow most rapidly in the summer

[*Yli-Juuti et al*., 2011]. As indicated by several studies [e.g., *Manninen et al.*, 2010; *Yli-Juuti et al*., 2011], the average aerosol growth rate, which is influenced by the curvature effect as well as the time of the day, increased with increasing particle size.

The expansion of particles in the presence of moisture depends on its chemical content and is expressed by hygroscopic growth factor (HGF) or simply GF, which is the ratio of particle size at higher RH to its dry size ($\frac{D_{@90\%\,RH}}{D_{dry}}$). The higher GF usually represents more hygroscopic (i.e., inorganic) and lower GF represents less-hygroscopic (i.e., organic) species condensation. This apparent connection between GF and chemical species prompted some researchers [e.g., *Gasparini et al.*, 2006; *Meier et al.*, 2009] to determine the change in chemical properties of the condensing compounds from the variation in GF distribution. This was simplified after coupling the growth and hygroscopicity data into hygroscopicity parameter, or kappa (*k*) [*Petters et al.*, 2007; *Cerully et al.*, 2011; *Liu et al.*, 2011].

The primary focus of this study is to thoroughly analyze the growth and hygroscopicity of aerosols at Department of Energy's (DOE) Atmospheric Radiation Measurement Southern Great Plain (ARM SGP) site, and combine them to propose a two-component condensable gas model which is able to broadly categorize the precursors.

## Methodology

Since 2005 the particle size and size resolved hygroscopicity distributions are continuously being measured at SGP site. The current study is based on the size

distribution of 12 nm - 760 nm and the size resolved hygroscopicity distribution of 13, 25, 50, 100, 200, 400 and 600 nm particles from 2009 and 2011.

*Seasonal variation of the growth events*

In 2009, all growth events beyond 12 nm were taken into account by carefully detecting sudden increase in number concentration of smallest detectable (i.e., 12 nm) particles followed by a persistent modal growth for atleast 3 hours. The frequency of those growth events was determined for each month and plotted.

*Influencing growth channels*

Following the particle formation, one or more growth channels, such as, condensation, coagulation, heterogeneous reaction etc. can be competitive based on existing particle concentration and their size distribution [*Zhang et al.*, 2011]. The overall growth was attributed to coagulation and condensation; and relative importance of each was examined. Discrete coagulation equation was used to calculate the coagulation rate of the k-mers and the resultant coagulated number concentration.

$$\frac{dN_{k(t)}}{dt} = \frac{1}{2}\sum_{j=1}^{k-1} K_{j,k-j} N_j N_{k-j} \; - \; N_k \sum_{j=1}^{\infty} K_{k,j} N_j \,, \quad k \geq 2 \qquad (1)$$

Where, $K_{j,k-j}$ is the coagulation coefficient between $j^{th}$ and $(k\text{-}j)^{th}$ particle, $N_j$ and $N_{k-j}$ corresponding number concentrations. The particle concentration subject to

condensational growth was determined by subtracting the concentration of coagulated particles from the total concentration.

*Growth rate (GR) profile*

The growing particle mode was detected, isolated and fitted using Polynomial method. The isolation of the growing particle mode is particularly important when multiple modes are present (e.g., in polluted condition). The particle growth rate was calculated and plotted as a function of time of the day and particle size. Also its diurnal and seasonal pattern was analyzed.

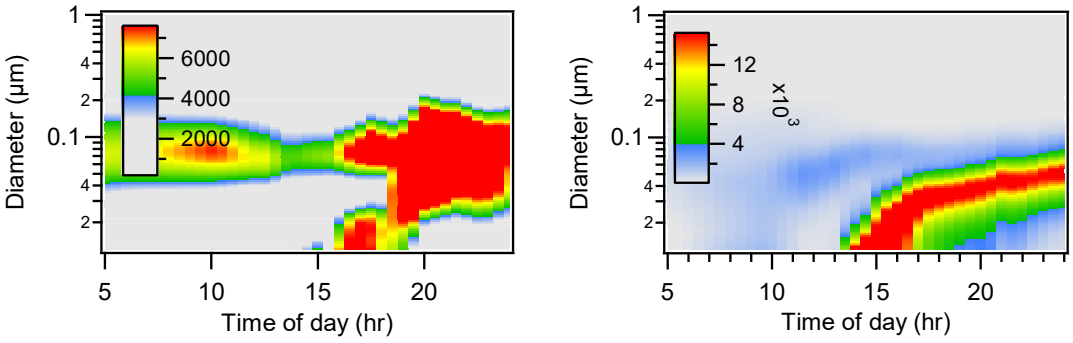


**Figure 2. Lognormal number size distribution on April 16 (left) and October 6, 2009 (right). Two modes can be seen on April 16 due to high pollution, but a single mode on a clean background can be seen on October 6, 2009.**

*Growth factor (GF) profile*

The size resolved hygroscopic growth factor (GF) was measured at 90% RH for 7 fixed particle sizes and was used as reference to calculate GF of the growing mode by interpolation. Similar to GR, the temporal variation in the GF profile was discussed.

*Two-component condensable gas (inorganic vs. organic) model*

The two-component condensable gas model was introduced to broadly categorize the gas phase precursor into inorganic and organic species. The hygroscopicity parameter, Kappa, *k*, was determined from equation 2 as described by *Petters and Kreidenweis* [2007].

$$k = (GF^3 - 1)\left\{\frac{1}{S}\exp\left(\frac{4\frac{\sigma_s}{a}M_w}{RT\rho_w D}\right) - 1\right\} = \sum_i \varepsilon_i k_i \quad (2)$$

Where, S is the saturation ratio, $\rho_w$ density of the water, $M_w$ molecular weight of the water, $\sigma_s/a$ surface tension of the solution/ air interface, R the universal gas constant, T the temperature, D the droplet diameter, *i* corresponding individual species, and $\varepsilon$ dry volume fraction. The concentrations of inorganic ($C_{in}$) and organic ($C_{org}$) precursors were calculated by rearranging the mass balance equations as described in Case 1 to 3.

Case 1: Kinetic regime (Knudsen number ($\frac{mean\ free\ path}{particle\ size}$), Kn > 1)

$$C_{in} = \left(\frac{r}{r+1}\right)\frac{2\rho}{M_{in}\overline{c_A}\alpha}\left(\frac{dD}{dt}\right) \quad (3)$$

$$C_{org} = \left(\frac{1}{r+1}\right)\frac{2\rho}{M_{org}\overline{c_A}\alpha}\left(\frac{dD}{dt}\right) \quad (4)$$

Case 2: Transition regime, Kn ~1

$$C_{in} = \frac{(1+1.333K_n+(1.333\sqrt{\pi}K_n+1)K_n)}{(1+1.333K_n)}\left(\frac{r}{r+1}\right)\frac{\rho D}{4M_{in}D_i}\left(\frac{dD}{dt}\right) \quad (5)$$

$$C_{org} = \frac{(1+1.333K_n+(1.333\sqrt{\pi}K_n+1)K_n)}{(1+1.333K_n)}\left(\frac{1}{r+1}\right)\frac{\rho D}{4M_{org}D_i}\left(\frac{dD}{dt}\right) \quad (6)$$

Case 3: Continuum regime (Knudsen number, Kn < 1)

$$C_{in} = \left(\frac{r}{r+1}\right)\frac{\rho D}{4M_{in}D_i}\left(\frac{dD}{dt}\right) \quad (7)$$

$$C_{org} = \left(\frac{r}{r+1}\right)\frac{\rho D}{4M_{org}D_i}\left(\frac{dD}{dt}\right) \quad (8)$$

Where, $C$ is the precursor concentration, r simplified volume fraction ratio of inorganic to organic ($\frac{k-k_{org}}{k_{in}-k}$), $\rho$ the particle density, $\bar{c_A}$ the mean speed of the molecules, $M$ the molecular weight of the inorganic ($M_{in}$) and organic ($M_{org}$) species, $\alpha$ the molecular accommodation coefficient and $D_i$ the diffusion coefficient.

## Result and discussion

*Seasonal variation of growth events*

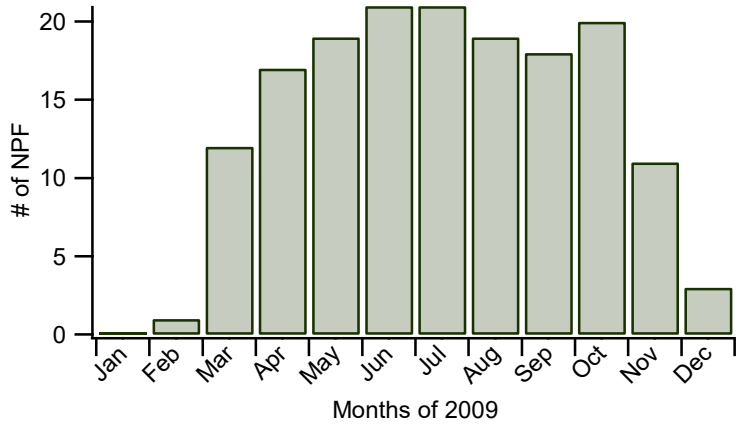


**Figure 3. Seasonal variation in growth event frequency during 2009.**

Evidently, the frequency of growth events increaed abruptly in the spring and dropped in the winter. The first maxima occurred in the summer as a result increased rate of photochemical reactions and abundant VOCs. Besides, many growth events took place following precipitation, which washed out larger particles from the atmosphere, minimized coagulational loss and promoted condensational growth.

*Influencing growth channels*

A significant amount of coagulation loss causes sudden decrease in number concentration and increase in aerosol size, which can affect the size of growing mode

and the growth rate. Effect of coagulation was examined for all the growth events but illustrated here for 3 scenarios.

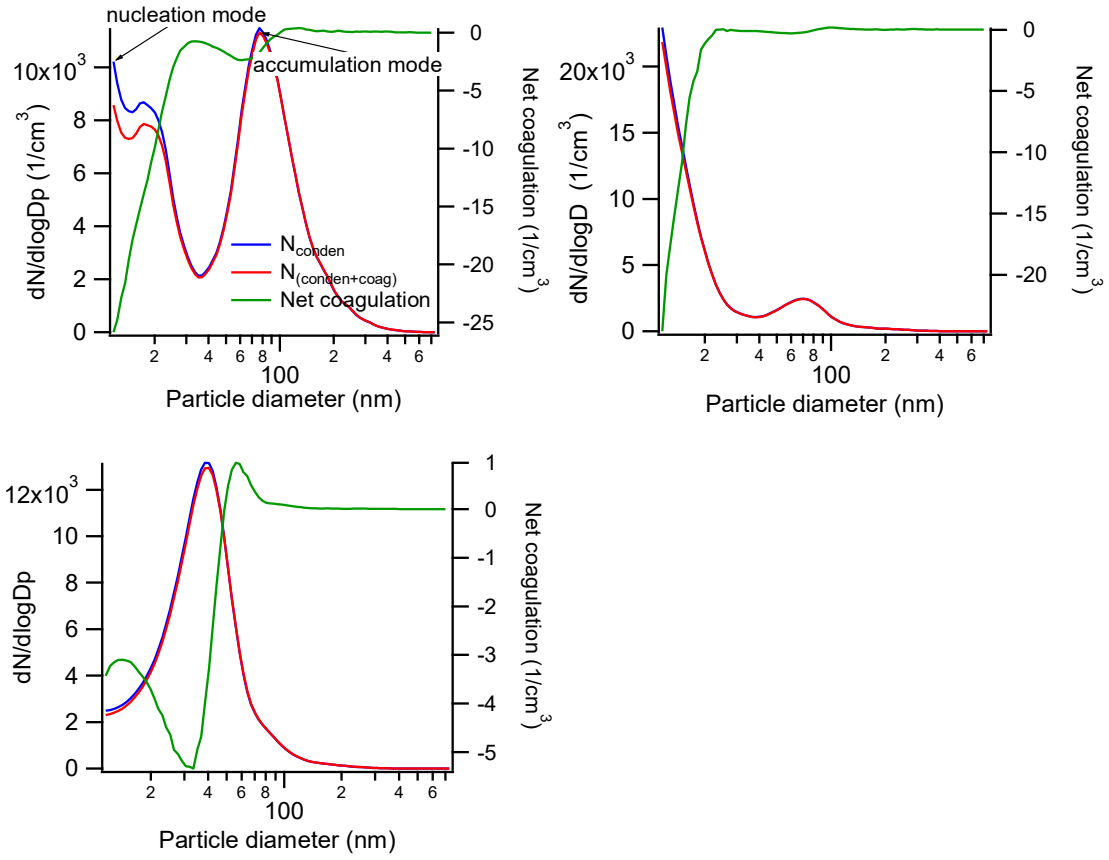


**Figure 4. N concentration and net coagulation on April 16 (top, left); and on October 6 following nucleation (top, right); and several hours after nucleation (bottom) on October 6 in 2009.**

Among the three scenarios, the coagulation loss was maximum (~16% of overall N) for the nucleation range particles on April, 16, 2009, when both the nucleation and accumulation range particle concentrations were high. But that did not alter the profile of growing particle mode.

*Growth profile*

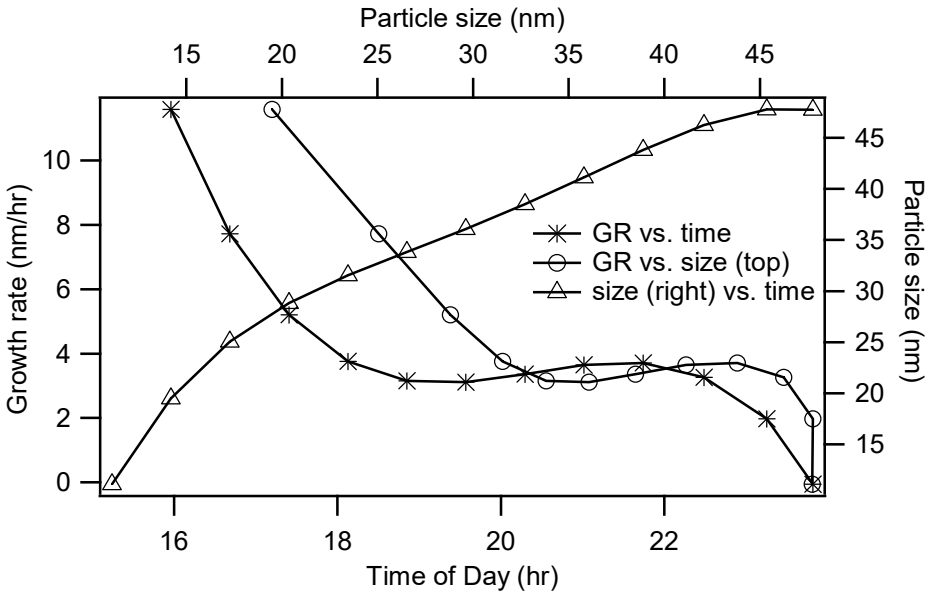


**Figure 5. Variation in aerosol size and growth rate on October 6, 2009.**

The growth rate (GR) was high (11.6 nm/hr) when the particles were first detected (~12 nm) around 3:30 pm, but went down to 3.7 nm/hr as the mode grew upto 30 nm around 6 pm. This outcome is in contradiction with several works which suggested increase in GR with increasing particle size as a result of decreasing curvature effect on larger particles [*Fiedler et al.*, 2005; *Virkkula et al.*, 2007; *Boulon et al.*, 2010; *Manninen et al.*, 2010; *Suni et al.*, 2008; *Yli-Juuti et al.*, 2009; *Vakkari et al.*, 2011; *Yli-Juuti et al.*, 2011]. The size range considered in most of those studies was 1.5 -20 nm. The small particles within that range grew during the earlier hours of the day when the photochemical reaction rates and the biogenic emissions were not significant, but the larger particles grew during later hours when the atmospheric conditions were more

favorable. In our case, the growing mode often reached the smallest detectable range (~12 nm) around noon when the photochemical reaction rates and the biogenic emissions were at their peak, and grew further at late hours when they decline.

*Seasonal variation of growth rate*

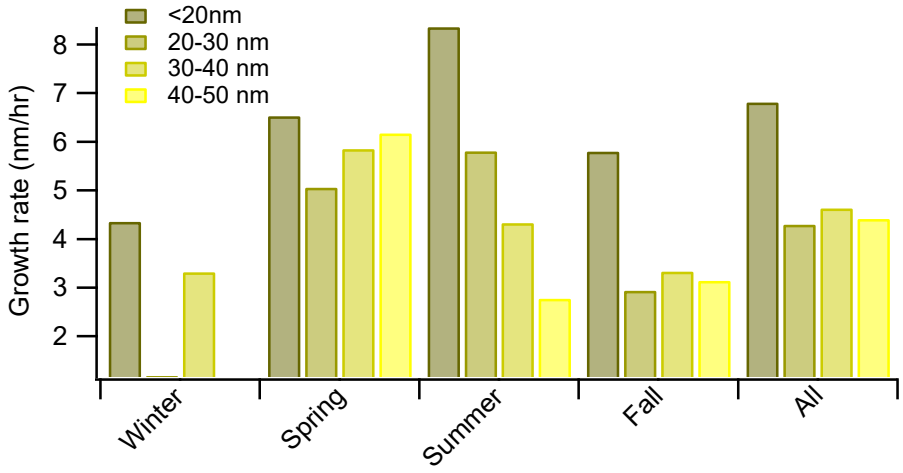


**Figure 6. Seasonal variation in growth rates for 4 size classes during 2009.**

The trend in growth rate is more apparent below and above 20 nm size. Therefore, all growth events were re-categorized into 2 size groups: smaller and larger than 22 nm (The adjustment was made to capture more observations in <22 nm group) and presented in Figure 7.

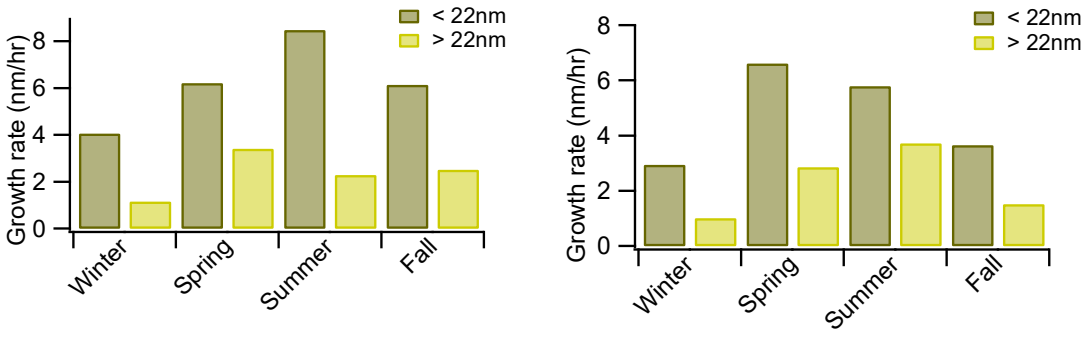


**Figure 7. Seasonal variation in particle growth rates in 2009 (left) and 2011 (right).**

For both years and size groups the GR was lowest in the winter, increased noticeably in the spring and continued through the summer before dropping slightly in the fall. As the variation in GR largely depends on the seasonal profile of the temperature, photochemical reaction and precursor concentration, GR in the summer and spring was naturally higher than other seasons.

*Growth factor (GF) profile*

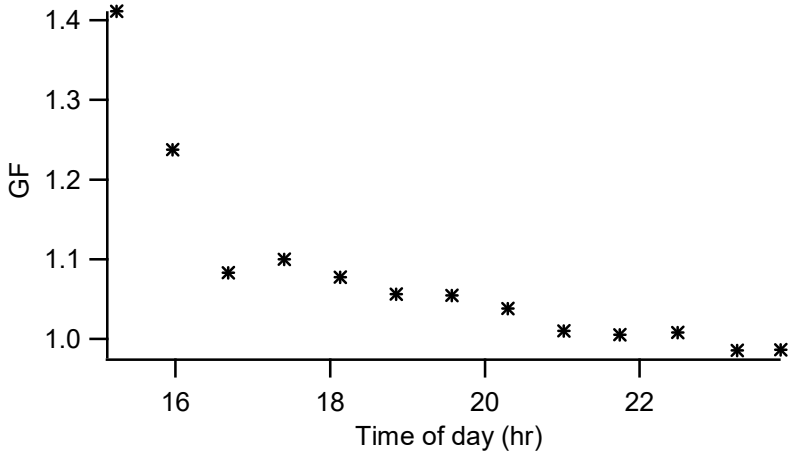


**Figure 8. Diurnal variation in GF on October 6, 2009.**

Despite large variation in diurnal patterns, GF was usually higher during the daytime (suggesting inorganic species condensation) and lower at night (suggesting organic species condensation or oligomerization). As the GF distribution did not display any seasonal pattern in 2009 or 2011, the plots are not included.

*Precursor concentration profile*

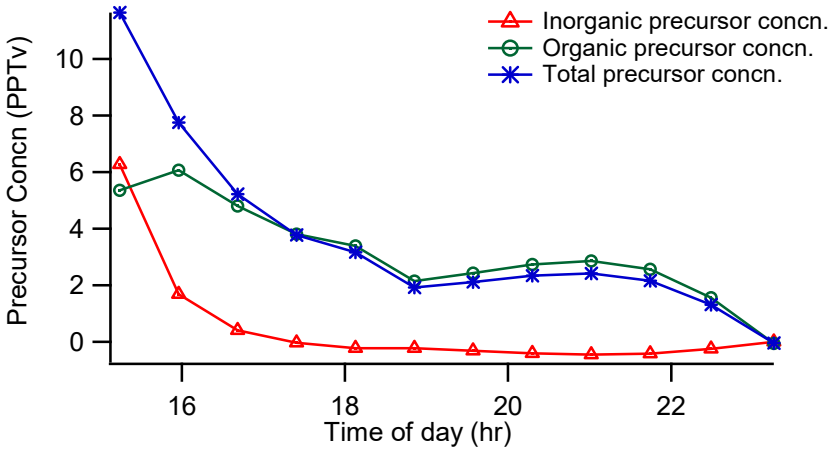


**Figure 9. Diurnal variation in precursor concentration on October 6, 2009.**

According to the proposed two-component condensable gas model, the inorganic precursor concentration went down to zero after 5 pm. This is not surprising as the gas phase concentration of the most common inorganic precursor, $H_2SO_4$, reaches its peak around noon [*Zheng et al.*, 2011]. The organic precursor concentration was usually higher during the day due to higher leaf temperature and the light intensity, but its partitioning into particle phase is more effective at night. The gas phase precursor concentration was considered to be proportional to particle phase concentration in this

model. On October 6, 2009, the night time growth primarily occurred due to condensation of organic species, but the day time condensational growth was caused by both, inorganic and organic species.

*Seasonal variation in precursor concentrations*

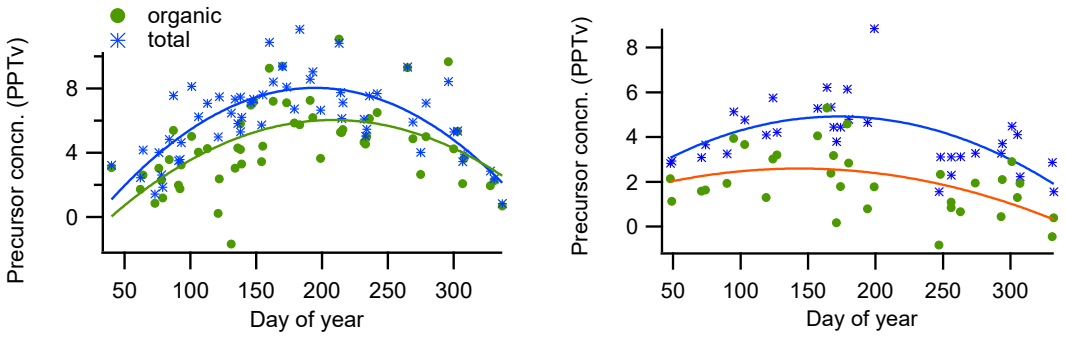


**Figure 10. Seasonal variation in precursor concentration in 2009 (left) and 2011 (right).**

The organic (and total) precursor concentration profile displays seasonal characteristics with maxima in the summer, when the controlling factors, such as, the radiation intensity, temperature, and VOC emission rates are all at their peak.

## Summary

The particle size distribution and size resolved growth factor distribution measured at SGP site in 2009 and 2011 with a SMPS/HTDMA system were used to analyze the growth and hygroscopicity pattern in atmospheric particles and combine those data to determine the organic and inorganic precursor concentration using a simple

two-component condensable gas model. In 2009, frequent NPF growth events, the pattern of which is assumed to be mainly driven by the rate of photochemical reactions and biogenic emissions, were detected at the beginning of the spring which dropped at the arrival of the winter. Condensational growth was found to be the major growth mechanism at all scenarios. The growth of particles from (~) 13 nm to 22 nm took place during the time of the day when both photochemical reaction and biogenic emission rate were higher relative to when growth of relatively larger particles took place. This explains the derived higher growth rate in smaller particles. For the entire size range the average growth rate was greater in warmer months. The hygroscopic growth of the growing mode particles was usually higher during the day indicating more inorganic species condensation then than night. This supposition was supported by the derived inorganic and organic precursor concentration from the two-component condensable gas model. The seasonal variation in organic precursor concentration showed greater value in summer as a result of intense radiation and biogenic emission.

# CHAPTER IV

# ANALYSIS OF A MULTI-YEAR RECORD OF SIZE-RESOLVED HYGROSCOPICITY MEASUREMENTS*[1]

## Introduction

Atmospheric particles influence climate by scattering and absorbing solar radiation and by acting as cloud condensation nuclei (CCN). The extent of this influence depends on the size of the particles, which can be significantly increased when hygroscopic aerosols are exposed to high relative humidity (RH). Among common atmospheric particle types, those composed of soluble inorganic species are generally the most hygroscopic, while those composed of organics exhibit a range in hygroscopicity with some being slightly hygroscopic [*Saxena and Hildemann*, 1996; *Zappoli et al.*, 1999; *Peng et al.*, 2001; *Svenningsson et al.*, 2006; *King et al.*, 2007; *Prenni et al.*, 2007; *Duplissy et al.*,2008; *Smith et al.*, 2008; *Engelhart et al.*, 2008; *Gunthe et al.*, 2009; *Jurányi et al.*, 2009; *King et al.*, 2009; *King et al.*, 2010.; *Yli-Juuti et al.*, 2011] and others non-hygroscopic [*Abbatt et al.*, 2005; *Prenni et al.*, 2007]. Major inorganic species such as ammonium, sulfate, nitrate, and chloride are typically the primary contributors to water uptake and consequent hygroscopic growth of atmospheric aerosols. The varied and complex composition of organic aerosols results in varied

[1] *Reprinted with permission from "Analysis of a Multi-Year Record of Size-Resolved Hygroscopicity Measurements from a Rural Site in the U.S." by Mahish, M. and Collins, D., 2017, Aerosol and Air Quality Research, Vol 17, Page 1389-1400, Copyright [2017] by Taiwan Association for Aerosol Research (TAAR)

hygroscopicity that remains an active area of study. Organics can also influence water uptake by inorganic species in the same particle, with studies showing reduced water uptake by inorganic salts above their deliquescence RH (DRH), but higher uptake below it relative to particles composed of the pure species [*Dick et al.*, 2000; *Hersey et al.*, 2009; *Meyer et al.*, 2009]. Other studies have shown the influence of organics differs among inorganics, with addition of commonly found organics resulting in decreased water uptake by NaCl but increased water uptake by $(NH_4)_2SO_4$ [*Cruz et al.*, 2000; *Choi et al.*, 2002]. The effect of organics on the hygroscopicity of multi-component aerosols varies by type and amount, but often can be explained by the simple ZSR mixing rule at RH above the DRH [*Jing et al.*, 2016; *Peng et al.*, 2016]. This link with composition supports the use of GF as a rough proxy for particle type [*McMurry and Stolzenburg*, 1989; *Zhang et al.*, 1993; *Gysel et al.*, 2007], with higher GF indicating a higher soluble inorganic content and lower GF indicating a higher content of organics and/or insoluble components such as soot and dust.

Hygroscopic growth of an aerosol is often measured using a Hygroscopic Tandem Differential Mobility Analyzer (HTDMA), which was first illustrated by *Liu et al.* [1978]. The measured distribution of particle hygroscopicity is usually reported in terms of the Hygroscopic Growth Factor or simply Growth Factor (GF), which is the ratio of the size of a particle at high relative humidity to its dry size ($\frac{D_{@\text{high RH}}}{D_{@\text{low RH}}}$). *Gasparini et al.* [2006] reported increased hygroscopicity with increasing particle size based on HTDMA data collected in May 2003 at the Department of Energy's Southern Great Plains (SGP) Atmospheric Radiation Measurement (ARM) site in an agricultural

area of Oklahoma, U.S., which is also the location of the study reported here. This result is supported by the findings of *Holmgren et al.* [2014], *Levin et al.* [2014], and others. An interpretation of this size dependent hygroscopicity is a higher organic content in smaller particles. *Levin et al.* [2014] reported results from a forest site that are consistent with this interpretation, with higher organic fraction in smaller particles and increasing inorganic fraction in larger particles.

Aerosol hygroscopicity in continental locations often exhibits a diel pattern, frequently being higher during the day and lower at night, as observed in a boreal forest in Hyytiälä, southern Finland [*Ehn et al.*, 2007], and at a polluted site of the North China Plain [*Liu et al.*, 2011]. The pattern at Hyytiälä has been attributed to higher gas phase concentration of sulfuric acid during the day [*Fiedler et al.*, 2005], and abundant less hygroscopic organic compounds at night [*Sellegri et al.*, 2005]. The diel pattern observed at the North China Plain has been attributed to accumulation of freshly emitted non-hygroscopic particles near the surface at night and of aged particles during the day. *Holmgren et al.* [2014], however, found more hygroscopic aerosols at night than during the day at the high altitude site, Puy de Dôme, France, where boundary layer dynamics and long range transport play more important roles.

*Holmgren et al.* [2014] used hygroscopicity data to derive growth factor probability density functions (GF-PDFs) and used them to quantify aerosol mixing state. They described aerosols for which GF-PDFs had standard deviations (SD) less than 0.1 as internal mixtures and those with SD higher than 0.15 as external mixtures. For external mixtures, at least two modes were identified. The median GF and number

concentration of each mode were determined and the mode was then categorized into one of three groups: more-hygroscopic, hygroscopic, or less-hygroscopic. Their study explored the influences of particle size and seasons on mixing state. They found that accumulation mode particles were more frequently in external mixtures during autumn and winter.

Our study uses size and GF distributions to analyze the overall hygroscopic properties of the aerosol population, the variation of those properties with time of day and with particle size, and the connection of those properties and their time dependence with new particle formation (NPF) events. Additionally, the mixing state of the aerosol has been quantified using a particle size dependent threshold SD (i.e., SD(D)) over the full measurement size range.

## Methodology

Growth factor distributions were first used to calculate hygroscopicity parameters (*kappa* or $\kappa$) for 13, 25, 50, 100, 200, and 400 nm dry diameter particles using $\kappa$-Köhler theory [*Petters and Kreidenweis*, 2007]. Averages of $\kappa$ were calculated for three different time spans of the day: morning (midnight - 10:30 am), day (10:30 am – 7:00 pm), and night (7:00 pm – midnight). Further, separate morning, day, and night averages of $\kappa$ were recorded for days with and for days without NPF events for which the particle mode grew past 13 nm and was discernable for at least 3 hours (referred to simply as NPF event days later). The analysis here largely focuses on the dominant GF mode/modes at the six particle sizes for which GF distributions are routinely measured.

Each mode was categorized into one of three hygroscopicity groups: hygroscopic ($GF > 1.3$), less-hygroscopic ($1.3 \geq GF > 1.15$), and nearly-hydrophobic ($GF \leq 1.15$).

Different particle types within an external mixture generally have different hygroscopicity, resulting in GF distributions with a single broad mode or multiple narrow modes, and correspondingly high SD. In contrast, all particles in internal aerosol mixtures have the same composition and, therefore, the same hygroscopicity, leading to unimodal and narrow GF distributions with low SD. Here, the SD of the GF distributions is used to quantify the aerosol (hygroscopicity) mixing state, similar to the approach of *Holmgren et al.* [2014]. Specifically, we use the ratio of the GF distribution SD calculated for each measurement, $SD_{measurement}$, to a reference value, $SD_{int/ext}$, that is selected to roughly represent the separation between a more internal and a more external mixture at that size. That reference value is based on the lowest *SD* values observed over the 4-year period, which are assumed to represent the values for an internal mixture. Figure 11 presents the calculated *SD* for every GF distribution measured from 2009 to 2012.

The rightward extension and the increased breadth of the histograms in Figure 11 for the smaller and the larger particles is due partially to the increased frequency of broad and/or multi-modal GF distributions and to greater compositional variability over time, respectively. But size-dependent characteristics of the HTDMA response also contribute. The breadth of the GF distributions for the smaller particles (e.g., 13 nm) is increased due to diffusional broadening [*Stolzenburg*, 1988]. For measurements of the larger particles (e.g., 400 nm) the instrument flow rates are automatically reduced, which

broadens the instrument response due to an increased impact of mixing (or smearing) in the tubing connecting the condensation particle counter (CPC) to the downstream DMA outlet [*Russell et al.*, 1995; *Collins et al.*, 2002]. The GF distributions for the small and large particle size tails of the size range also tend to be noisier due to low particle counts, and are therefore more sensitive to false counts. Thus, because the *SD* of a true internally mixed aerosol would vary with particle size, the reference value used for the mixing state quantification is also assumed to be size-dependent. Somewhat arbitrarily, the reference *SD* for each dry size is defined based on that corresponding to the 10% cumulative frequency, $SD_{10\%}$, for all observations, which is shown in Figure 12 as the intersection of each of the cumulative frequency curves with the dashed horizontal line. Based on visual inspection of the results for different GF distributions, $SD_{int/ext}$ was defined as 1.4 x $SD_{10\%}$, with the results for all sizes also shown in Figure 12. For each measurement, a hygroscopicity-based mixing state value was calculated as $MS_{hy} = \frac{SD_{measurement}}{SD_{int/ext}}$. A GF distribution with an $MS_{hyg}$ higher (lower) than 1 indicates a more external (internal) mixture for that particle size.

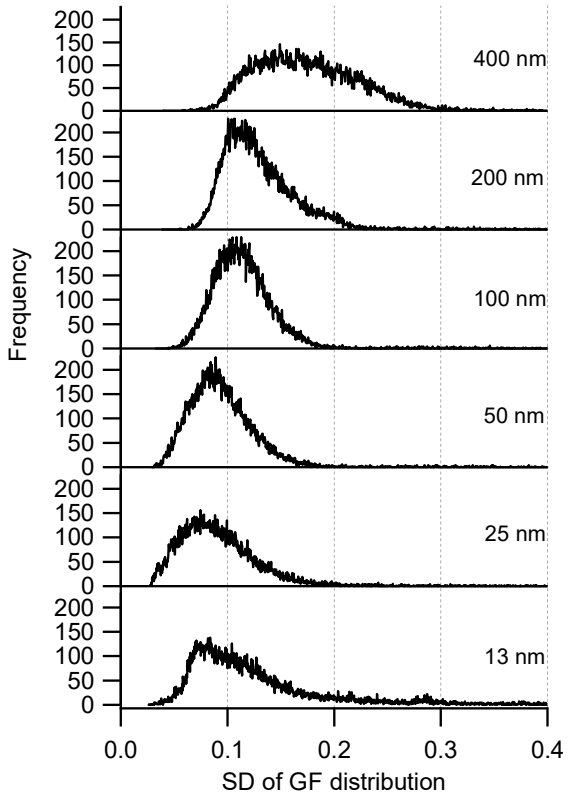


**Figure 11. SD histograms for all GF data from 2009 to 2012.**

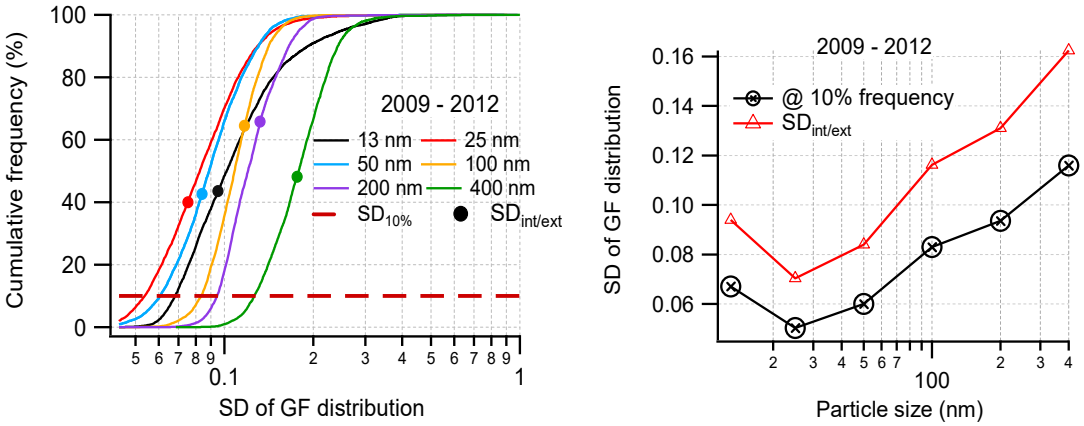


**Figure 12. Cumulative frequency vs. SD (left) and SD at 10% cumulative frequency and $SD_{int/ext}$ (right).**

## Result and discussion

*Diel variation in kappa (κ)*

The hygroscopicity parameter, $\kappa$, was determined for each mode in all GF distributions measured over the 4-year period. Among the commonly observed aerosol hygroscopicity characteristics at the site is the diel pattern evident in the example 4-day time series shown in Figure 13.

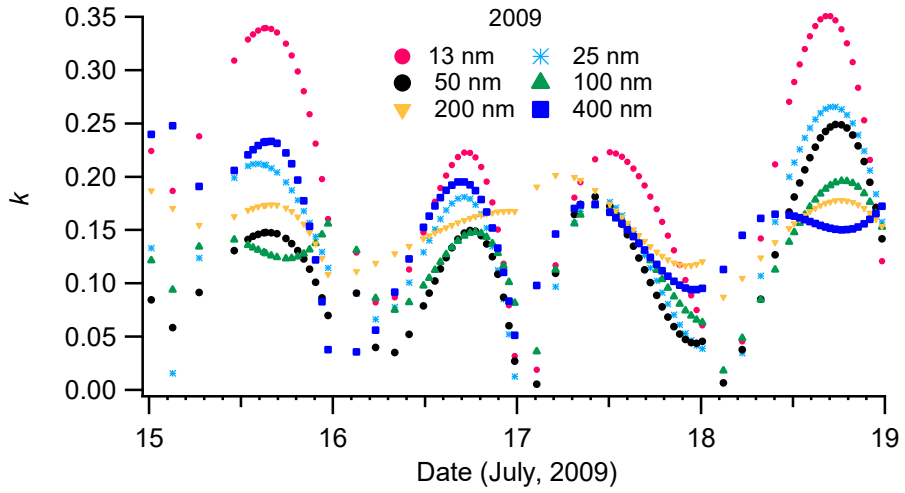


**Figure 13. Diel variation in $\kappa$ from 15$^{th}$ to 18$^{th}$ July, 2009.**

For all particle sizes, $\kappa$ is generally higher during the day than at night. The daytime enhancement in hygroscopicity likely accompanies production of soluble secondary inorganic and organic species through reactions with hydroxyl radical, OH·, and ozone, $O_3$, both of which are most concentrated during the day. Increased nightly emission of some less hygroscopic organics [*Sellegri et al.*, 2005] can lower the nighttime hygroscopicity as well.

Annual averages of morning, day, and nighttime $\kappa$ as a function of particle size are presented in Figure 14, which displays a diel pattern similar to that shown in Figure 13. Because the relative change in mass due to condensation is typically greatest for small particles, the diel variations are also more pronounced with them.

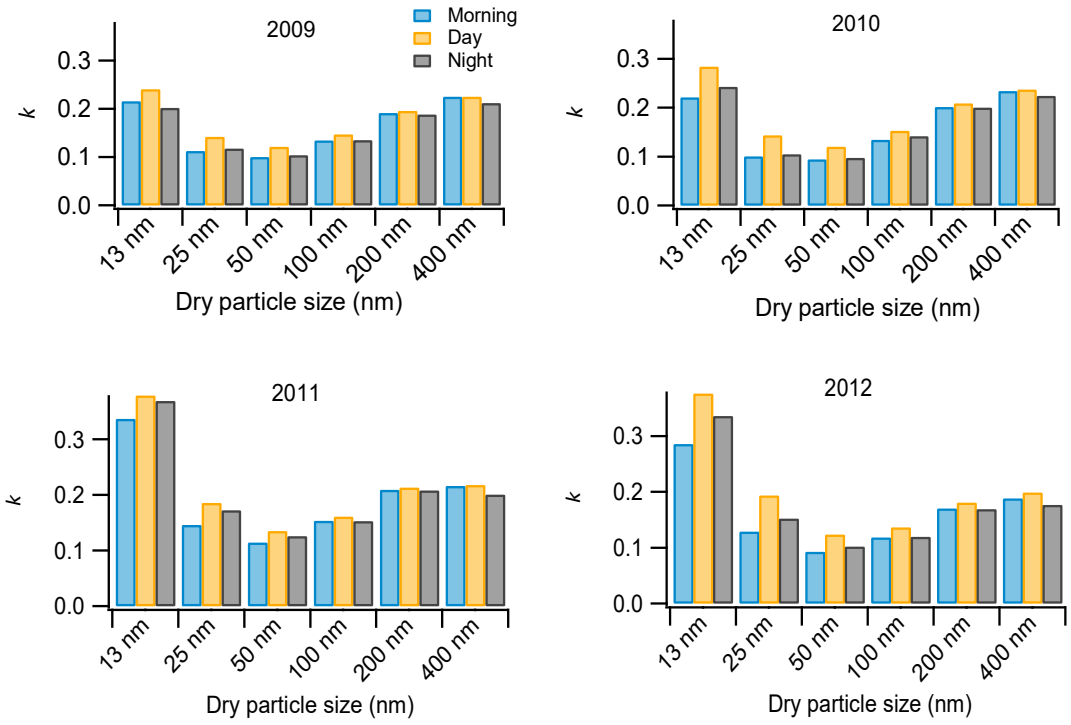


**Figure 14. Annually averaged $\kappa$ for morning, day, and night from 2009 (top, left), 2010 (top, right), 2011 (bottom, left), and 2012 (bottom, right).**

*Size dependence of $\kappa$*

From Figure 14 it is evident that $\kappa$ has a strong size dependence. Very small particles are usually more hygroscopic, perhaps due to a higher content of more hygroscopic species such as sulfate and organic salts that have sufficiently low volatility to condense on them despite the large particle curvature. Hygroscopicity then tends to

gradually decrease with increasing size as less-hygroscopic organic species make up an increasing fraction of the particle mass. This trend reverses for particles larger than 50 nm, which are often cloud activated and have grown through aqueous phase formation of sulfate and oxygenated organics. Within the measured size range, 50 nm particles have the lowest average $\kappa$. The small particle tail of the coarse dust mode often impacts the 600 nm GF distributions, which results in a time dependent variation that is not closely connected with that of the smaller particles. Thus, only the results for the 13 to 400 nm sizes are presented here.

*NPF event vs. non-event day $\kappa$*

During NPF event days particles grow well beyond the 13 nm lower limit of the measured size range. The difference in hygroscopicity between days with and days without NPF events is presented in Figure 15 as the ratio of respective $\kappa$ of the 6 particle sizes. The $\kappa$ on NPF event days was usually higher than on non-event days for smaller particles, especially during the daytime. This in part reflects production of more hygroscopic condensable species on days on which there is active photochemistry. This enhancement on NPF event days is not evident for the 200 and 400 nm particles. This is not unexpected as the NPF mode does not grow into that size range in a day and so any connection between $\kappa$ of those large particles and the events comes from the common influence of the meteorological and chemical conditions that favor NPF. The average morning time $\kappa$ of smaller particles (13 - 50 nm) on NPF event days is lower than that on non-event days. According to *Ehn et al.* [2007], NPF event days at Hyytiälä are similarly

often preceded by a significant concentration of less hygroscopic aerosols, which lowers the morning-time average $\kappa$. The relative changes in $\kappa$ at different times of day and types of day (i.e., NPF event, non-event) are summarized in Figure 16.

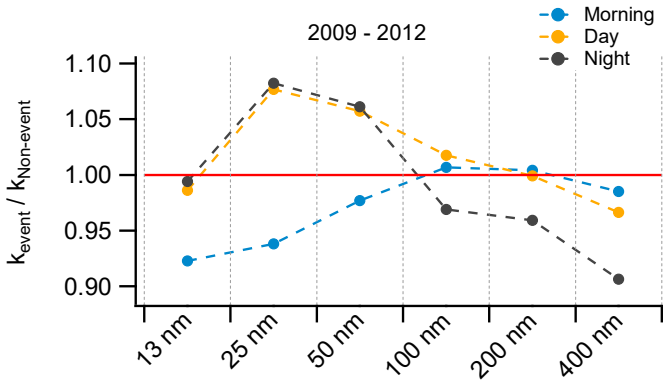


**Figure 15. Average NPF event day $\kappa$ to non-event day $\kappa$ ratio for all measurements from 2009 - 2012. Markers above (below) the red line indicate higher (lower) $\kappa$ on NPF event days than on non-event days.**

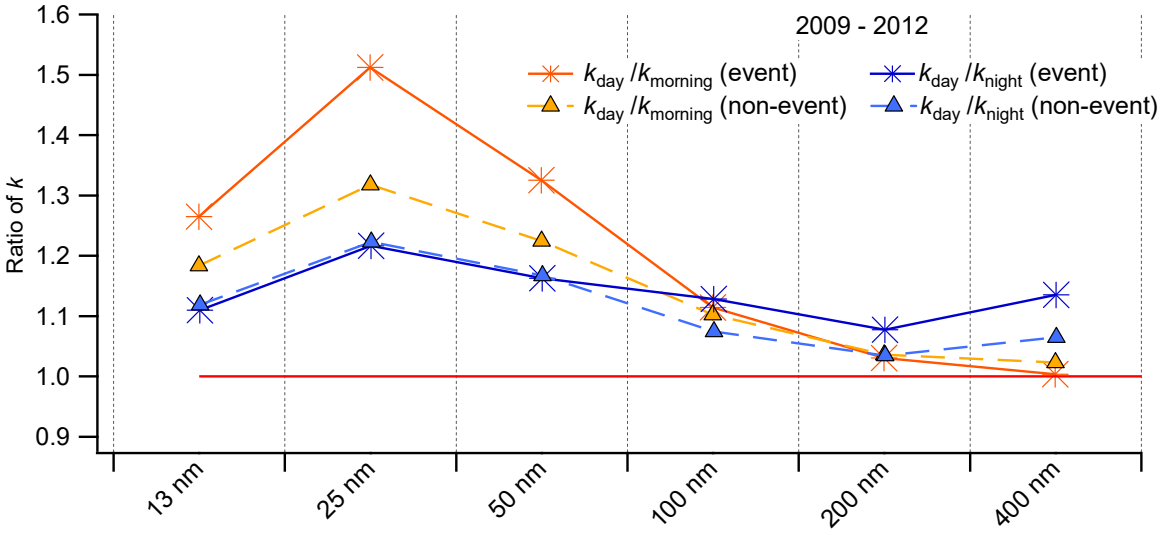


**Figure 16. Change in $\kappa$ from morning to day (orange) and day to night (blue) averaged on NPF event days (star), and non-event days (triangle) from 2009 - 2012.**

The result that all points lie above the red line in Figure 16 indicates that the hygroscopicity is highest during daytime for all sizes. Usually the increase in $\kappa$ from morning to daytime is higher than the decrease in $\kappa$ from daytime to nighttime for particles smaller than 100 nm. This change is greatest for 25 nm particles during event days. The reverse trend is evident in particles larger than 100 nm. For example, the average event daytime $\kappa$ of 25 nm particles was 1.5 times higher than that in the morning and 1.2 times higher than that at night, whereas for 400 nm particles the average $\kappa$ during the daytime was similar to morning but 1.13 times higher than that at night. This indicates that the hygroscopicity of smaller particles is higher at night than in the morning, while for larger particles it is slightly higher in the morning than at night.

## *Quantifying mixing state*

### Mode resolved hygroscopicity

As described in Methodology, modes of GF distributions were classified into three groups. The relative occurrence frequencies at each size and for each year are shown in Figure 17.

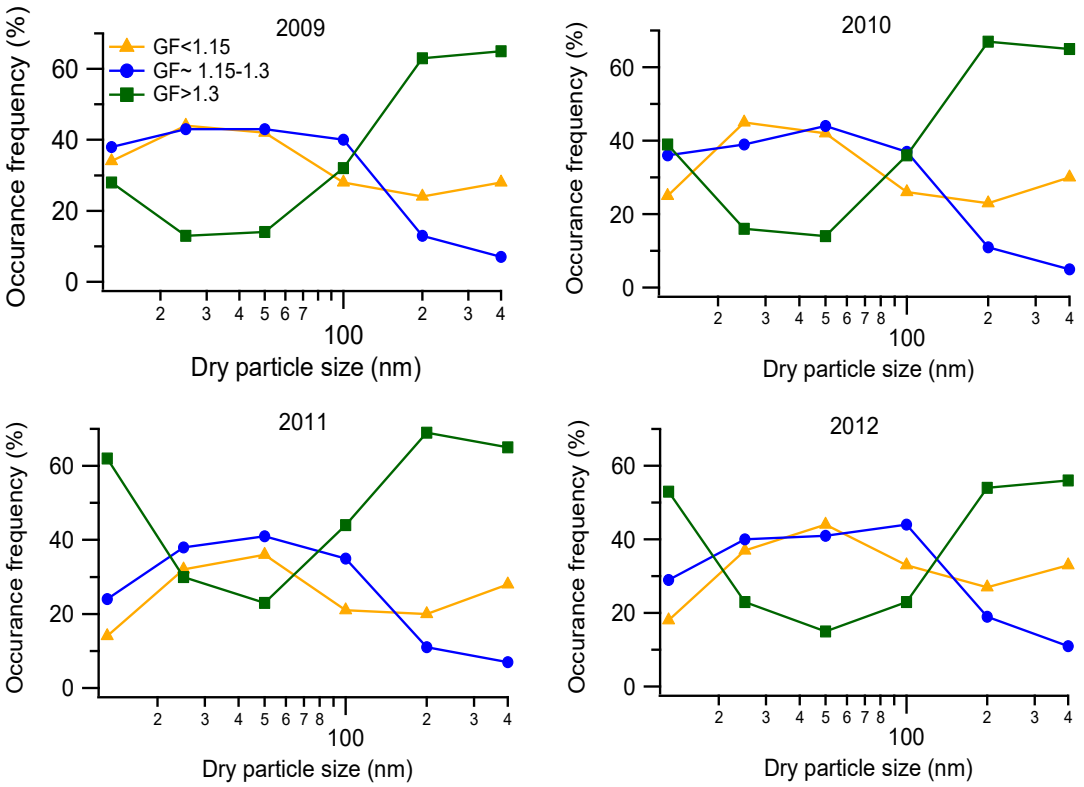


**Figure 17. Average GF for 3 hygroscopicity modes in 2009 (top, left), 2010 (top, right), 2011 (bottom, left), and 2012 (bottom, right).**

A majority of the modes in the hygroscopic growth distributions for particles within the 25 - 100 nm size range were classified as either less-hygroscopic or nearly-hydrophobic. But at larger sizes (>100 nm) there are higher concentrations of hygroscopic and nearly-hydrophobic particles. At least averaged over each year, nearly-hydrophobic particles, which includes fresh carbonaceous aerosols and dust (at larger sizes), are present across the entire size range. A large fraction of the <100 nm particles in the less-hygroscopic category are likely composed of water soluble secondary organic compounds. Increasing sulfate content in larger particles accompanying cloud processing contributes to the increased frequency of hygroscopic modes. Similar

variations with particle size were observed by *Gasparini et al.* [2006], *Levin et al.* [2014], *Swietlicki et al.*, [2008] and others.

**Diel variation in aerosol mixing state**

The SD ratio at each particle size was used to quantify aerosol mixing state as described in Methodology. An example time series for 14$^{th}$ -18$^{th}$ June, 2009 is shown in Figure 18. As is true for this 5-day period, a diel pattern is typically observed.

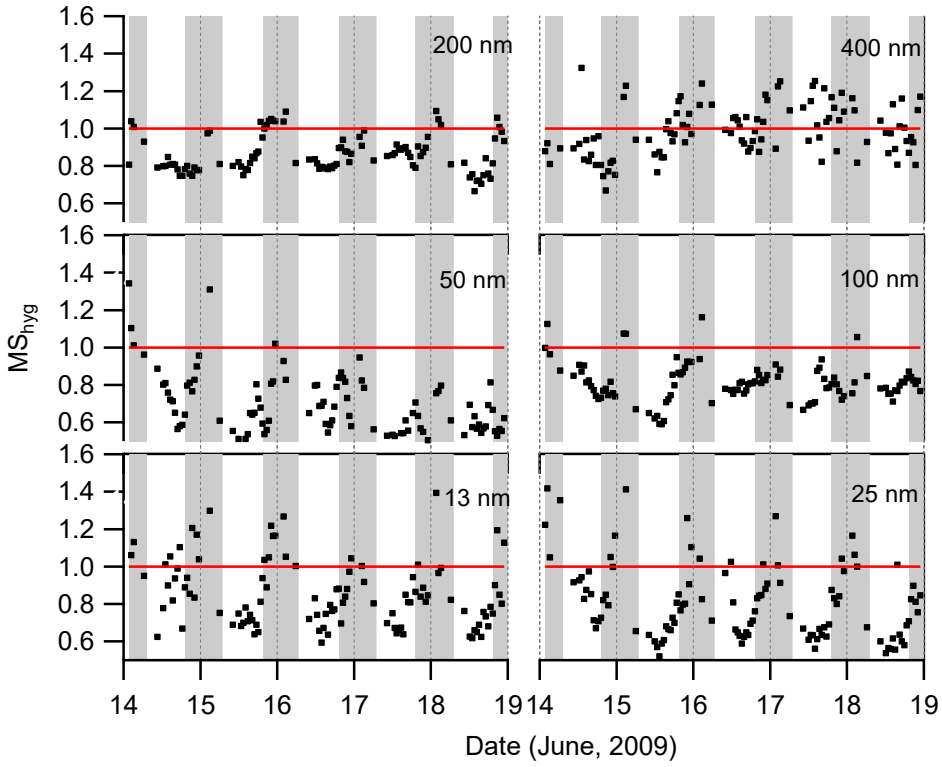


**Figure 18. Diel pattern in hygroscopicity based mixing state from 14$^{th}$ to 18$^{th}$ June, 2009. The light gray shading bands represent nighttime.**

The greater frequency of $MS_{hyg}$ below the '$MS_{hyg}$=1' line during the daytime in Figure 18 indicates more frequent occurrence of internal mixtures, which is likely the result of condensational growth.

**Seasonal variation in aerosol mixing state**

The daily average $MS_{hyg}$ is plotted in Figure 19 for all measurements made between 2009 and 2012 to illustrate the seasonal variation. The relatively lower $MS_{hyg}$ during summer months across all sizes is suggestive of more internally mixed particles at that time of the year. In summer, higher temperature and abundant sunlight expedite photochemical aging to form internal mixtures. In contrast, in the winter enhanced emission of fresh carbonaceous aerosol, lower temperatures, and shorter daylight period make this process less effective, resulting in an increased frequency of external mixtures.

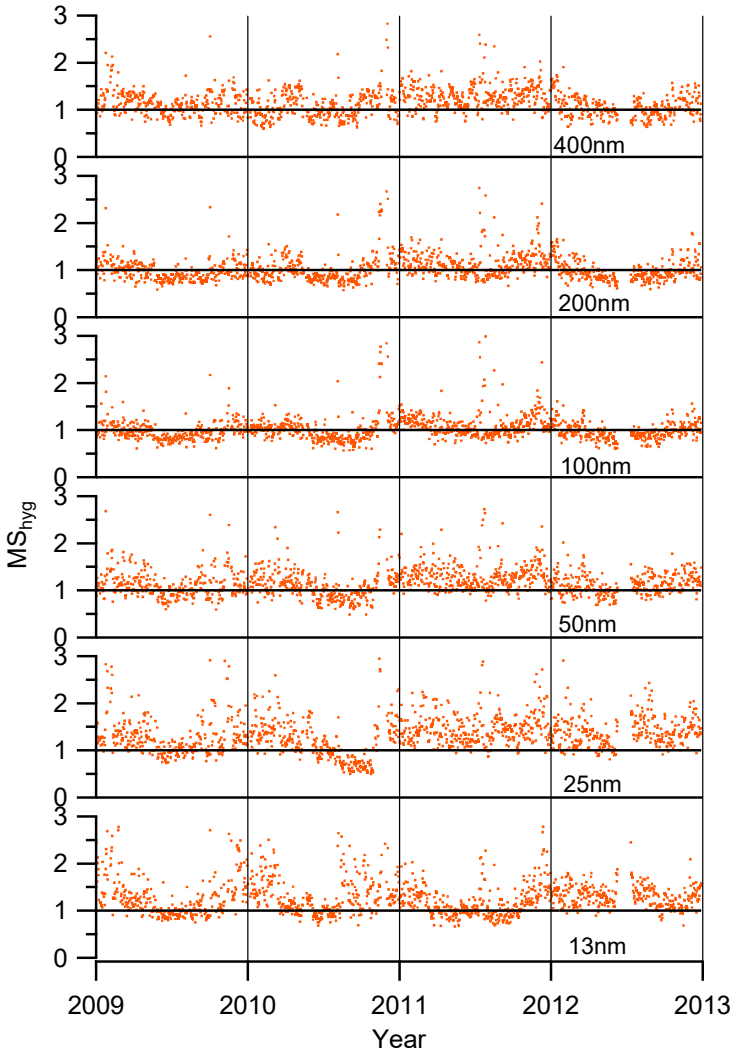


**Figure 19. Annual pattern in daily average $MS_{hyg}$.**

## Summary

Hygroscopic growth factor distributions measured between 2009 and 2012 at the DOE Southern Great Plains (SGP) site were used to calculate size- and time-dependent hygroscopicity parameters (κ), which were then averaged over different time periods. The average κ was highest during the day regardless of particle size, likely due to increased photochemical production of soluble secondary inorganic and organic species.

This trend was more apparent in smaller particles as their relative change in mass from condensation is greater. For each of the 4 years, 50 nm particles were least hygroscopic on average, with hygroscopicity monotonically increasing with increasing size for larger particles and with decreasing size for smaller particles. Averaged daytime κ on days with NPF events ($\kappa_{event}$) were higher than those on days without events ($\kappa_{non\text{-}event}$) for particles smaller than 200 nm that are more directly influenced by the growing mode of nucleated particles. As has been observed elsewhere, smaller particles were typically less hygroscopic in the morning preceding an NPF event.

Modes present in the GF distributions were categorized into three hygroscopicity groups (hygroscopic, less-hygroscopic, and nearly-hydrophobic). At all sizes, modes categorized as nearly-hydrophobic were frequently observed, reflecting the presence of primary carbonaceous particles and/or dust. Consistent with the size-dependent variation in average κ, modes classified as hygroscopic were more frequently observed at the small and large particle tails of the size range. A diel pattern was observed in the hygroscopicity based mixing state, $MS_{hyg}$, which is defined as the ratio of the calculated SD for a measured GF distribution and the size specific threshold SD roughly separating internal and external mixing states. The low values observed during the daytime indicate frequent internal mixing that likely results from uniform condensational growth and photochemical aging. A similar increase in the prevalence of internal mixtures accompanying more active photochemistry and aging is observed during each of the four summers over the measurement period.

# CHAPTER V

# USE OF IN SITU AEROSOL MEASUREMENTS TO ESTIMATE BOUNDARY LAYER UPSCATTER FRACTION.

## Introduction

The radiative balance of the earth is influenced by the greenhouse gases (GHGs) as much as the atmospheric particles. Unlike the warming effect of the GHGs, atmospheric particles can have warming or cooling effect on the atmosphere based on their properties. Therefore, a detailed insight of their role on the radiative balance is crucial and is primary point of this study. *Charlson et al.* [1991] first coined the term, upscatter fraction, (β), ($\frac{b_{ups}}{b_{scat}} = \frac{scattered\ radiation\ to\ upward\ hemisphere}{total\ scattered\ radiation}$) to describe the effect of aerosols on the radiation budget. His formula was modified by *Haywod and Shine* [1995] to include sky conditions as in Equation 9.

$$\Delta\bar{F} = -\frac{1}{2}F_0T_a^2(1-A_c)\omega\bar{\beta}\bar{\tau}[(1-R_s)^2 - \frac{2R_s}{\bar{\beta}}(\frac{1}{\omega}-1)] \quad (9)$$

Where, $\Delta\bar{F}$ is average change in outgoing radiative flux, $F_0$ incident solar flux, $T_a$ fractional transmittence of the atmosphere, $A_c$ fraction of the surface covered by clouds, $R_s$ albedo of the underlying earth surface, $\bar{\beta}$ average upscatter fraction of the aerosol layer, $\bar{\tau}$ average optical depth, and $\omega$ single scattering albedo.

Although $\beta$ is an important parameter, no instrument directly measures it, and there has been limited study in this area. *Wiscombe and Grams* [1976] first introduced $\beta$ as a function of solar zenith angle ($\theta_0$) and aerosol size. As per *Nemesure et al.* [1995], $\beta$ reaches maxima of 0.5 regardless of aerosol size when $\theta_0$ is 90° (i.e., sun at horizon) due to symmetrically distributed radiation at both hemispheres, and minimum when $\theta_0$ is 0° (i.e., overhead sun). The solar position on its annual path affects $\beta$ too (except over places near equator) with a maxima in winter and minima during summer. The aerosol size influences it through the increased forward scattering from larger aerosols.

Our current focus is to estimate boundary layer $\beta$ over the Atmospheric Radiation Measurement Southern Great Plains (ARM SGP) site, at Oklahoma, US, thoroughly analyze and parameterize it based on the measurements from 37 days in 2009.

## Methodology

### *Estimating mixing layer height*

Mixing Layer Height (MLH) was determined using 3 methods to set the limiting height for vertical profile of $\beta$. Ideally the atmosphere is homogeneously mixed below MLH.

**Balloon borne sounding system (SONDE)**

Balloon sounding provides vertical profile of weather parameters upto 28 km altitude 4 times a day at the ARM mobile facility. The temperature and pressure data from SONDE were used to determine the potential temperature ($\theta = T(\frac{P}{P_0})^{0.286}$), which remains practically unchanged ($i.e., \frac{\partial\theta}{\partial z} \sim 0$) within the MLH due to equal temperature lapse rates of the air parcel ($\Gamma$) and the ambience ($\gamma$), i.e., adiabatic. The atmosphere becomes stable (i.e., $\frac{\partial\theta}{\partial z} > 0$) above MLH with $\Gamma$ larger than $\gamma$ [*Rogers and Yau*, 1988].

**Lapse rate equation**

The clouds are often formed above the Lifting Condensation Level Height ($h_{LCL}$) as the air becomes completely saturated through adiabatic lifting. The stable layer within the cumulous cloud [*Zeng et al.*, 2004] and the inversion from the latent heat [*Tjernström*, 2007] act as a turbulence barrier near its cloud base [*Wang et al.*, 2014]. So the MLH is often substituted by the height of cumulous cloud base [*Stull*, 1988], which can be calculated from the ratio of difference between air temperature ($T_{sfc}$) and dew point temperature ($T_{d\_sfc}$) at surface to their corresponding lapse rates (Equation 10).

$$Cloud\ base\ height\ (m) = h_{LCL} = \frac{T_{sfc} - T_{d\_sfc}}{\Gamma - \Gamma_d} \quad (10)$$

Where, $\Gamma$ is dry adiabatic lapse rate and $\Gamma_d$ dew point lapse rate.

**Backscatter profile**

As aerosols are mostly emitted from/ near the surface, their concentration is much higher within the MLH than in the free troposphere. The top of MLH can be detected by a drastic decrease in vertical gradient of backscatter profile [*Hayden et al.*, 1997; *Flament et al.*, 1997; *Menut et al.*, 1999; *Steyn et al.*, 1999; *Wulfmeyer et al.*, 1999; *Cohn and Angevine*, 2000; *Davis et al.,* 2000; *Münkel and Päsänen*, 2004; *Schäfer et al.*, 2004, 2005; *Münkel et al.*, 2007]. The backscatter data was obtained from a ground based Raman lidar (RL) transmitting electromagnetic radiation at different angles and direction, determining the 3-dimensional distribution of the aerosols, and measuring the scattered back radiation fraction.

*Vertical profile of T*

The weather data (e.g., $T, RH$) are recorded by a sensor above the 60m tower at ARM SGP site. Assuming $\Gamma$ = 0.0098℃/$m$, the vertical profile of $T$ was created from 60m to the top of the ML.

*Vertical profile of $T_d$*

First the saturation vapor pressure ($e_s$) was determined from the measured $T$ at height $z$ (i.e., 60m here) using *Lowe and Ficke*'s equation [1974].

$$|e_s|_z = |a_0 + a_1 T + a_2 T^2 + a_3 T^3 + a_4 T^4 + a_5 T^5 + a_6 T^6|_z \quad (11)$$

Where, $a_0$= 6.108, $a_1$= 4.437 x $10^{-1}$, $a_2$ = 1.429 x $10^{-2}$, $a_3$= 2.651 x $10^{-4}$, $a_4$= 3.031 x $10^{-6}$, $a_5$= 2.034 x $10^{-8}$, and $a_6$ = 6.137 x $10^{-11}$.

At altitude $z$, actual vapor pressure, $|e|_z$, was calculated as $|RH * e_s|_z$ and $|f(T_d)|_z$ was calculated assuming an array of $T_d$ ranging from 0 to T℃. The actual $|T_d|_z$ at $z$ was considered as the one corresponding to least difference between $|e|_z$ and $|f(T_d)|_z$.

$$|least\ error|_z = \left|minimum\left[absolute\left\{{}^{T}_{T_d = 0}(e - f(T_d))\right]\right|_z \quad (12)$$

Where, $f(T_d)$ is $(a_0 + a_1T_d + a_2T_d^2 + a_3T_d^3 + a_4T_d^4 + a_5T_d^5 + a_6T_d^6)$ for assumed values of $T_d$. Considering $\Gamma$ as 0.0098℃/$m$, and $\Gamma_d$ as $6.3 * 10^{-6}\frac{T_d^2}{T}$, $T$ and $T_d$ were calculated at $z + \Delta z$ as ($|T|_{(z+\Delta z)} = |T|_z + \Gamma$), and ($|T_d|_{(z+\Delta z)} = |T_d|_{(z)} + \Gamma_d$), respectively, which was repeated for each incremental height, $\Delta z$, upto the top of the ML.

*Vertical profile of RH*

At $z$, $RH$ was determined from the ratio $\frac{e}{e_s}$, where $e$ and $e_s$ were calculated from *Lowe and Ficke'*s equation [1974] using the values from vertical profile of $T_d$ and $T$ respectively. For $RH$ too, the $z$ ranged from 60m till the top of ML.

*Calculation of $\beta$*

The $\beta$ was calculated using Mie scattering based on 37 days of data between 11:30am to 5:30pm CST or shorter time span when the air was well mixed. The optical properties are determined using Mie scattering theory. The Mie scattering demo program was originally created by Martin Fierz (http://www.fierz.ch/programs.htm ) in 2005 using P.J. Flatau's (1998) C version of the Bohren and Huffman code (1983). By employing the refractive index (m) and size parameter ($\frac{\pi D}{\lambda}$) of an assumed spherical aerosol as inputs, the optical properties of the aerosol and the angular distribution of the scattered light are estimated. The size distribution measurement from 12 – 740 nm and hygroscopic growth factor distribution of 13, 25, 50, 100, 200, 400 and 600 nm particles are used to determine m of aerosols for which the inorganic component is assumed to be made of ammonium sulfate. The organic carbon to elemental carbon ratio is assumed as 9:1.

**Correlation between β and RH**

$RH$ affects scattering of the particles through their hygroscopic growth. *Im et al.* [2001] established the correlation between backscattering and $RH$ which is similar to the correlation with other optical properties (e.g., upscattering coefficient ($b_{ups}$), total scattering ($b_{scat}$)) as well. In order to determine β as a function of RH, an array of RH (i.e., 24, 59, 77, 86, 90, 92.5, 94, 95, and 95.7%) was chosen for which the change in $b_{ups}$ or $b_{scat}$ with respect to two consecutive RHs remains roughly constant.

**Vertical profile β at atmospheric RH**

Within the well mixed layer, the change in aerosol number concentration (N) as well as the $b_{ups}$ and $b_{scat}$ was assumed to be proportional to the air density ($\rho$). At altitude $z$, the $b_{ups}$ and $b_{scat}$ were then adjusted to the actual atmospheric $RH$ to consider its effect on particle size and $\beta$.

$$|\beta|_{z\ @\ atmospheri\ \ RH} = \frac{\left|b_{ups\_0} * \frac{P_z T_0}{P_0 T_z}\right|_{RH}}{\left|b_{scat\_0} * \frac{P_z T_0}{P_0 T_z}\right|_{RH}} \quad (13)$$

Where, $\frac{P_z}{P_0} = \exp(-\frac{Z}{scale\ height})$ and $\frac{T_0}{T_z}$ was obtained from $(T_z = T_0 + \Gamma * z)$ at each incremental height.

**Diurnal profile of β**

Diurnal profile of β was created at 60m from ground during time when the air below MLH was well mixed.

**Seasonal profile of β**

Seasonal profile of β was created by averaging it over height upto top of the ML and time of day for 37 days selected between March and October. During those days the mixing layer height derived from the three methods were comparable and the boundary layer was deep and well mixed.

$$\bar{\beta} = \frac{\sum_0^n (\sum_0^m \frac{\beta_j}{m+1})_i * \cos(90 \quad \theta_{0i})}{\sum_0^n \cos(90 \quad \theta_{0i})} \tag{14}$$

Where, m is number of incremental height and n number of measurements in a day.

*Correlating with other variables using Principal component analysis (PCA)*

Principal component analysis or PCA is a multivariate statistical technique, which fit an n-dimensional ellipsoid to a dataset, for which each axis is a principal component (PC). It is based on singular value decomposition which is equivalent to eigen value decomposition in linear algebra. PCA was applied to reduce the dataset dimension, find the number of significant PCs, select the component for which β has higher coefficient and find variables which have stronger correlations with β in order to parameterize it. The dataset was eventually re-expressed in terms of PCs without changing its original relationship and presented using the primary visualization tool, biplot. In a biplot, the axes, points and the vectors represent a pair of PCs, score of observations and the coefficients of the variables on PCs, respectively.

## Result and discussion

The work is based on the measurements from 37 days chosen from March to October in 2009, when the boundary layer was well mixed.

*Estimating mixing layer height (MLH)*

MLHs from 3 different methods are presented together in Figure 20 on 20th September, 2009.

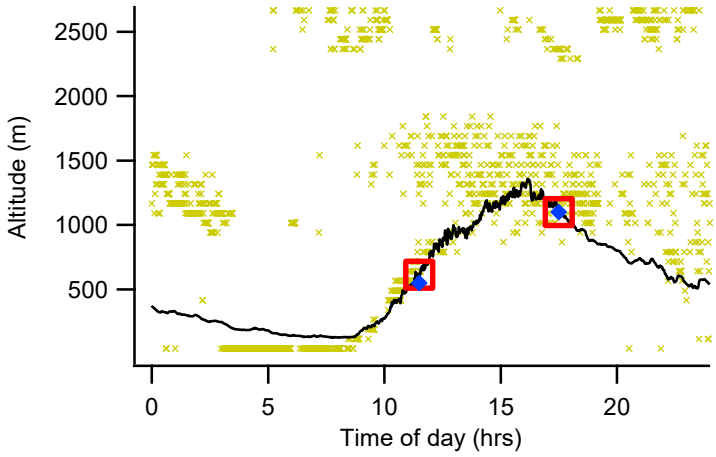


**Figure 20. Mixing height from 3 different methods on 20th September, 2009. The blue markers represent MLH at 11:30am and 5:30pm from potential temperature profiles. The black line shows MLH from lapse rate equation; and green markers represent derived MLH from backscatter profile. The red boxes indicate the averaged MLHs from all three approaches.**

Sometimes the cloud base height was lower than the MLH calculated from the backscatter profile. A closer look revealed that the backscatter coefficient increased abruptly on those occasions right above the cloud base apparently due to larger cloud activated particles. Extending the MLH by 100-200 m above the cloud base level enabled to capture 100% of the backscatter/ aerosol scattering ratio/extinction coefficient during 40% observations and above 70% during 67% observations, indicating possible presence of high altitude aerosols (Figure 20) during many observations. When there were visible differences between MLH from backscatter profile and the cloud base

height, MLH was considered equivalent as the latter to diminish the error from cloud activated aerosols or high altitude aerosols.

*Vertical profile of T, $T_d$ and RH*

The vertical profiles of $T$, $T_d$ and RH around 1 PM on 20th September, 2009, are plotted in Figure 21. The $T$ decreases at a faster rate than $T_d$ and becomes equal at condensation level (CL) where the air is fully saturated.

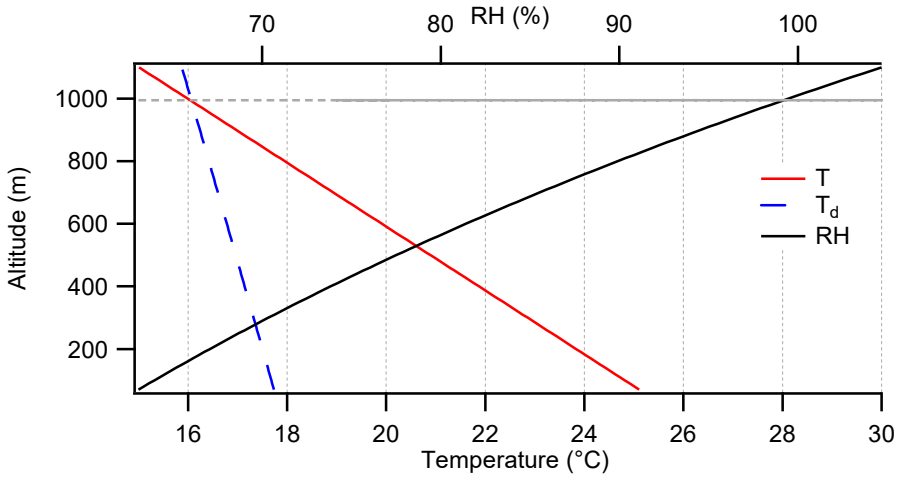


**Figure 21. Vertical profile of RH at 1 PM on 20th Sep, 2009. The gray dashed line around 1 km altitude denotes CL height.**

*Calculation of $\beta$*

**Vertical profile at atmospheric RH**

The vertical profile of $\beta$ is a function of vertical distribution of water vapor and aerosol concentration. Assuming the relative amount of different aerosol species as

constant throughout the altitude and the change in aerosol number concentration proportional to the air density within the MLH, $b_{ups}$, $b_{scat}$ and $\beta$ were calculated at each incremental $z$ and atmospheric RH.

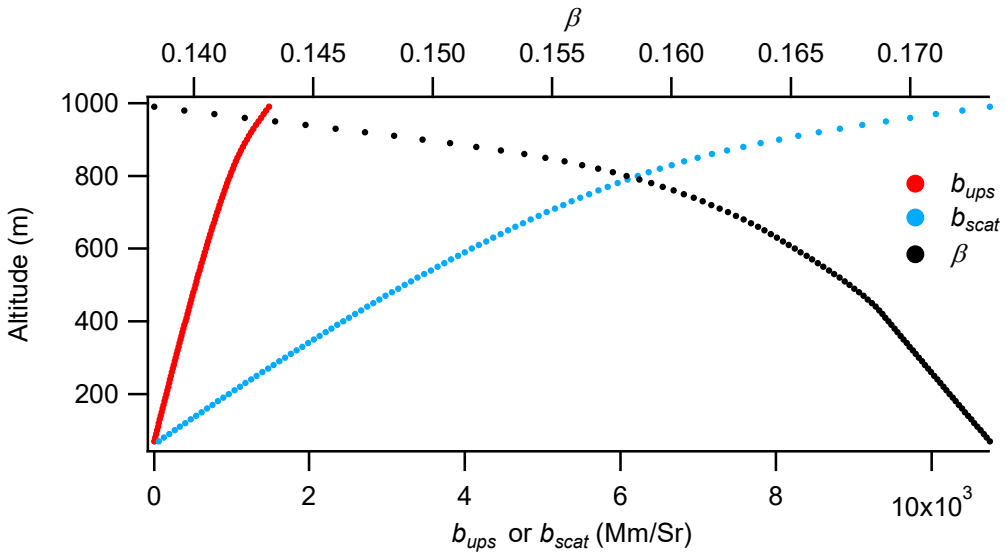


**Figure 22. Vertical profile of $b_{ups}$, $b_{scat}$ and β around 1 PM on 20th September, 2009.**

While both $b_{ups}$ and $b_{scat}$ increase with altitude undermining the effect of slowly declining aerosol concentration, the change is much higher for $b_{scat}$ due to increased forward scattering from enlarged aerosols at higher RH. As a result $\beta$ decreases much faster at higher altitude (Figure 22). Similar results can be seen at other locations too [*Porter et al.*, 2003; and *Magi et al.*, 2003] except at places with exceptionally dry air or mostly non-hygroscopic aerosols.

**Diurnal profile of β**

Time of the day affects the optical properties through the variation in RH profile and the solar position. The time span considered for the diurnal profile was the least between i) time span used during MLH estimation and ii) 11:30 AM to 5:30 PM. The variations in $b_{ups}$, $b_{scat}$ and $\beta$ are shown in Figure 23.

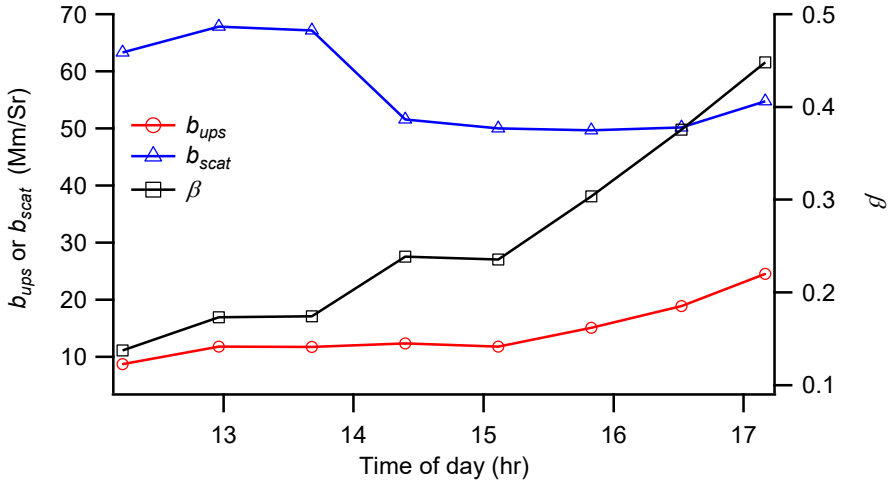


**Figure 23. Variation of $b_{ups}$, $b_{scat}$ and β between 11:30 AM to 5:30 PM at 60m from ground on 20th Sep, 2009.**

The variation in $b_{scat}$ and $b_{ups}$ in Figure 23 can be partially explained by the variation in number concentration of aerosol on 20th September, 2009 as the dominant particle size mode (i.e., 0.1-0.2 µm), and its GF (i.e., 1.35 and 1.45 for 0.1 µm and 0.2 µm respectively) remained practically unchanged for the selected time span. But $b_{ups}$ and resultant $\beta$ were largely influenced by solar elevation, φ (i.e., 90°- $\theta_0$). As observed by *Nemesure et al.* [1995], $\beta$ approaches maxima when the sun nears the horizon. The

calculation of $b_{scat}$, $b_{ups}$ and $\beta$ was continued upto top of MLH to combine the effects of height (f(RH)) and time of the day (f(RH, φ)) as presented in Figure 24.

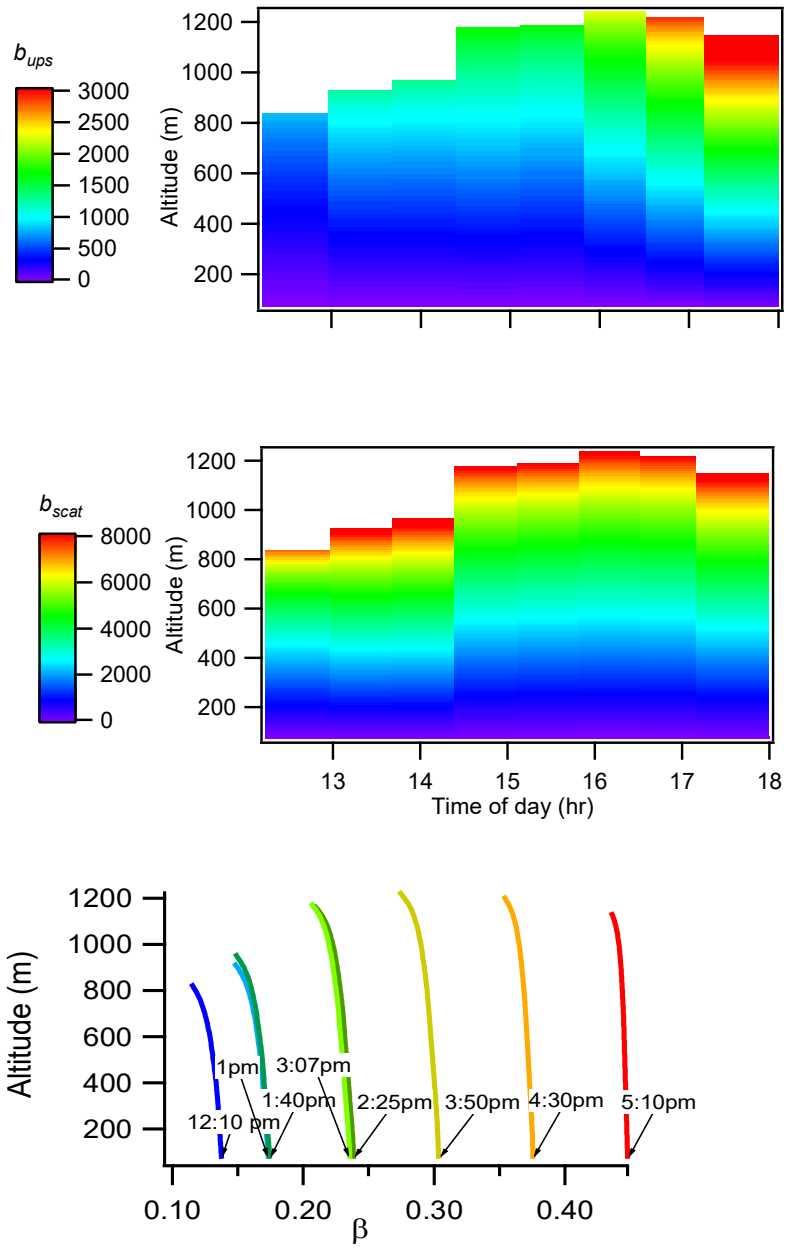


**Figure 24. Variation of $b_{ups}$ (top), $b_{scat}$ (middle) and β (bottom) with altitude from 11:30 AM to 5:30 PM on 20th Sep, 2009.**

**Seasonal profile of β**

Seasonal variation in $\beta$ is affected mostly due to the change in φ, which is relatively higher during the summer as is shown in Figure 25. For a given day the averaged $\beta$ or $\bar{\beta}$ was determined by averaging it over the altitude followed by the cosine of φ. As expected the higher summer time φ resulted in lower $\bar{\beta}$.

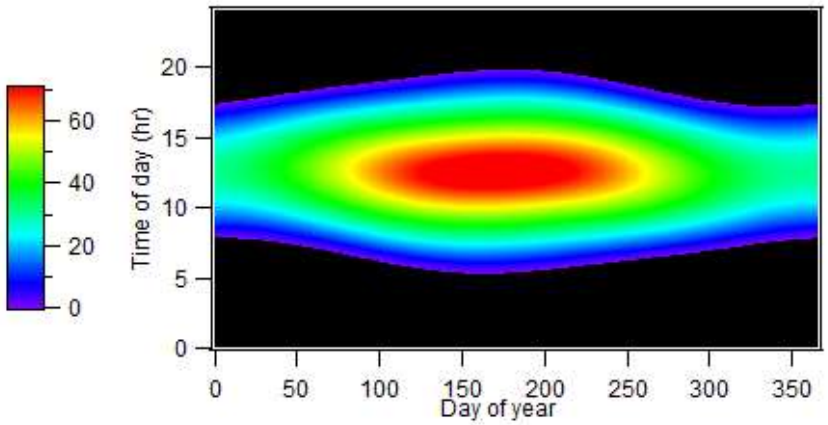


**Figure 25. Seasonal change in φ at SGP site. Along y scale, the change from black to blue and blue to black signify the time of sunrise and sunset respectively. The z scale displays the magnitude of φ.**

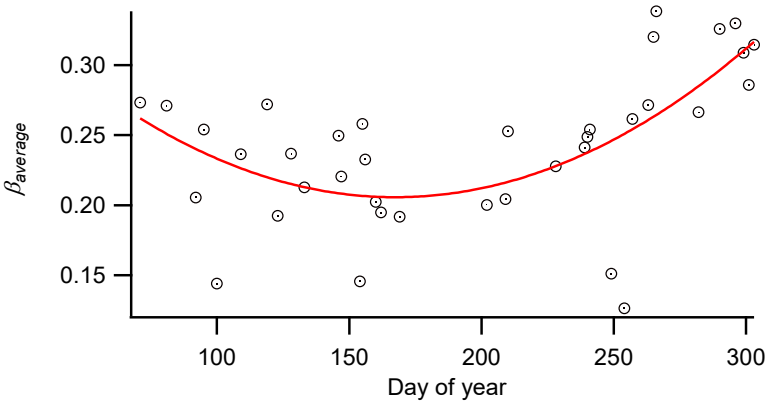


**Figure 26. Variation in average β in 2009 based on 37 days of measurements.**

*Correlating β with other variables*

Several variables were selected to parameterize $\beta$ including $b_{ups}$, $b_{scat}$, cos φ, f(RH) ($= \frac{Scattering\ coeff_{85\%\ RH}}{Scattering\ coeff_{40\%\ RH}}$), average dry size, average GF at 90% RH ($= \sum n_i GF^3)^{1/3}$ and total volume within 50nm - 1μm size, which might have potential effect on $\beta$. PCA analysis on 37 days of data suggested that $\beta$ has the strongest relation with cos φ. So, initially the correlation between β and cos φ was examined. The goodness of fitting, $r^2$ was 0.8748. Regardless of the particle size, the spread of the distribution was narrower during the evening due to increasingly symmetric scattering and broader when position of sun was higher in sky.

$$\beta = 0.064*\exp(1.8445* \cos \varphi),\ r^2 = 0.8748 \quad (15)$$

As β is a ratio of $b_{ups}$ and $b_{scat}$, which are related to particle volume, size, and hygroscopicity, the wet particle size ($d_{dry}$*GF) was included in the fitting equation to improve the correlation.

$$\beta = 0.1141*\exp(1.4661*\cos\varphi^{(1.2+\exp(d_{dry}*GF))},\ r^2 = 0.9143 \quad (16)$$

The $r^2$ was improved instantly by 4% following the inclusion of $d_{dry}$*GF.

However, particles near surface are only occasionally exposed to as high as 90 %RH at which their hygroscopic expansion could be significant (Figure 27). During the selected 37 days in 2009, 30 minutes average RH reached 90% or higher only 15% of the times.

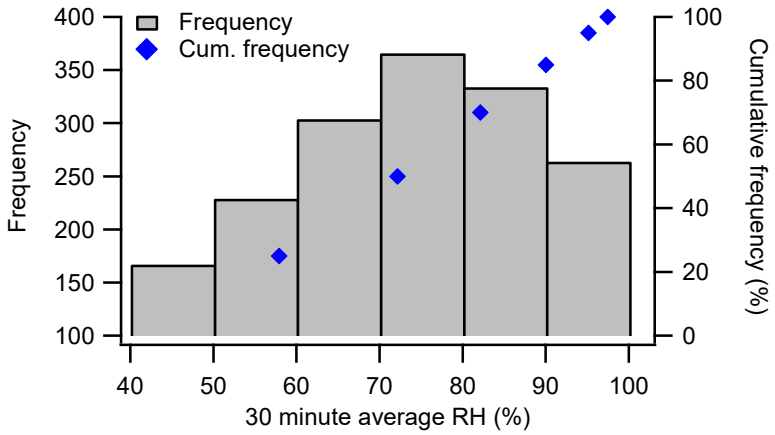


**Figure 27. 30 minute average RH at 60m from surface on 37 days in 2009.**

In order to get rid of the hygroscopicity related error, the relation was re-established using β at 24% RH ($\beta_{dry}$) and average dry size ($d_{dry}$).

$$\beta_{dry} = 0.0789*\exp(1.6805*\cos\varphi),\ r^2 = 0.914 \quad (17)$$

$$\beta_{dry} = 0.1278*\exp(1.3464*\cos\varphi^{(1+\exp(d_{dry}))}),\ r^2 = 0.9407 \quad (18)$$

Similar to previous step, considering average dry size improved the $r^2$ by 3%. In conclusion, β can be estimated reasonably using variables; such as aerosol size and solar elevation.

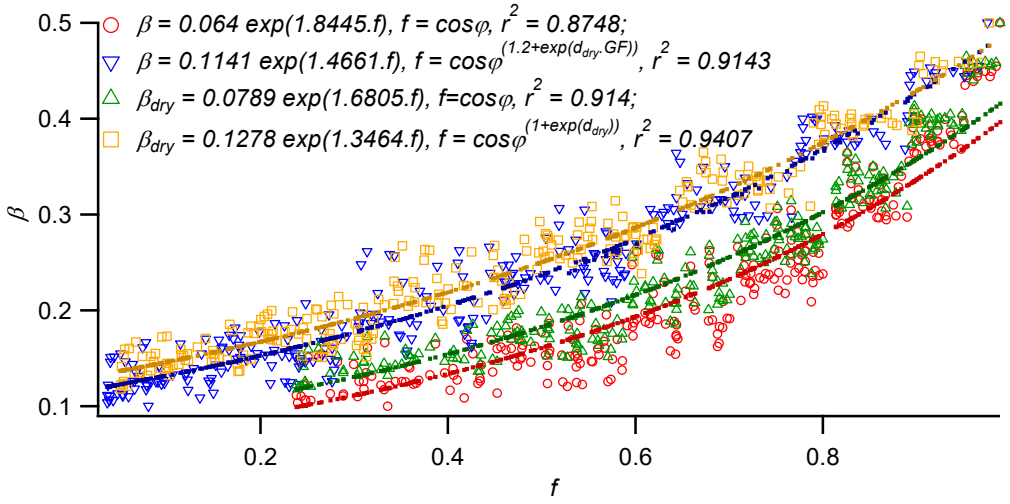


**Figure 28. Parameterization of β.**

## Summary

The particle size distribution and size resolved hygroscopicity distribution data were measured with a DMA/TDMA system on selected 37 days in 2009 when the boundary layer was well mixed at the ARM SGP site and were used to create the vertical profile of upscatter coefficient ($b_{ups}$), scattering coefficient ($b_{scat}$) and upscatter fraction (β). All the optical properties mentioned were first calculated at 60 m height from ground using Mie theory and then adjusted at each incremental height for change in the air density and RH. The variation in particle concentration and size influenced the variation in $b_{scat}$ and $b_{ups,}$ which was evident in their vertical profile. But, it is the solar position which largely influenced the β and partially the $b_{ups}$. The vertical profile displayed decreasing β with altitude due to increased forward scattering from larger particles. The greater variation in β however was observed in diel scale with the largest value coinciding the time nearing sunset due to symmetry in scattered radiation

distribution. The seasonal profile of β is also a function of solar position showing lower values during the summer and higher values in the winter. While solar position alone can explain the variation in β quite well, inclusion of particle size has improved the parameterization significantly.

# CHAPTER VI

# INFLUENCE OF AEROSOL COMPOSITION AND MIXING STATE ASSUMPTIONS ON CCN CONCENTRATION ESTIMATION

## Introduction

Aerosol particles activate to form cloud droplets when they encounter a supersaturation, $S$, that exceeds their size-and composition-dependent critical supersaturation, $S_c$. Those particles with $S_c$ less than the relevant local, instrumental, or prescribed $S$ are called cloud condensation nuclei or CCN. Particles composed of soluble inorganic species are usually more hygroscopic than those composed of organic species and thus are more efficient nuclei. For particles of any composition, $S_c$ decreases and CCN "activity" increases with increasing particle size. Thus, variation in both the size distribution and the chemical composition of an aerosol significantly affects CCN concentration.

Particle $S_c$ can be determined for inorganic species using Köhler Theory, provided the physico-chemical properties (e.g., size, hygroscopicity) of the solutes are known [*Köhler*, 1936]. However, atmospheric aerosols frequently contain a significant amount of organic material as well [*Hallquist et al.*, 2009; *Pennington et al.*, 2013]. In several studies, particles composed entirely of organic species have been reported to be largely ineffective in droplet formation [*Abbatt et al.*, 2005; *Prenni et al.*, 2007]. But the solubility and surface tension-reducing properties of the organic component can sometimes have significant influence on $S_c$ [e.g., *Bigg*, 1986; *Roberts et al.*, 2002; *Smith*

*et al.*, 2008; *Yli-Juuti et al.*, 2011; *Raymond and Pandis*, 2002, 2003; *Chan et al.*, 2008]. Extended Köhler Theory can reasonably predict CCN concentration with knowledge of the size distribution and chemical composition of a multi-component aerosol [*Raymond and Pandis*, 2002, 2003; *Bilde and Svenningsson*, 2004; *Hartz et al.*, 2006; *Svenningsson et al.*, 2006]. Introduction of a single hygroscopicity parameter by *Petters and Kreidenweis* [2007] has simplified description and comparison of hygroscopicity and CCN activity for particles composed of single or multiple inorganic and organic species [*Moore et al.*, 2011].

CCN concentration is also dependent on aerosol mixing state. Previous closure studies have shown that assumption of an internal mixture generally results in an overestimate of the CCN concentration and assumption of an external mixture in an underestimate [*Mircea et al.*, 2002; *Broekhuizen et al.*, 2006; *Rissler et al.*, 2006; *Roberts et al.*, 2006; *Medina et al.*, 2007; *Cubison et al.*, 2008; *Furutani et al.*, 2008; *Kuwata et al.*, 2008; *Quinn et al.*, 2008; *Shantz et al.*, 2008; *Wang et al.*, 2008; *Bougiatioti et al.*, 2009; *Chang et al.*, 2010; *Gunthe et al.*, 2009; *Lance et al.*, 2009; *Kammermann et al.*, 2010; *Roberts et al.*, 2010; *Rose et al.*, 2010; *Wang et al.*, 2010]. However, assumption of either mixing state leads to reasonable results for aged aerosols [*Ervens et al.*, 2010]. While inclusion of mixing state [*Broekhuizen et al.*, 2006; *Cubison et al.*, 2008; *Lance et al.*, 2009; *Padró et al.*, 2012] and chemical composition [*Medina et al.*, 2007; *Stroud et al.*, 2007; *Cubison et al.*, 2008; *Gunthe et al.*, 2009; *Murphy et al.*, 2009] can increase the accuracy with which CCN concentration can be estimated, both can be highly variable with time and with particle size, and are often unavailable with

current measurement techniques and not easily incorporated into aerosol descriptions used in models. Moreover, chemical composition and mixing state are greatly simplified in large scale models, e.g., inorganic/organic, internal/external. Supporting such treatment, several studies have shown that CCN concentration is most sensitive to the aerosol size distribution [*Conant et al.*, 2004; *Dusek et al.*, 2006], and the assumption of internal mixing has resulted in fairly accurate predictions [*Liu et al.*, 1996; *Cantrell et al.*, 2001; *Roberts et al.*, 2002; *VanReken et al.*, 2003; *Rissler et al.*, 2004; *Broekhuizen et al.*, 2006; *Chang et al.*, 2007; *Ervens et al., 2007*; *Wang et al., 2008*; *Gunthe et al., 2009*]. *Ervens et al.* [2007, 2010] reported that description of the mixing state is relatively more important than that of the size-resolved chemical composition. Other studies suggest detailed information of size distribution, chemical composition, and mixing state is important for achieving closure among aerosol and CCN measurements [*Mircea et al.*, 2005; *Medina et al.*, 2007; *Stroud et al.*, 2007; *Cubison et al.*, 2008; *Lance et al.*, 2009; *Quinn et al.*, 2008; *Asa-Awuku et al.*, 2011].

In this study, measured size-resolved concentration and subsaturated hygroscopicity were used to estimate CCN concentration using an array of assumptions for composition and mixing state. CCN spectra (CCN concentration vs. $S_c$) were first derived using the computationally expensive technique described by *Gasparini et al.* [2006] in which measured hygroscopicity and size distributions are combined to create an $S_c$ matrix with thousands of elements. The resulting CCN concentrations calculated by integrating over $S>S_c$were then compared to direct measurements and with CCN concentration calculated using alternate approaches and assumptions.

## Measurements

**Table 1. List of instruments, measured quantities, manufacturer, and active years**

| Instrument | Measurement | Manufacturer / Model | Active years |
|---|---|---|---|
| Scanning Mobility Particle Sizer (SMPS; part of the "TDMA" system) | Size distribution from 12 to 760 nm diameter ($D$) | Fabricated, Texas A&M University | 2005 - present |
| Hygroscopic Tandem Differential Mobility Analyzer (HTDMA; part of the "TDMA" system) | Hygroscopic growth factor distributions of 13, 25, 50, 100, 200, 400,and 600 nm $D$ particles at 90% RH | Fabricated, Texas A&M University | 2005 - present |
| Cloud Condensation Nuclei counter (CCNc) | CCN concentration at a fixed set of supersaturations | Droplet Measurement Technologies | 2009 - present |
| Condensation Particle Counter (CPC) | Concentration of $D$> 10 nm particles | TSI Inc. 3010 | 1996 - present |
| Aerosol Chemical Speciation Monitor (ACSM) | Bulk chemical composition (organics, sulfate, nitrate, ammonium, and chloride) | Aerodyne Research, Inc. | 2011 - present |

## Screening and time interval selection

Data from individual sources were validated separately and periods having erroneous data or no data were excluded from analysis. Data from time periods during which instrument problems or failure was evident in the data or when one of the following occurred were not used:

a. The measured CCN concentration ($N_{CCN}$) exceeded the total particle concentration ($N_{CN}$), possibly due to malfunction of the CCNc,

b. The sample flow entering the upstream (1$^{st}$) DMA had an RH>30%, or

c. The sample flow entering the downstream (2nd) DMA had an RH< 85%.

The categorized data quality during the period of analysis is shown in Figure 29. During times when the absolute averaged fractional error between $N_{CN}$ measured by the CPC and that calculated by integrating the SMPS-measured size distribution ($AAFE = \frac{N_{CN\ measured} - N_{CN\ calculated}}{N_{CN\ measured}}$) was higher than 0.05, the estimated $N_{CCN}$ was multiplied by a correction factor calculated by averaging $\frac{N_{CN\ measured}}{N_{CN\ calculated}}$ from all measurements made after 7 p.m. when the aerosol size distribution is observed to be relatively stable at the site.

$$N_{CCN\ calculated\_corr} = \left(\frac{N_{CN\ measured > 7p.m.}}{N_{CN\ calculated\ \ 7p.m.}}\right)_{average} * N_{CCN\ calculated} \quad (19)$$

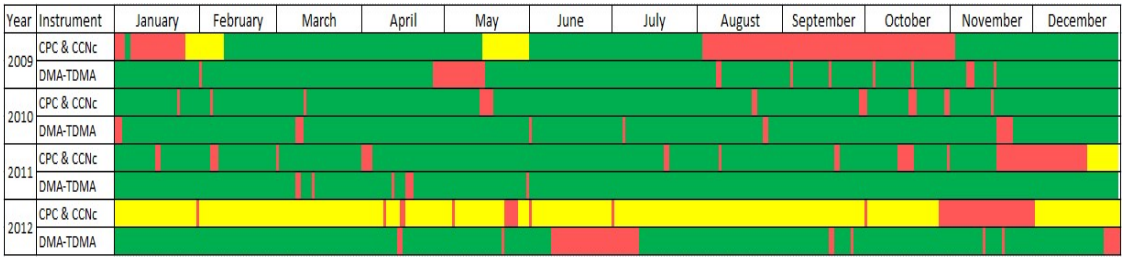


**Figure 29. Data quality during the analysis period. Periods during which data are available and no significant problems were identified are green, those during which confidence in at least some subset of the data is low are yellow, and those during which data are unavailable or thought to be erroneous are red.**

## Chemical composition analysis

Bulk aerosol chemical composition for particles with aerodynamic diameter less than 1μm has been measured at SGP since 2011. Measured chemical species include ammonium, sulfate, nitrate, chloride, and non-refractory organics. Ammonium

commonly exceeds that required to neutralize the observed sulfate and nitrate throughout the year. Its abundance is largely associated with fertilizer application and husbandry, similar to that found by *Nemitz et al.* [2009] at another agricultural site. Local sulfate concentrations are occasionally enhanced when the site is within the plume of the nearby Sooner Lake coal-fired power plant. Organics comprised an average of 56% of the total mass concentration between 2011 and 2013 (Table 2). According to *Fast et al.* [2013], the fractional contribution of organics to the overall mass concentration is highest in the summer. Secondary organic aerosol precursors are not well characterized at SGP, but likely are mostly biogenic with significant contributions from urban pollution when the site is directly within the plume of cities such as Oklahoma City (140 km S), Tulsa, OK (150 km SE), and Dallas, TX (440 km S). Local and regional agricultural burning also contributes to the organic aerosol concentration. Seasonal variation in all these species causes variation in aerosol properties and concentration and, consequently, in $N_{CCN}$.

**Table 2. Percent of total mass concentration**

| Year | % of total mass | | |
|---|---|---|---|
| | Total organics | Ammonium sulfate | Ammonium nitrate |
| 2011 | 57 | 17 | 26 |
| 2012 | 56 | 18 | 26 |
| 2013 | 56 | 24 | 20 |

Annually-averaged mass concentration fractions of sulfate and nitrate at the site are comparable, with sulfate more abundant from April through October and nitrate from November through March (Figure 30).

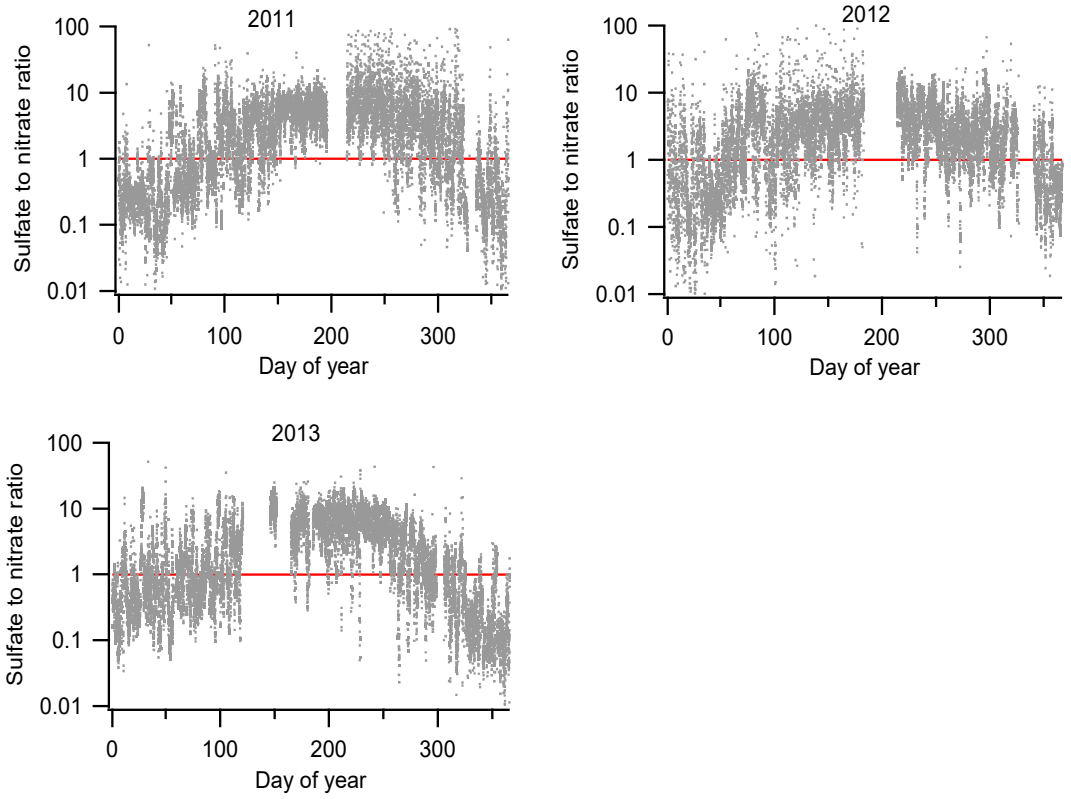


**Figure 30. Sulfate to nitrate equivalent concentration ratio based on the chemical composition data from 2011(top, left), 2012 (top, right), and 2013 (bottom). DOY = day of year, and equivalent concentration =molar concn./equivalence factor, where equivalence factor for sulfate and nitrate are 0.5 and 1, respectively.**

Inorganic nitrate aerosol is formed primarily through gas phase oxidation of nitrogen dioxide, followed by combination with species such as ammonium, or through heterogeneous reactions on existing aerosol surfaces. Ammonium preferentially combines with sulfuric acid and then with nitric acid to produce ammonium sulfate (AS) and ammonium nitrate (AN), respectively. The high nitrate concentration in the winter may be attributed to increased stability of AN at lower temperatures, which is supported by the strong correlation between excess ammonium (i.e., remaining ammonium after neutralizing available sulfate) and nitrate shown in Figure 31.

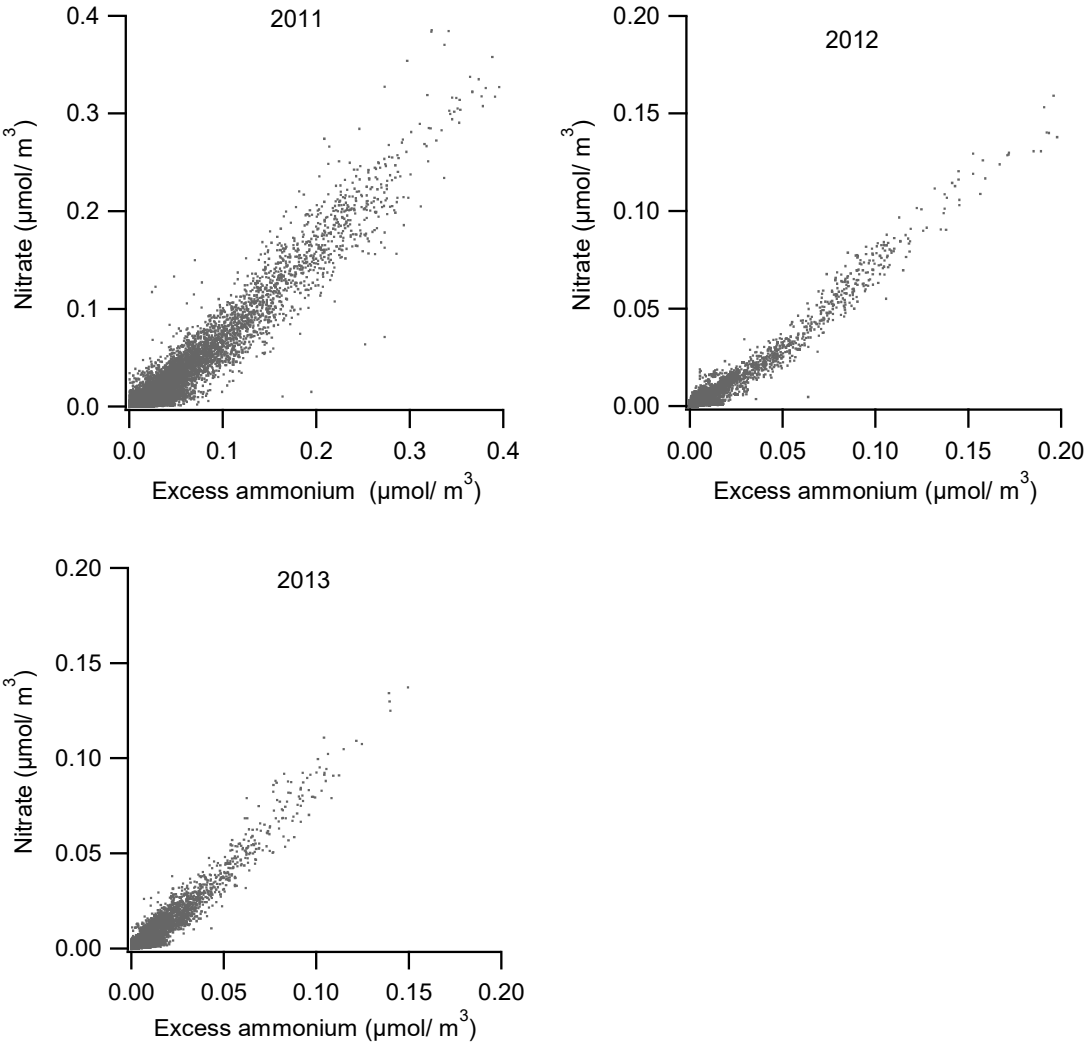


**Figure 31. Excess ammonium vs. nitrate equivalent concentration from chemical composition data in 2011 (top, left), 2012 (top, right), and 2013 (bottom).**

### Determining the hygroscopicity parameter or kappa of organics ($k_{org}$).

As aerosol organic components at SGP site are not well characterized, direct derivation of $k_{org}$ is not possible. An average $k_{org}$ = 0.1 was used to calculate $N_{CCN}$ for assumed external mixtures as described earlier. Support for this assumption comes from

derivation of $k_{org}$ using measured chemical composition data and size distribution + hygroscopicity distribution data and the mixing rule [*Petters and Kreidenweis*, 2007].

$$k_{org} = \frac{V_{overall}k_{overall} - \left(\frac{m_{AS}}{\rho_{AS}} + \frac{m_{AN}}{\rho_{AN}}\right)k_{inorg}}{\frac{m_{org_{NR}}}{\rho_{org_{NR}}}} \quad (20)$$

Particle volume concentration ($V_{overall}$) and kappa ($k_{overall}$) were obtained directly from measured size distribution and hygroscopicity distribution data. The mass concentration, $m$, of major inorganic compounds (i.e., AS and AN) and non-refractory organics ($org_{NR}$) were calculated from the ACSM-measured chemical composition data. The density, ρ, of AS, AN, and $\mathrm{org_{NR}}$ were assumed to be 1.77$\frac{g}{cm^3}$, 1.72$\frac{g}{cm^3}$, and 1.3$\frac{g}{cm^3}$ [*Nakao et al.*, 2013], respectively. An average kappa for inorganic compounds ($k_{inorg}$) of 0.6 was assumed.

The resulting seasonal profiles of $k_{overall}$ and $k_{org}$ in 2011 are shown in Figure 32. Unlike the $k_{org}$ profile, $k_{overall}$ was highest in the winter and lowest in the summer. The high wintertime $k_{overall}$ is a result of high concentrations of inorganic compounds, especially nitrate, while the relatively low summertime $k_{overall}$ is caused by higher organic mass concentrations, as shown in Figure 33. Positive Matrix Factorization (PMF) analysis from the Organic Aerosol Component (OACOMP) Value Added Product (VAP) [*Fast et al.*, 2013] indicates that less-hygroscopic biomass burning organic aerosol (BBOA) was prevalent from February through April in 2011, thus lowering $k_{org}$ in winter and spring. But aged SOA (MO-OOA), which is moderately

hygroscopic, was more abundant in summer, and thus raised $k_{org}$. The $k_{org}$ in the spring and fall lies between that of the winter and summer. Although some seasonal variation in $k_{org}$ is evident in Figure 32, the assumed average value of 0.1 is reasonable for this study.

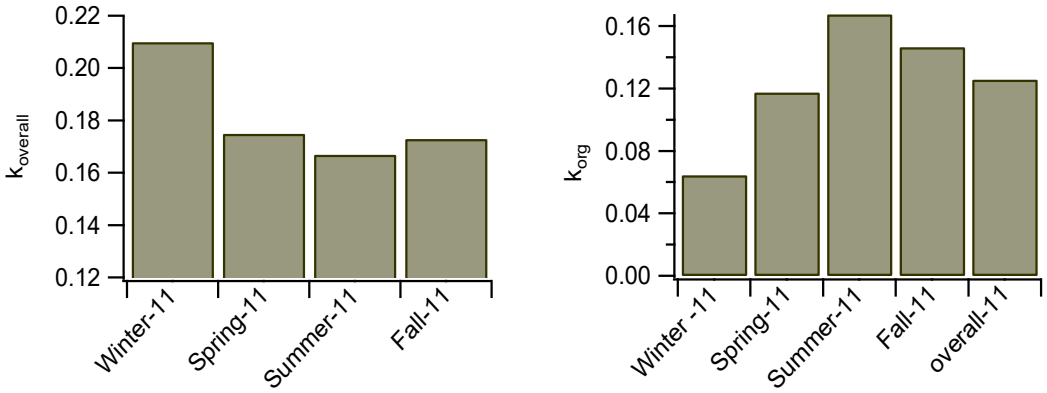


**Figure 32. Seasonal profile of $k_{overall}$ (left) and $k_{org}$ (right) in 2011.**

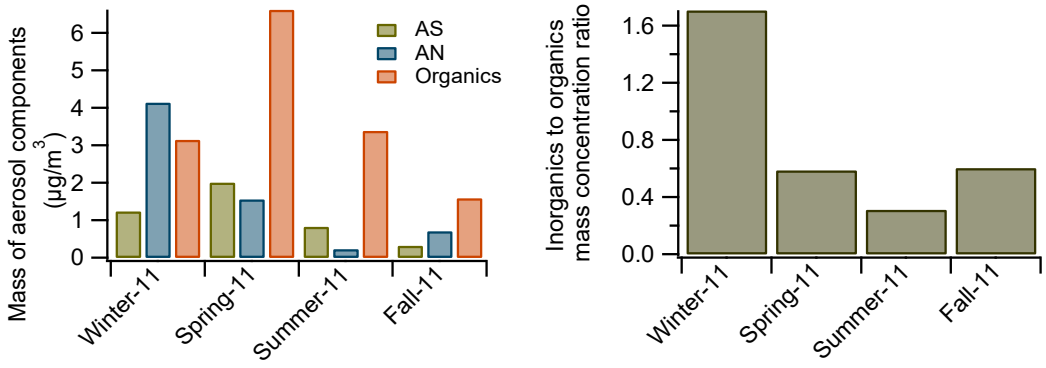


**Figure 33. Seasonal average of inorganic and organic mass concentration in 2011.**

### Determining soluble fraction (SF)

Many atmospheric particles are aqueous solutions of inorganic and/or organic species. They may contain homogeneous mixtures of different species (i.e., all particles in an internal mixture), or a single species (i.e., one type of particle in an external mixture). Some of the approaches used here to estimate $N_{CCN}$ assume the particles are comprised of separate water soluble and insoluble components. The split between the two components is calculated from the hygroscopicity data and is expressed as a soluble fraction, $SF$, which is simply the ratio of soluble, $m_s$, to total, $m_s + m_{in}$, particle mass.

$$SF = \frac{m_s}{m_s + m_{in}} \quad (21)$$

The approach used to relate size-resolved $GF$ to $SF$ is similar to that described in *Gasparini et al.* [2006]. Briefly, an iterative approach is used to determine $SF$ that explains the measured $GF$ for an assumed soluble component (AS here) present in an ideal aqueous solution. This quantity is operationally defined and will not generally reflect the actual soluble content of the aerosol. The mathematical relationships used for the calculations are summarized in TextS1 of the Supplemental Information.

### Description of models used for estimating $N_{CCN}$

The $N_{CCN}$ was estimated by combining the measured size distributions with the size-resolved $S_c$ or $S_c$ distributions calculated using an array of assumptions regarding particle composition and mixing state. The chemical make-up of particles at the ARM

SGP site is complex and highly variable with time and size. For all approaches any aerosol aqueous solution is assumed to be ideal, for which the solute effect and the ionic activity effect on vapor pressure are taken into account. Somewhat arbitrarily, the 'Two-component particles with an aqueous solution surrounding an insoluble core' approach, which is summarized next, is considered as our base model. The results from that model are compared with the directly measured $N_{CCN}$ and with results using other approaches that rely on simplifying assumptions similar to those that might be employed in a climate model. The approaches considered are summarized in Figure 34 and described in the sections that follow.

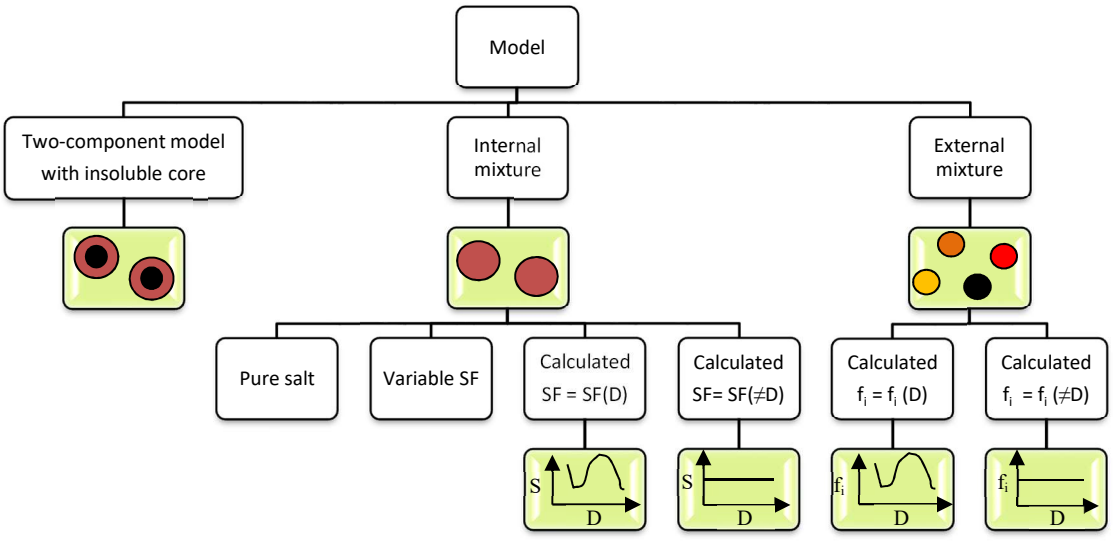


**Figure 34. Overview of the $N_{CCN}$ calculation models.**

*Two-component particles with an aqueous solution surrounding an insoluble core/ Base model*

Each particle is assumed to contain an ideal solution of AS and water surrounding a non-hygroscopic core. The particle number concentration, $N$, and the mass of solute (i.e., AS), $m_s$ (and in turn the $SF$) for the matrix of $D$ and $GF$ pairs were calculated from each set of a measured size distribution and series of $GF$ distributions. A Köhler curve was constructed at each $(D, GF)$ pair for a range in droplet diameter, $D_{drop}$, describing $S$ as a function of $D_{drop}$ ($S(D_{drop})$), with $S_c$ defined as the maximum value along the curve.

$$S(D_{drop}) = \frac{1}{1+\frac{6jm_sM_w}{M_s\rho_w\pi\left(D_{drop}^3-\left(\frac{1}{1+\frac{\rho_{in}}{\rho_s}\left(\frac{SF}{1-SF}\right)}\right)D^3\right)}} \exp\left[\frac{4M_w\sigma_{sol}}{RT\ \ _wD_{drop}}\right] - 1 \qquad (22)$$

Where $M_w$ is the molecular weight of water, $\sigma_{sol}$ the surface tension of the aqueous solution, $\rho_{in}$ the density of the insoluble component, and $\rho_w$ the density of water. The density $\rho_s$ and the molecular weight $M_s$, of the solute AS are $1.77\frac{g}{cm^3}$, and 132 g/mol, respectively. Although the van't Hoff factor $(j)$ in Equation 22 is 3 for a dilute solution with completely dissociated solute AS, a value within 2 – 2.5 results in better agreement between measured and calculated droplet diameters [*Gerber et al.*, 1977; *Kumar et al.*, 2003]. For the current study $j$ was assumed to be 2.3, though using a fixed value introduces some error as *McDonald* [1952] and *Low* [1969] stated that it is a

function of solute molality. The total $N_{CCN}$ at any given $S$ was calculated by summing all $N(D, GF)$ elements for which $S_c(D, GF) < S$.

*Internal mixtures with fixed soluble fraction*

The assumption of pure AS particles almost always results in an upper bound of the estimated $N_{CCN}$. Only in rare instances in which the aerosol is composed almost entirely of even more hygroscopic species with lower $S_c$, such as ammonium bisulfate, would this assumption not be expected to lead to an over-prediction of the actual concentration. Aerosols with variable soluble fraction is similar to the previous approach except the soluble (inorganic) fraction was varied from 20% to 80%.

*Internal mixtures with calculated soluble fraction*

$SF$ was calculated based on the size-resolved hygroscopicity data as discussed earlier.

**Size-dependent soluble fraction (SF(D)) derived from interpolated GF distributions**

The overall kappa ($k_{overall}(D)$) at each size bin was calculated following Equation 23 and used in Equation 24 to calculate $S_c$ and, in turn, $N_{CCN}$.

$$k_{overall}(D) = \left(\frac{1}{1-\frac{\rho_s}{\rho_{in}}\left(1-\frac{1}{SF(D)}\right)}\right) k_{inorg} \quad (23)$$

$S_c$ is obtained by setting the 1st derivative of the Köhler equation to zero.

$$S_c = \exp\left(\frac{4(\frac{4\sigma_{as}M_w}{RT\ \ w})^3}{27D^3k_{overall}(D)}\right)^{1/2} - 1 \quad (24)$$

**Size-independent soluble fraction (SF(≠D)) derived from integrated size and GF distributions**

This is similar to the previous approach except the $SF$ was calculated as a mass concentration-weighted average over the entire size range and the resulting kappa used in Equation 24 to calculate $S_c$.

$$k_{overall} = \left(\frac{1}{1-\frac{\rho_s}{\rho_{in}}\left(1-\frac{1}{SF}\right)}\right)k_{inorg} \quad (25)$$

*External mixtures with calculated particle-type fractions ($f_i$)*

The generalized particle types ($i$) considered are soluble inorganic (AS), soluble organic, and insoluble component (could be organic, soot, dust, etc.).

**Size-dependent particle-type fractions ($f_i(D)$)**

The $SF(D)$ and corresponding $k_{overall}(D)$ were calculated as described earlier. Two scenarios were considered.

*Case 1:* $k_{overall}(D) > k_{org}$

$k_{overall}(D) = f_{org}(D)k_{org} + f_{inorg}(D)k_{inorg}$ and $f_{org}(D) + f_{inorg}(D) = 1$

So, $f_{inorg}(D) = \frac{k_{overall}(D)-k_{org}}{k_{inorg}-k_{org}}$ and $f_{org}(D) = \frac{k_{inorg}-k_{overall}(D)}{k_{inorg}-k_{org}}$

*Case 2:* $k_{overall}(D) < k_{org}$

$k_{overall}(D) = f_{org}(D)k_{org}$ and $f_{org}(D) + f_{in}(D) = 1$

$f_{org}(D) = \frac{k_{overall}(D)}{k_{org}}$ and $f_{in}(D) = 1 - \frac{k_{overall}(D)}{k_{org}}$

For an external mixture at diameter $D$, $f_i = n_i$, where $n_i$ is the number concentration fraction of $i$.

So, $N_{inorg} = N\frac{k_{overall} - k_{org}}{k_{inorg} - k_{org}}$ and $N_{org} = N\frac{k_{inorg} - k_{overall}}{k_{inorg} - k_{org}}$ when $k_{overall} > k_{org}$ (26)

Or, $N_{org} = N\frac{k_{overall}}{k_{org}}$ and $N_{in} = N - N_{org}$ when $k_{overall} < k_{org}$ (27)

At each dry diameter, $D$, the number concentration of inorganic, $N_{inorg}$, soluble organic, $N_{org}$, and insoluble particles, $N_{in}$, were calculated following Equations 26 and 27. The $S_c$ for soluble organic and inorganic particles was determined from Equation 24. At a given $S$, the $N_{CCN}$ from soluble organic ($N_{CCN.org}$) and inorganic particles ($N_{CCN.inorg}$) were calculated separately by integrating for $S_c$<$S$ and then added to calculate the total $N_{CCN}$ (i.e., $N_{CCN} = N_{CCN.inorg} + N_{CCN.org}$).

**Size-independent particle-type fractions ($f_i(\neq D)$)**

Similar to previous one, except the $f_i$ was calculated based on $k_{overall}$ instead of $k_{overall}(D)$.

## Results and discussion

*Comparison between measured and calculated $N_{CCN}$*

Measured $N_{CCN}$ at four fixed supersaturations was compared to that derived following the base model approach. Comparisons were made for all available data from 2009 – 2012. The results for May, 2011 are shown in Figure 35.

The measured and calculated $N_{CCN}$ have similar trends with some deviation. The average Normalized Root Mean Square Errors ($NRMSE$) between the measured and the calculated concentrations for June, 2011 and for each of the four years analyzed are summarized in Table 3.

$$NRMSE = \{\frac{1}{n}\sum_{i=0}^{n-1}\left(\frac{x_i - y_i}{x_i}\right)^2\}^{0.5} \quad (28)$$

Where, $x_i$ is the measured $N_{CCN}$ at a given $S$, $y_i$ the estimated $N_{CCN}$ at the same $S$, and $n$ the number of observations.

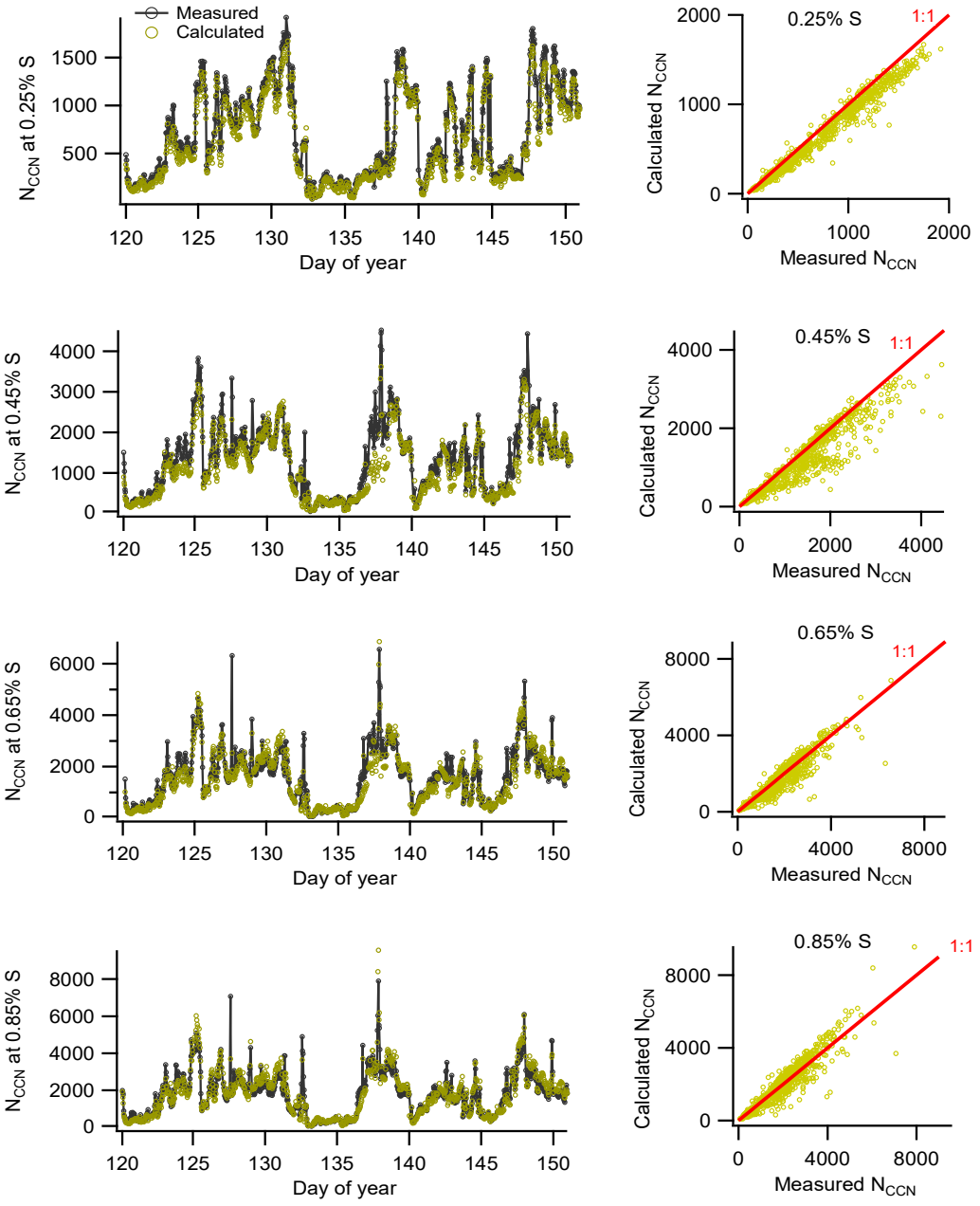


**Figure 35. Comparison between measured and derived $N_{CCN}$ for June, 2011 at 0.25% (top row), 0.45% (2nd row), 0.65% (3rd row), and 0.85 %S (bottom row). DOY = day of year.**

**Table 3. NRMSE at 4 different S from 2009 - 2012 and for June, 2011**

| Year / time | $NRMSE$ @ $\%S$ | | | |
|---|---|---|---|---|
| | *0.25* | *0.45* | *0.65* | *0.85* |
| 2009 | 0.74 | 0.41 | 0.4 | 0.41 |
| 2010 | 0.26 | 0.2 | 0.2 | 0.2 |
| **June, 2011** | **0.19** | **0.18** | **0.19** | **0.21** |
| 2011 | 0.25 | 0.22 | 0.22 | 0.24 |
| 2012 | - | 0.28 | 0.29 | 0.28 |

From 2010 to 2012, the $NRMSE$ is less than 0.3 at each $S$. The error is higher at the lowest $S$ but roughly constant across the other three. In addition to measurement error, some possible reasons for deviations between the measured and calculated concentrations are i) differences in assumed and actual properties of aerosol chemical species, ii) interactions among components not captured by the simplistic solution-over-insoluble-core model, iii) the presence of low solubility organics that dissolve under the dilute conditions with $S \sim S_c$ but not in the more concentrated solution in the TDMA at 90% RH, and iv) the presence of particles that contain slowly dissolving compounds or that are in an amorphous/glassy state for which hygroscopic growth and activation timescales may be comparable to or greater than the TDMA and CCNc residence times. The measured $N_{CCN}$ at 0.25% $S$ during 2012 was very noisy and was excluded from the analysis.

*Comparison of $N_{CCN}$ calculated from different approaches*

$N_{CCN}$ estimated from different approaches relative to that estimated using the base model are presented in Figure 36 for June, 2011. Linear fits forced through the origin were used simply because of the apparent linear correlations with minimal offset in the figures. Table 4 summarizes the slope ($m = \frac{N_{CCN\ from\ alternate\ approach}}{N_{CCN\ from\ base\ model}}$) and goodness of fit ($r^2$) for each of the different approaches with respect to the base model. The slopes from best fit lines through each of the datasets are plotted against $S$ for 2011 in Figure 37. Values of $m$ above (below) 1 indicate that use of that model results in $N_{CCN}$ greater (less) than that from the base model for a given $S$.

**Table 4. Fit parameters of $N_{CCN}$ estimates for 2011 data.**

| Model | 0.25% $S$ | | 0.45% $S$ | | 0.65% $S$ | | 0.85% $S$ | | $\frac{m_{0.25\%\,S} - m_{0.85\%\,S}}{m_{0.25\%\,S}}$ |
|---|---|---|---|---|---|---|---|---|---|
| | $m$ | $r^2$ | $m$ | $r^2$ | $m$ | $r^2$ | $m$ | $r^2$ | |
| Pure salt | **1.94** | 0.83 | 1.58 | 0.86 | 1.42 | 0.86 | **1.34** | 0.87 | **0.31** |
| Internal, 80% AS | 1.77 | 0.85 | 1.49 | 0.88 | 1.36 | 0.88 | 1.28 | 0.88 | 0.28 |
| Internal, 50% AS | 1.32 | 0.86 | 1.23 | 0.90 | 1.17 | 0.91 | 1.13 | 0.90 | 0.14 |
| Internal, 20% AS | **0.70** | 0.83 | 0.80 | 0.87 | 0.84 | 0.86 | **0.85** | 0.84 | 0.21 |
| Internal, $SF(D)$ | **1.07** | **0.96** | 1.06 | 0.96 | 1.06 | 0.96 | **1.06** | **0.96** | **0.01** |
| Internal, $SF(\neq D)$ | 1.15 | 0.92 | 1.13 | 0.90 | 1.10 | 0.89 | 1.11 | 0.89 | 0.04 |
| Base model | 1 | 1 | 1 | 1 | 1 | 1 | 1 | 1 | 0 |
| External, $f_i(D)$ | 0.93 | 0.93 | 0.95 | 0.94 | 0.96 | 0.94 | 0.97 | 0.94 | 0.04 |
| External, $f_i(\neq D)$ | 0.99 | 0.91 | 0.99 | 0.90 | 0.98 | 0.88 | 0.97 | 0.87 | 0.02 |

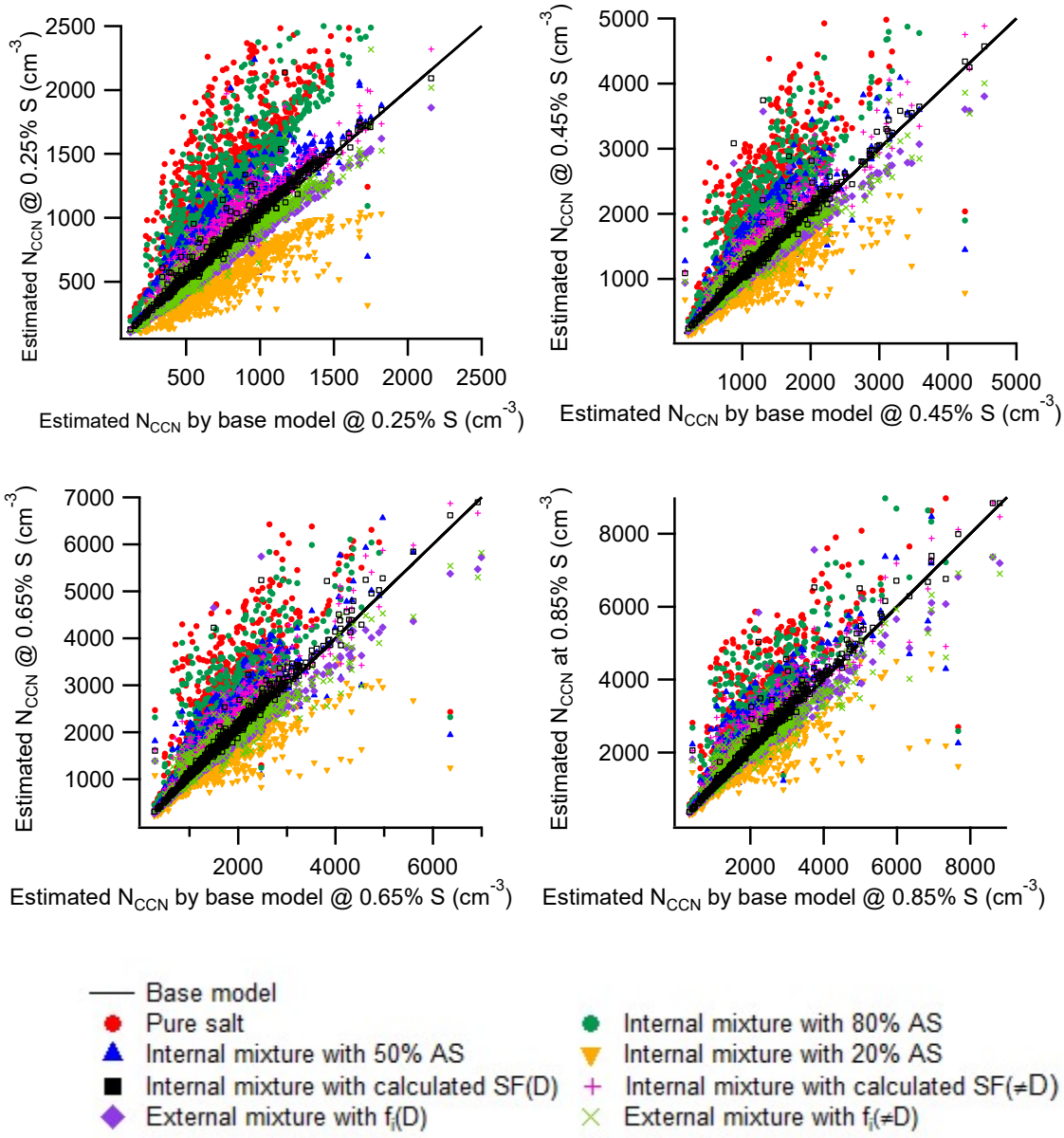


**Figure 36. $N_{CCN}$ at 0.25% (top, left), 0.45% (top, right), 0.65% (bottom, left) and 0.85% S (bottom, right) for June, 2011.**

In general, high $r^2$ with respect to the base model suggests that the approach may be employed with a simple multiplier (=$1/m$). The simplest approach taken assumed particles were internally mixed with a fixed percentage of AS. As expected, assumption of a high AS fraction (e.g., 100% AS) resulted in slopes well above 1, and of a low fraction (e.g., 20%) in slopes well below 1. These differences are most evident at lower $S$ (e.g., at 0.25% $S$, $m$ = 1.94 for pure AS and 0.7 for 20% AS). Linear interpolation between the percentages considered suggests that an assumption of 35% AS would result in a slope of about 1. However, exclusion of the hygroscopicity data in this approach would result in increased scatter, manifested by a lower $r^2$. Assumption of external and internal mixtures with composition determined from the $GF$ measurements resulted in best fit slopes below 1 and above 1, respectively, for all $S$.

The dependence of the best fit slopes on $S$ is shown in Figure 37 and quantified in the rightmost column in Table 4 as a fractional change over the full range in $S$ considered. The utility of any of the simplifying approaches is obviously greatest if applicable over a wide range in $S$. The best fit slopes from these approaches altogether take the shape of a funnel gradually approaching $m$=1 with increasing $S$. The fractional difference in $m$ between 0.25% and 0.85% $S$ is largest for the assumption of a pure AS aerosol and smallest for the assumption the aerosol is an internal mixture with $SF = SF(D)$.

It is not surprising that the two approaches that capture the hygroscopicity size dependence are most strongly correlated with the base model. Of the two, the internal mixture assumption resulted in the highest $r^2$ and the smallest variation in $m$ over the

full $S$ range. Thus, that somewhat simplified model could be used in place of that of the more computationally demanding base model with an $N_{CCN}$ correction factor of roughly 1/1.06. Of course, the balance between the importance of computational efficiency and predictive skill will vary considerably across applications.

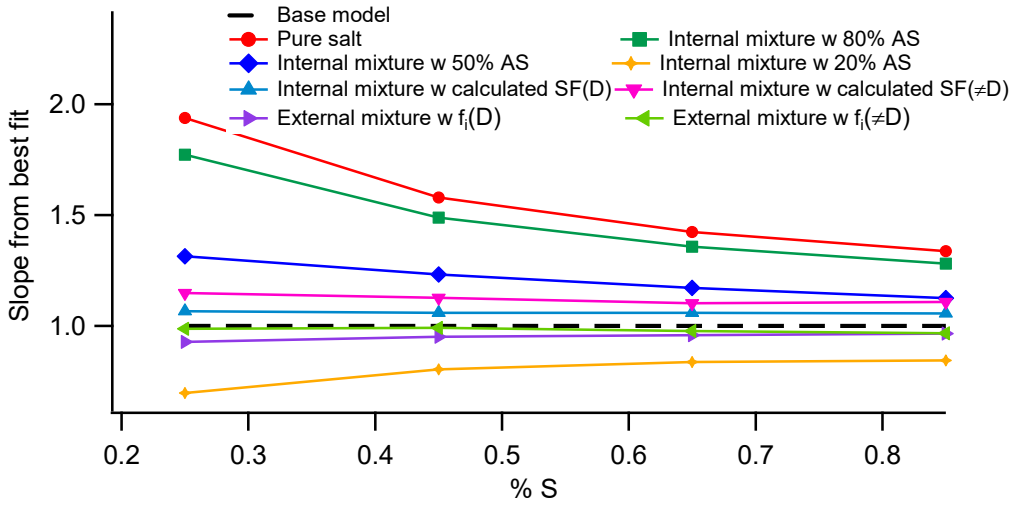


**Figure 37. $N_{CCN}$ from different models/ base model during 2011.**

## Summary

Size distributions and hygroscopic growth factor distributions measured from 2009 to 2012 at the SGP ARM site with a DMA/TDMA system were used to estimate CCN concentration over a range in supersaturation. Estimates used as a basis for comparison followed an approach similar to that described by *Gasparini et al.* [2006] in which matrices of $S_c(D, GF)$ and $N(D, GF)$ calculated from the measured distributions are used to calculate $N_{CCN}(S)$. Comparisons of those estimates with direct measurements

suggest that the base model approach can reasonably predict $N_{CCN}$ over a range of $S$ without detailed information about aerosol chemical composition.

Several simplified aerosol models were evaluated as alternates to the computationally expensive base model approach. These included approximating the aerosol as an internal mixture with fixed soluble fraction, as an internal mixture with size-dependent and size-independent calculated soluble fraction, and as an external mixture with size-dependent and size-independent calculated particle-type fractions. In general, high $r^2$ of the best fit line through the pairs of $N_{CCN}$ calculated from the base model and from one of the simplified models demonstrates its potential to serve as alternative for the base model when used with a multiplier, $1/m$. Of the simplified treatments considered, assuming the aerosol is an internal mixture with size-dependent soluble fraction resulted in the smallest fractional variation in $m$ and the highest $r^2$ over the selected $S$ range.

As aerosol properties vary with time and place, similar assessments of $N_{CCN}$ estimation approaches should be made using other comparable datasets.

# CHAPTER VII

# ESTIMATING OPTICAL PROPERTIES AND CLOUD CONDENSATION NUCLEI CONCENTRATION FROM COMMONLY MEASURED PARTICLLE PROPERTIES

## Introduction

The influence of atmospheric particles on climate can be broadly categorized into its direct and indirect effects. The direct effect describes attenuation of solar radiation by atmospheric particles through scattering and absorption. The indirect effect describes modification of cloud properties through activation of particles and formation of cloud droplets. Therefore, it is crucial to directly measure or adequately estimate them in order to assess particles' overall effect on the climate.

Optical properties (e.g., extinction, total scattering, absorption, hemispheric backscattering etc.) are functions of particle size, complex refractive index, and wavelength of the incident beam. Usually most of the extinction in the visible wavelength is caused by scattering. Absorption becomes significant during forest fire, or seasonal biomass burning. Hemispheric Backscattering, which is the fraction of the scattered intensity redirected towards the backward hemisphere, accounts for only 10-15% of the total, as scattering occurs mainly in the forward direction within the visible wavelength. Most optical properties can be determined from ground based instruments, or space borne remote sensors; e.g., Cimel sunphotometer (CSPHOT), Continuous Light Absorption Photometer (CLAP), nephelometer, micropulse lidar, Raman lidar etc. But those are not always convenient. As scattering of visible solar radiation primarily occurs

within the Mie scattering regime, it can also be explained by Mie theory / Mie-Debye-Lorenz theory through Maxwell equations [*Bohren and Huffman*, 1983]. However, Mie theory is analytically very complex. Particles within 0.3-0.7μm size range are most efficient scatterer of visible light spectrum (i.e., 0.4-0.7μm wavelength), which coincides with aerosol size range contributing to maximum mass/volume. Therefore, there is a potential link between volume and scattering, which has not been explored properly so far.

Cloud condensation nuclei concentration ($N_{CCN}$) varies spatially and temporally. It is usually higher in continental than the maritime air and in polluted than the clean air. Size and chemical composition of atmospheric particles affect their ability to act as CCN. $N_{CCN}$ is measured directly by CCN counter ($CCN_C$), where the air stream is adjusted to achieve pre-fixed supersaturations inside a flow column [*Ross et al.*, 2003; *Rose et al.*, 2008; *Liu et al.*, 2011]. Measuring $N_{CCN}$ is complex, costly, and limited. So it was attempted to estimate $N_{CCN}$ by various means.

*Twomey* [1959] proposed a power law formula assuming Junge Power Law distribution and uniform aerosol chemical composition. It was later modified by *Ji and Shaw* [1998] to better fit the CCN spectra. While *Mircea et al.* [2005] observed improved fitting using the modified Power law, *Deng et al.* [2013] found stronger correlation only at higher supersaturation. As chemical composition and size distribution information were not included in those equations, errors were high especially at extremely clean or polluted condition. *Jefferson et al.* [2010], used the original power law to estimate $N_{CCN}$, in which, parameters were calculated from optical properties, but

ended with a low goodness of fitting. Thus, application of power law formula was not suitable to estimate $N_{CCN}$.

Some researchers [*Pruppacher and Klett*, 1977; *Roberts et al.* 2002; *Rose et al.*, 2010; *Bougiatioti et al.*, 2009; *Deng et al.*, 2013] used Bulk activation ratio ($A_{Bulk,\ tot} = N_{CCN}/N_{CN}$) to determine $N_{CCN}$. There were disagreements in results (Table 5) as small particles comprise a major portion of total $N_{CN}$, but a small fraction of $N_{CCN}$. So, change in reference size range, chemical composition and %S caused great difference in the activation ratio. Consideration of bulk activation ratio for accumulation mode particles (>100nm) ($A_{bulk,acc} = N_{CCN}/N_{CN,\ D>100nm}$) improved the correlation (Table 6) [*Ross et al.*, 2003; *Breed et al.*, 2002; *Deng et al.*, 2013]. This ratio was further modified by using activated pure ammonium sulfate aerosol concentration as reference ($A_{bulk,\ AS} = N_{CCN}/N_{CCN,\ AS,}$), which improved the outcome [*Deng et al.*, 2013]. *Deng et al.*'s [2013] approach to use size distribution and sigmoidal activation ratio curve to calculate $D_{50}$, (i.e., diameter, where 50% of the particles are activated) and $N_{CCN}$ also showed good potential.

Several optical properties, such as, aerosol optical depth (AOD), extinction, and scattering were also used to estimate $N_{CCN}$ [*Ghan and Collins*, 2004; *Ghan et al.*, 2006; *Andrea et al.*, 2009; *Quaas et al.*, 2009; *Shinozuka et al.*, 2009; *Jefferson*, 2010; *Liu et al.*, 2011; *Wang et al.*, 2011; *Tao et al.*, 2012; *Grandey et al.*, 2013]. *Andreae et al.* [2009] and *Liu et al.* [2014] observed a power law relation between AOD and CCN which was improved after including humidity, hygroscopicity, and size distribution.

**Table 5. Summary of $N_{CCN}$ parameterization based on bulk activation ratio, $A_{bulk,tot}$**

| Study | Size | %S | $A_{bulk, tot}$ | Aerosol type/ site |
|---|---|---|---|---|
| | | | 0.2-0.6 | Maritime |
| *Pruppacher and Klett* [1977] | >10 nm | 1 | 0.004-0.25 | Continental |
| | | 0.15 | 0.07 | |
| | | 0.3 | 0.235 | |
| | | 0.6 | 0.458 | |
| | | 1 | 0.682 | |
| *Roberts et al.* [2002] | | 1.5 | 0.818 | Amazon basin |
| | | 0.068 | 0.06 | |
| | | 0.27 | 0.36 | |
| | | 0.47 | 0.53 | |
| | | 0.67 | 0.59 | |
| | | 0.87 | 0.71 | |
| *Rose et al.* [2010] | 3-900 nm | 1.27 | 0.85 | Guangzhou, China |
| | | 0.21 | 0.5 | |
| | | 0.38 | 0.7 | |
| *Bougiatioti et al.* [2009] | 10-460 nm | 0.5 | 0.8 | East Mediterranean |
| | | 0.061 | 0.06 | |
| | | 0.083 | 0.11 | |
| | | 0.2 | 0.37 | |
| | | 0.414 | 0.54 | |
| *Deng et al.* [2013] | 10 nm-10 μm | 0.812 | 0.65 | North China plain |

**Table 6. Summary of $N_{CCN}$ parameterization based on accumulation mode activation ratio, $A_{bulk,acc}$**

| Study | Size | %S | $A_{bulk,acc}$ | Site |
|---|---|---|---|---|
| | | 0.36 | 0.41-0.85 | Southern Africa, dry season |
| *Ross et al.*, [2003] | | 0.28 | 0.2-0.45 | Southern Africa, wet season |
| | | | <1 | within boundary layer |
| *Breed et al.*, [2002] | | | >1 | above boundary layer |
| | | 0.061 | <1 | |
| | | 0.083 | <1 | |
| | | 0.2 | ~1 | |
| | | 0.4 | >1 | |
| *Deng et al.*, [2013] | >100 nm | 0.8 | >1 | North China plain |

$N_{CCN}$ can also be determined for inorganic particles using *Köhler* theory [1936], with known physico-chemical properties (e.g., size, hygroscopicity) [*Gasparini et al.*, 2006; *Ervens et al.*, 2007; *Deng et al.*, 2013], which was later modified acknowledging the effect of solubility and surface tension-reducing properties of organics species on $S_c$ [*Raymond and Pandis*, 2002, 2003; *Bilde and Svenningsson*, 2004; *Hartz et al.*, 2006; *Svenningsson et al.*, 2006, *Petters and Kreidenweis,* 2007, *Moore et al.*, 2011] and the effect of mixing state.

Although optical properties and $N_{CCN}$ can be predicted / measured adequately, there are still scopes to parameterize them using commonly measured particle properties, such as, size distribution, GF etc., which is main focus of this study.

## Methodology

### *Parameterizing optical properties*

In atmosphere, the accumulation mode particles contribute most to the total aerosol volume and the optical properties within the visible wavelength range. So, attempt was made to establish relations between Mie theory derived optical properties (i.e., extinction coefficient ($b_{ext}$), scattering coefficient ($b_{scat}$), hemispheric backscattering coefficient ($b_{h.back}$) and backscattering coefficient ($b_{back}$)) calculated at 550 nm wavelength for an array of fixed RHs (i.e., 24, 59, 77, 86, 90, 92, 94, 95 and 95.7% ) and aerosol properties, such as, total particle volume concentration (V) between 200 nm and 500 nm, and the corresponding average GF at 90% RH. The array of RHs considered for

calculating optical properties were chosen so that difference in calculated values at two consecutive RHs remains roughly constant throughout. Each optical property was then fitted with a combination of V and GF at individual RH through trial and error to represent it as a bivariate function as ($f(V,GF) = m.V^aGF^b$). Finally RH was included in the expression as f(V, GF, RH) to predict each optical property reasonably well at any RH.

### *Parameterizing $N_{CCN}$*

CCN concentration was determined using modified Köhler Theory at 0.1, 0.2, 0.3, 0.4, 0.5, 0.6, 0.8, and 1% supersaturations as described in CHAPTER VI. As atmospheric supersaturations (S) are often less than 1%, it was set as the upper limit. Also, as larger hygroscopic aerosols are activated at lower S, the effort was made to correlate number concentration of large particles to Köhler theory derived $N_{CCN}$ at lower S and vice versa. So a total of 5 size groups (i.e., 0.05 - 0.5µm, 0.1 - 0.5 µm, 0.2-0.5µm, 0.3- 0.5µm, and 0.4-0.5µm) were considered to correlate $N_{CN}$ from each group to derived $N_{CCN}$ at a given S. Further, the slope of the dataset ($N_{CCN}$ / $N_{CN}$), or Activation Ratio (AR) at each S was divided into two groups using K-mean clustering method, in which the group with larger slope represents more hygroscopic particles and the group with smaller slope represents less hygroscopic particles. Finally, inclusion of trends in AR and % observation made it possible to establish a single equation determining $N_{CCN}$ at and above 0.3 % S.

## Result and discussion

### *Parameterizing optical property*

Optical properties calculated from Mie theory and fitted empirical equations are plotted in Figure 38 for selected RHs. The linear correlations between all optical properties (except $b_{back}$) and $V^aGF^b$ (where, a and b are equation parameters) are high. The correlations improved at higher RH, at which scattering occurs more towards forward direction from expanded aerosols. Coefficient a associated with the dry volume V does not change with change in RH. But change in coefficient b with RH has a clear pattern for all the optical properties. These correlations overall reflects the dependence of these optical properties on total particle volume at any given RH. As a next step, the RH itself is included in the equation (equation 29 - 32) as a variable.

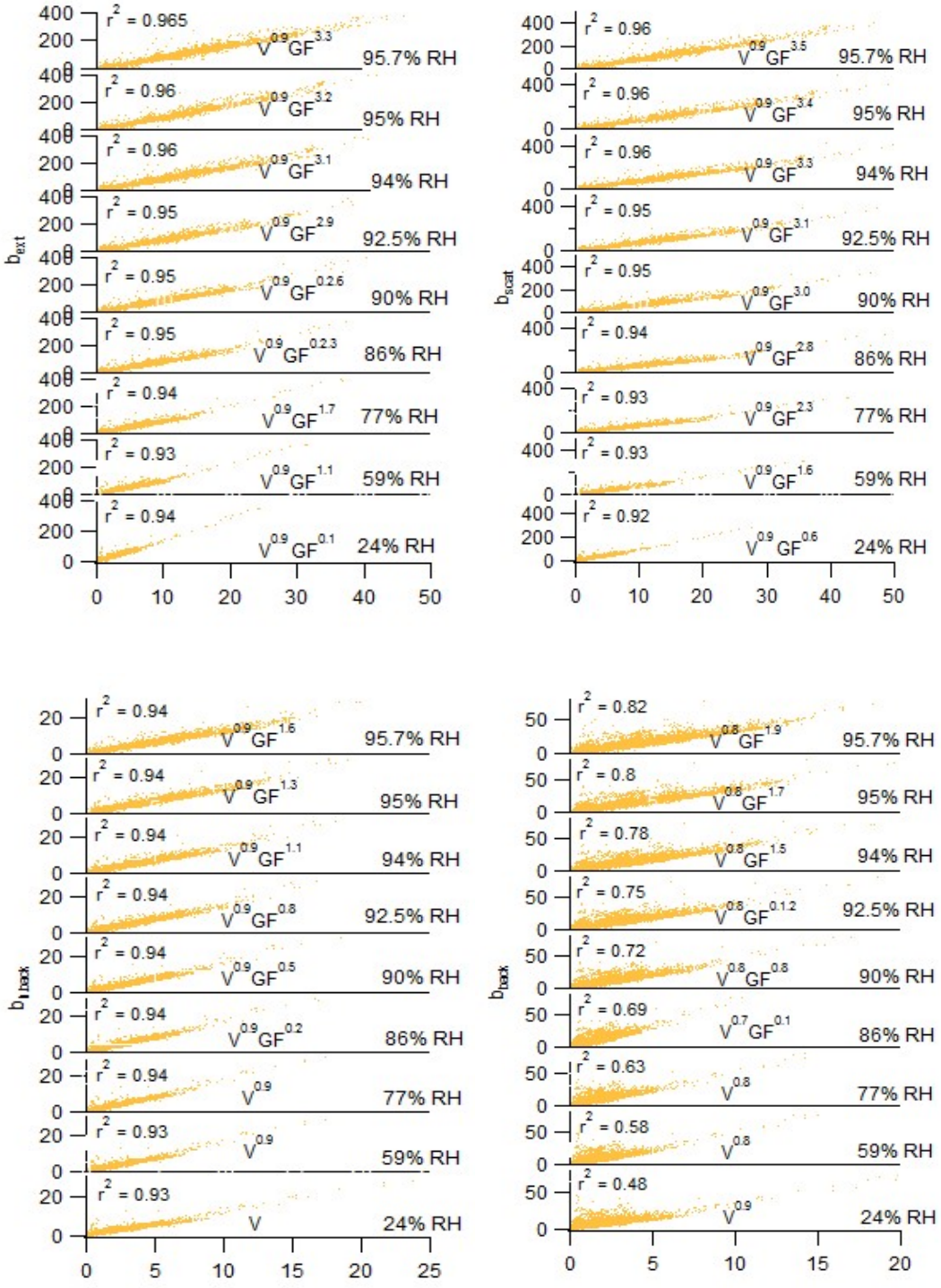


**Figure 38. $b_{ext}$ (top, left), $b_{scat}$ (top, right), $b_{h.back}$ (bottom, left) and $b_{back}$ (bottom, right) vs. $V^aGF^b$.**

In order to collapse all 9 empirical equations into one single equation as f(RH, V, GF), the variations in slope and parameter b with respect to RH were taken into account as parameter a mostly remained unchanged. The final expressions for $b_{ext}$, $b_{scat}$, $b_{h.back}$ and $b_{back}$ are shown in Equation 29 - 32 and plotted against Mie theory derived values in Figure 39.

$$b_{ext} = 54.41\{\left(\frac{RH}{100} - 0.56\right)^3 - 0.24\left(\frac{RH}{100} - 0.56\right) + 0.2\}V_{dry}^{0.9} GF_{90\%RH}^{3.54\left(\frac{RH}{100}\right)^{2.48}} \quad (29)$$

$$b_{scat} = 88.03\{\left(\frac{RH}{100} - 0.56\right)^3 - 0.16\left(\frac{RH}{100} - 0.56\right) + 0.095\}V_{dry}^{0.9} GF_{90\%RH}^{0.36\exp(2.38\frac{RH}{100})} \quad (30)$$

$$b_{h.back} = -13.26\{\left(\frac{RH}{100} - 0.55\right)^3 - 0.15\left(\frac{RH}{100} - 0.55\right) - 0.11\}V_{dry}^{0.9} GF_{90\%RH}^{4*10^{-10}\exp(23.14\frac{RH}{100})} \quad (31)$$

$$b_{back} = -45.18\{\left(\frac{RH}{100} - 0.52\right)^3 - 0.13\left(\frac{RH}{100} - 0.52\right) - 0.1\}V_{dry}^{0.8} GF_{90\%RH}^{3*10^{-12}\exp(28.643\frac{RH}{100})} \quad (32)$$

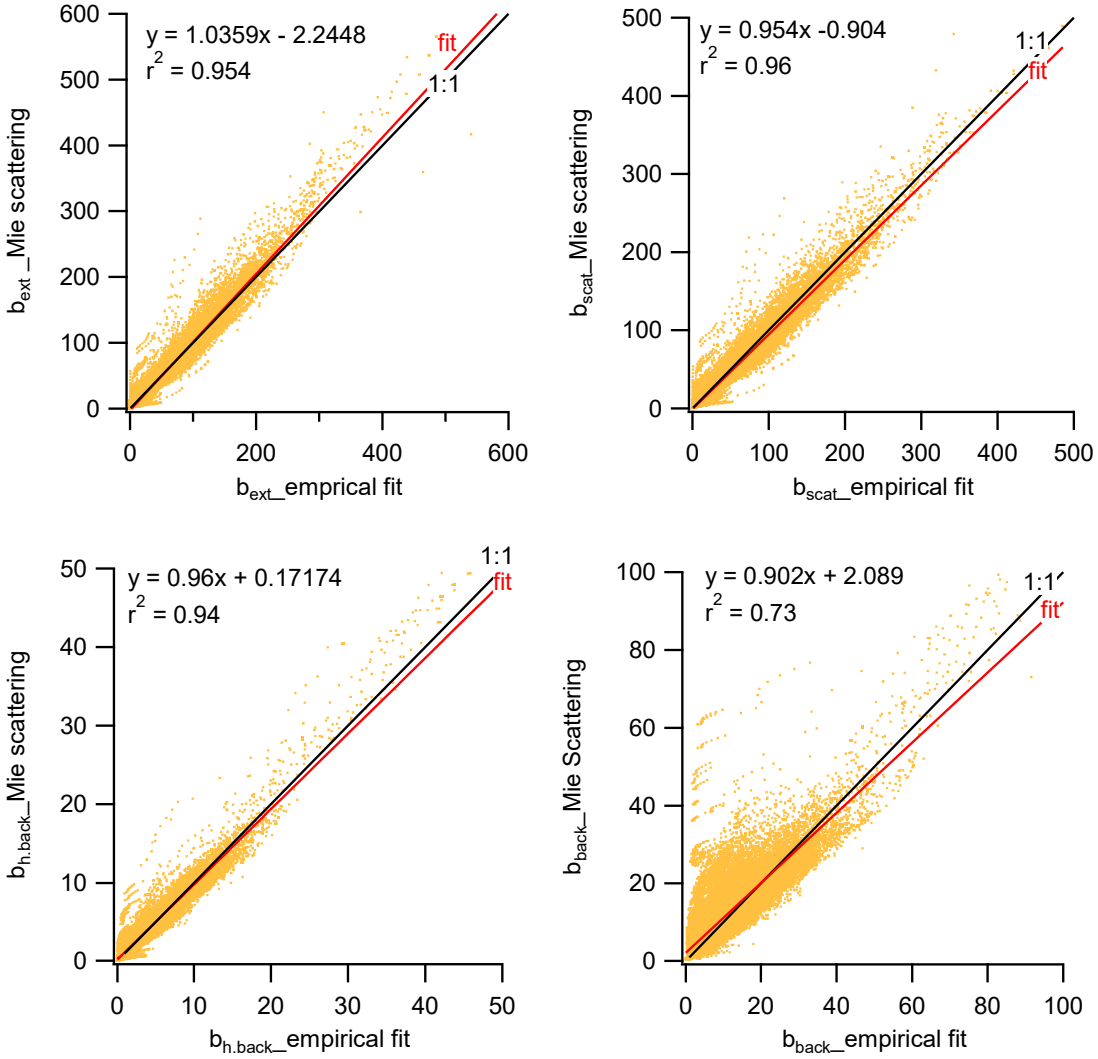


**Figure 39. Optical properties ($b_{ext}$ (top, left), $bs_{cat}$ (top, right), $b_{h.back}$ (bottom, left), and $b_{back}$ (bottom, right)) calculated from Mie scattering vs. empirically fitted f(V,GF,RH) in 2009.**

From Figure 39 it is evident that at 550 nm wavelength and within the RH range of 24 - 95.7 % RH, $b_{ext}$, $bs_{cat}$ and $b_{h.back}$ can be determined reasonably using these empirical equations.

### *Parameterization of $N_{CCN}$*

Activation ratio (AR) is defined as the ratio of activated particle concentration to total particle concentration ($N_{CCN}/N_{CN}$). AR depends on particle's size and chemical composition. The GF distribution of the aerosol suggests that within the size range of 0.05 -0.5 μm, smaller aerosols are usually less hygroscopic with higher organic content relative to larger aerosols with higher inorganic content. Although organic compounds can slightly decrease the surface tension, its hydrophobic nature lowers the water uptake enough to raise its overall critical supersaturation [*Kaku et al.*, 2006]. Also, larger particles are activated at relatively lower supersaturation due to Kelvin effect. So the dataset was divided into 2 groups: Group 1 with higher AR (i.e., hygroscopic particles) and Group 2 with lower AR (less-hygroscopic particles). The $N_{CCN}$ vs. $N_{CN}$ at different supersaturations and years are shown in Figure 40. The annual average of AR, $r^2$ and % observation is presented in Table 7 and Figure 41.

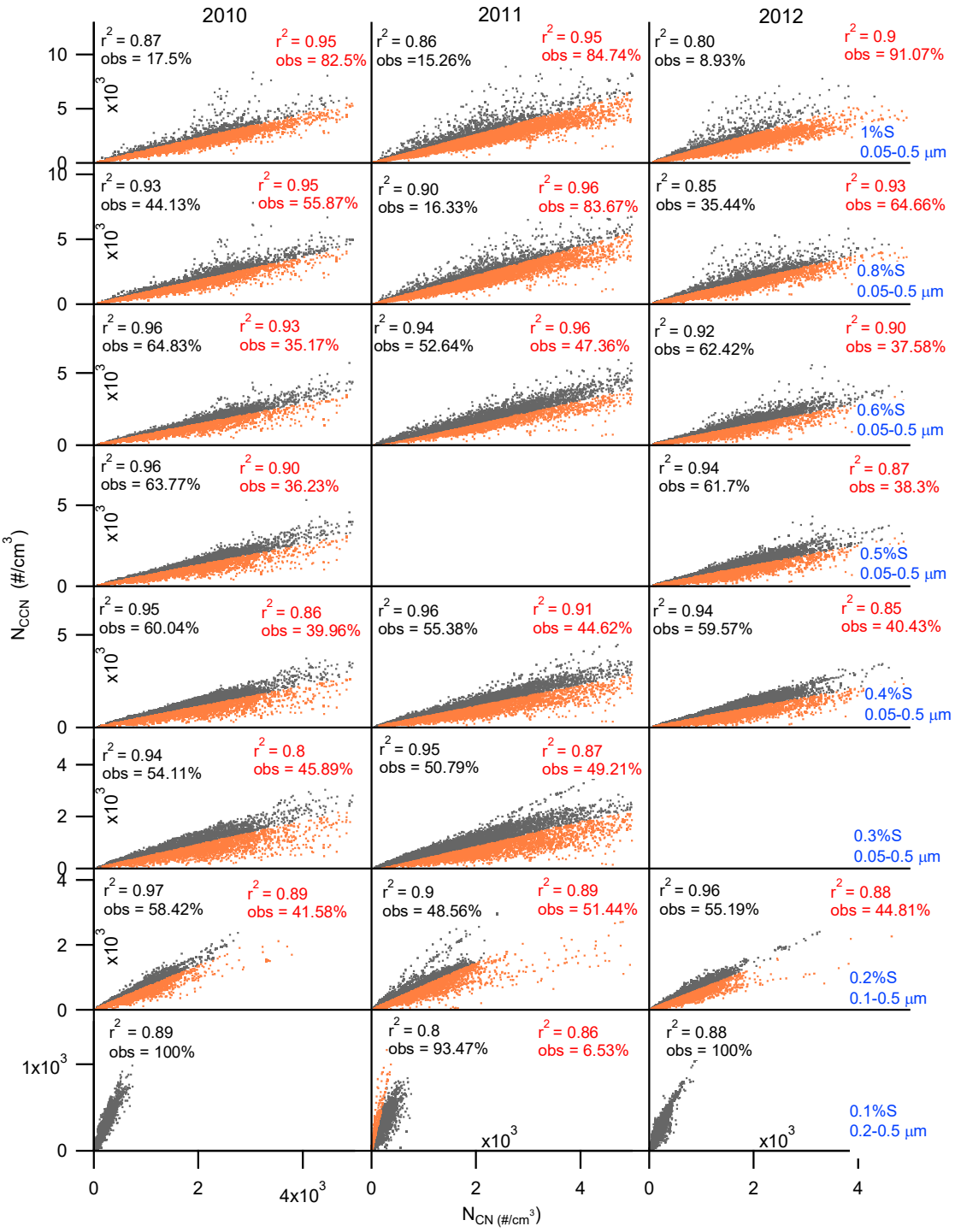


**Figure 40. $N_{CCN}$ at selected %S (blue) vs. $N_{CN}$ from selected size range (blue) in 2010 (left), 2011 (middle) and 2012 (right). Group 1 and 2 are shown in gray and orange respectively and their corresponding $r^2$ and % observations are shown in black and red.**

**Table 7. Averaged annual AR, $r^2$ and % observation**

| %S | Size range (μm) | Group 1 | | | Group 2 | | | Activation ratio |
|---|---|---|---|---|---|---|---|---|
| | | Activation ratio $N_{CCN}/N_{CN}$ | $r^2$ | % observation | Activation ratio $N_{CCN}/N_{CN}$ | $r^2$ | % observation | |
| 0.1 | **0.2-0.5** | 1.27 | 0.86 | 97.82 | 1.03 | 0.86 | 2.18 | **1.26** |
| 0.2 | 0.1-0.5 | 0.79 | 0.94 | 54.06 | 0.53 | 0.89 | 45.94 | 0.67 |
| **0.3** | **0.1-0.5** | 1.3 | 0.92 | 29.58 | 0.9 | 0.92 | 70.42 | **1.02** |
| 0.3 | 0.05-0.5 | 0.55 | 0.94 | 52.45 | 0.34 | 0.83 | 47.55 | 0.45 |
| 0.4 | 0.05-0.5 | 0.67 | 0.95 | 58.33 | 0.44 | 0.87 | 41.67 | 0.57 |
| 0.5 | 0.05-0.5 | 0.68 | 0.85 | 100 | | | | 0.68 |
| 0.5 | 0.05-0.5 | 0.77 | 0.95 | 62.73 | 0.53 | 0.89 | 37.27 | 0.68 |
| 0.6 | 0.05-0.5 | 0.87 | 0.94 | 59.96 | 0.63 | 0.93 | 40.04 | 0.77 |
| 0.8 | 0.05-0.5 | 1.13 | 0.89 | 31.93 | 0.83 | 0.94 | 68.07 | 0.93 |
| **1** | **0.05-0.5** | 1.53 | 0.84 | 13.9 | 0.98 | 0.93 | 86.1 | **1.06** |

On an average, all particles between 0.1 μm - 0.5 μm and 0.05 - 0.5 μm were activated at 0.3 % S and 1 % S respectively. At 0.1 % S, activated particle concentration was roughly 1.26 times higher than total $N_{CN}$ between 0.2 μm and 0.5 μm indicating activation of particles smaller than 0.2 μm. At other supersaturations, a fraction of total $N_{CN}$ within the selected range was activated. For example, only 45 % of the total $N_{CN}$ between 0.05 μm and 0.5 μm was activated at 0.3% S. The $N_{CN}$ fraction increased gradually with increasing supersaturation and reached ~ 100% at 1 % S.

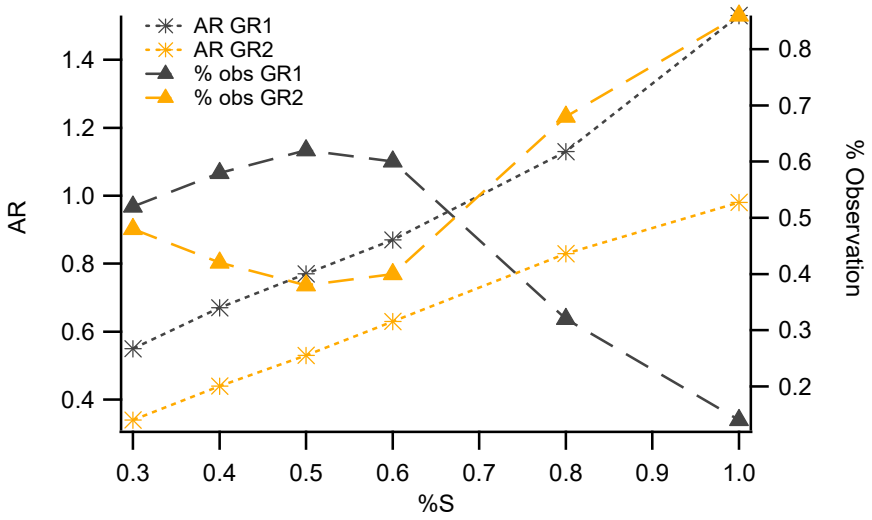


**Figure 41. Annual average of AR, and % observation vs. S above 0.3%S.**

It is evident from Figure 41 that for both groups AR consistently increased with S. From 0.3 – 0. 6 % S, GR 1 had higher number of observations than GR 2 which reversed at higher supersaturation. GR 2 usually contains less hygroscopic particles which are more common within the smaller size range. So, with activation of smaller particles at higher S, number of observation in less hygroscopicity group (GR 2) increased. Particles larger than 0.3 µm sometimes contain non-hygroscopic dust and/ carbonaceous organics, which explains reduced number of observation in GR 1 at lower S. Inclusion of trends in AR and % observation was useful to establish a single equation to parameterize $N_{CCN}$ at and above 0.3 % S (Equation 33).

$$N_{CCN}(S) = 0.815.S\{1.7 - (S - 0.46)^2\}N_{CN_{0.05-0.5\mu m}} \quad (33)$$

$N_{CCN}$ calculated for 2009 – 2012 from modified Köhler theory and Equation 33 is plotted in Figure 42. The high goodness of fitting ($r^2 = 0.87$) suggests the potential of the empirical equation to determine $N_{CCN}$ above 0.3 % S.

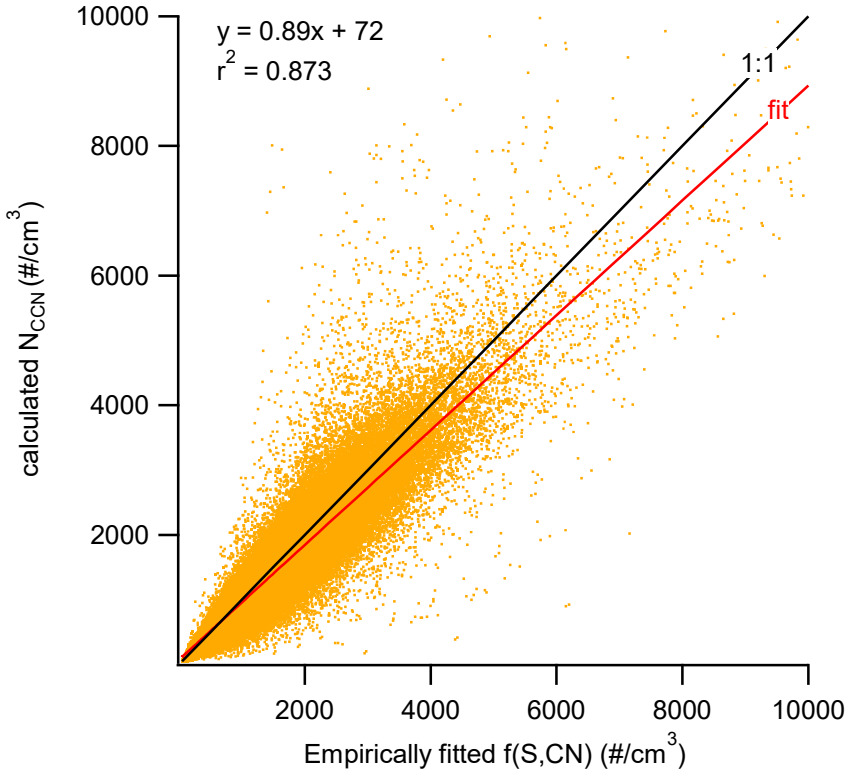


**Figure 42. $N_{CCN}$ calculated from modified Köhler theory vs. $N_{CCN}$ from parameterization equation.**

## Summary

Parameterization of the optical properties and $N_{CCN}$ would be very useful in order to avoid problems associated with direct measurements or complex calculation steps. In this study, several optical properties (i.e., extinction coefficient, scattering coefficient, hemispheric backscattering coefficient and backscattering coefficient) were

parameterized by establishing empirical relation between Mie theory derived values and particle properties from 2009. As larger particles are better scatterer and contribute most to the total volume, a combination of total aerosol volume and average GF between 0.2 - 0.5 μm (i.e., $mV^aGF^b$) was attempted to correlate with individual optical property. After appropriate fitting, all except backscattering was found to have high goodness of fitting. Finally, the trend in m, a and b was used to express the optical properties as functions of RH, V and GF. Here too, the result was very promising except for backscattering.

$N_{CCN}$ calculated from modified Köhler theory was parameterized using activation ratio (AR): the ratio of number concentration of activated particles to total particles. As aerosols between 0.05μm and 0.5 μm are relatively more hygroscopic, their number concentration was correlated to $N_{CCN}$ at lower S and vice versa. The dataset was further divided into 2 groups based on their AR. The trend in % observation and AR from 2009 – 2012 was used to finally express $N_{CCN}$ at and above 0.3 % S as a bivariate function of S, and total $N_{CN}$ between 0.05 μm and 0.5 μm. Overall, the derived empirical formula was able to reasonably predict $N_{CCN}$ at varying S.

# CHAPTER VIII

# CONCLUSIONS

The current work is based on particle size and size resolved hygroscopic growth distributions measured with an SMPS/TDMA system at the ARM SGP site. From measurements from 2009 and 2011 new particle formation (NPF) and subsequent growth events were detected frequently from March to October when solar irradiance and biogenic emission are expected to be higher. The newly formed particles grew mainly due to condensation of low volatility inorganic and/or organic species. The smaller particles within the measured size range grew at least to ~ 22 nm during the daytime through active photochemistry and high concentrations of gas phase organic compounds, while the subsequent growth beyond that size came during later hours of the day when photochemical aerosol production subsided. This explains the observed trend of higher growth rate in smaller particles relative to larger ones. Regardless of size, particles grew faster during the summer months when the intense solar radiation promotes faster photochemical reactions. The hygroscopic growth factor (GF), which describes the composition-dependent water uptake capacity of particles, usually displayed a diel variation with a higher value during daytime than at night suggesting more daytime condensation of hygroscopic (e.g., inorganics and oxygenated organics) species. The outcome from a two-component condensable gas model attributes the daytime growth to hygroscopic inorganic + less-hygroscopic organic species and nighttime growth

primarily to organic species condensation. The seasonal variation of derived organic precursor concentration expectedly showed higher values during the summer.

The hygroscopicity parameter, *k*, was calculated from measured GF data from 2009 to 2012 and averaged for 3 evaluated time-spans, morning, day, and night. It was highest during the daytime regardless of size and relatively higher at night than in the morning for particles smaller than 100 nm. It was also higher for particles < 100 nm during days and nights on which NPF events were observed. In general, the smaller and larger particles within the measured size range were more hygroscopic with higher inorganic content, but less so at intermediate sizes, resulting a minimum in *k* at 50 nm.

Further categorization of modes in the GF distributions into hygroscopic, less-hygroscopic, and nearly-hydrophobic groups showed that nearly-hydrophobic particle modes were common over the entire measured size range, while less hygroscopic and hygroscopic particle modes were more frequently detected at smaller and larger sizes, respectively. The mixing state of the aerosols was quantified using the GF distributions and size specific threshold SD separating internal and external mixing states. The results indicate more frequent formation of internal mixtures during daytime and the summer when conditions are favorable for photochemical oxidation, condensation, and aging.

In order to assess the impact of the atmospheric particles on the radiation budget, upscatter fraction (β) was determined from the ratio of Mie theory derived upscattering coefficient ($b_{ups}$) and scattering coefficient ($b_{scat}$) using data from 2009. As $b_{ups}$ and $b_{scat}$ are mainly influenced by particle size, both increased with increases in forward scattering accompanying higher altitude in the boundary layer and, consequently, higher

RH. Though particle size affects β to some extent as observed in its altitudinal profile, the position of the sun is the primary cause of its diurnal and seasonal variation, leading to maxima during the sunset daily and in the winter seasonally as a result of more symmetric distribution of scattering intensity. Parameterization of β was possible using the solar position and a measure of particle size. Other optical properties including extinction coefficient, scattering coefficient, and hemispheric backscatter coefficient were also parameterized successfully using aerosol volume concentration, GF, and RH.

Atmospheric particles also affect cloud properties through their control on cloud droplet concentration. The connection between aerosol characteristics and CCN concentration was investigated by employing various composition and mixing state based models. The comparison between estimated $N_{CCN}$ from a detailed model coupling measured size and GF distributions and the measured $N_{CCN}$ over a range of supersaturation (S) from 2009 to 2012 showed promising results. Among other simplified composition and mixing state based models, assuming the aerosol is an internal mixture with size-dependent soluble fraction resulted in the least difference between estimated $N_{CCN}$ from this model and the base model, and highest $r^2$ over the selected S range. Additionally, $N_{CCN}$ was parameterized adequately above 0.3% S based on a combination of supersaturation and the integrated particle concentration between 50 nm and 500 nm.

# REFERENCES

Abbatt, J., Broekhuizen, K., & Pradeepkumar, P. (2005). Cloud condensation nucleus activity of internally mixed ammonium sulfate/organic acid aerosol particles. *Atmospheric Environment, 39*(26), 4767-4778. doi:10.1016/j.atmosenv.2005.04.029

Andreae, M. O. (2009). Correlation between cloud condensation nuclei concentration and aerosol optical thickness in remote and polluted regions. *Atmospheric Chemistry and Physics, 9*(2), 543-556. doi:10.5194/acp-9-543-2009

Asa-Awuku, A., Moore, R. H., Nenes, A., Bahreini, R., Holloway, J. S., Brock, C. A., . .. Huey, L. G. (2011). Airborne cloud condensation nuclei measurements during the 2006 Texas Air Quality Study. *Journal of Geophysical Research, 116*(D11). doi:10.1029/2010jd014874

Bigg, E. (1986). Discrepancy between observation and prediction of concentrations of cloud condensation nuclei. *Atmospheric Research, 20*(1), 81-86. doi:10.1016/0169-8095(86)90010-4

Bilde, M., & Svenningsson, B. (2004). CCN activation of slightly soluble organics: the importance of small amounts of inorganic salt and particle phase. *Tellus B, 56*(2), 128-134. doi:10.1111/j.1600-0889.2004.00090.x

Bohren, C. F., & Huffman, D. R. (1983). *Absorption and Scattering of Light by Small Particles*. New York, John Wiley & Sons.

Bougiatioti, A., Fountoukis, C., Kalivitis, N., Pandis, S. N., Nenes, A., & Mihalopoulos, N. (2009). Cloud condensation nuclei measurements in the eastern Mediterranean marine boundary layer: CCN closure and droplet growth kinetics. *Atmospheric Chemistry and Physics Discussions, 9*(2), 10303-10336. doi:10.5194/acpd-9-10303-2009

Boulon, J., Sellegri, K., Venzac, H., Picard, D., Weingartner, E., Wehrle, G., . . . Laj, P. (2010). New particle formation and ultrafine charged aerosol climatology at a high

altitude site in the Alps (Jungfraujoch, 3580 m a.s.l., Switzerland). *Atmospheric Chemistry and Physics, 10*(19), 9333-9349. doi:10.5194/acp-10-9333-2010

Breed, D., Bruintjes, R., Jensen, T., Salazar, V., and Piketh, S. (2002), Aerosol and cloud droplet measurements in the United Arab Emirates, 11th Conference on Cloud Physics.

Broekhuizen, K., Chang, R. Y., Leaitch, W. R., Li, S., & Abbatt, J. P. (2005). Closure between measured and modeled cloud condensation nuclei (CCN) using size-resolved aerosol compositions in downtown Toronto. *Atmospheric Chemistry and Physics Discussions, 5*(4), 6263-6293. doi:10.5194/acpd-5-6263-2005

Cantrell, W., Shaw, G., Cass, G. R., Chowdhury, Z., Hughes, L. S., Prather, K. A., . . . Coffee, K. R. (2001). Closure between aerosol particles and cloud condensation nuclei at Kaashidhoo Climate Observatory. *Journal of Geophysical Research: Atmospheres, 106*(D22), 28711-28718. doi:10.1029/2000jd900781

Cerully, K. M., Raatikainen, T., Lance, S., Tkacik, D., Tiitta, P., Petäjä, T., . . . Nenes, A. (2011). Aerosol hygroscopicity and CCN activation kinetics in a boreal forest environment during the 2007 EUCAARI campaign. *Atmospheric Chemistry and Physics, 11*(23), 12369-12386. doi:10.5194/acp-11-12369-2011

Chan, M. N., Kreidenweis, S. M., & Chan, C. K. (2008). Measurements of the Hygroscopic and Deliquescence Properties of Organic Compounds of Different Solubilities in Water and Their Relationship with Cloud Condensation Nuclei Activities. *Environmental Science & Technology, 42*(10), 3602-3608. doi:10.1021/es7023252

Chang, R. Y., Slowik, J. G., Shantz, N. C., Vlasenko, A., Liggio, J., Sjostedt, S. J., . . . Abbatt, J. P. (2010). The hygroscopicity parameter (κ) of ambient organic aerosol at a field site subject to biogenic and anthropogenic influences: relationship to degree of aerosol oxidation. *Atmospheric Chemistry and Physics, 10*(11), 5047-5064. doi:10.5194/acp-10-5047-2010

Chang, R., Liu, P., Leaitch, W., & Abbatt, J. (2007). Comparison between measured and predicted CCN concentrations at Egbert, Ontario: Focus on the organic aerosol fraction at a semi-rural site. *Atmospheric Environment, 41*(37), 8172-8182. doi:10.1016/j.atmosenv.2007.06.039

Charlson, R. J., Langner, J., Rodhe, H., Leovy, C. B., & Warren, S. G. (1991). Perturbation of the northern hemisphere radiative balance by backscattering from anthropogenic sulfate aerosols*. *Tellus A, 43*(4), 152-163. doi:10.1034/j.1600-0870.1991.00013.x

Choi, M. Y., & Chan, C. K. (2002). The Effects of Organic Species on the Hygroscopic Behaviors of Inorganic Aerosols. *Environmental Science & Technology, 36*(11), 2422-2428. doi:10.1021/es0113293

Cohn, S. A., & Angevine, W. M. (2000). Boundary Layer Height and Entrainment Zone Thickness Measured by Lidars and Wind-Profiling Radars. *Journal of Applied Meteorology, 39*(8), 1233-1247. doi:10.1175/1520-0450(2000)039<1233:blhaez>2.0.co;2

Collins, D. (2010). Tandem Differential Mobility Analyzer/Aerodynamic Particle Sizer (APS) Handbook. doi:10.2172/982072

Collins, D. R., Flagan, R. C., & Seinfeld, J. H. (2002). Improved Inversion of Scanning DMA Data. *Aerosol Science and Technology, 36*(1), 1-9. doi:10.1080/027868202753339032

Conant, W. C., Vanreken, T. M., Rissman, T. A., Varutbangkul, V., Jonsson, H. H., Nenes, A., . . . Seinfeld, J. H. (2004). Aerosol-cloud drop concentration closure in warm cumulus. *Journal of Geophysical Research: Atmospheres, 109*(D13). doi:10.1029/2003jd004324

Cruz, C. N., & Pandis, S. N. (2000). Deliquescence and Hygroscopic Growth of Mixed Inorganic−Organic Atmospheric Aerosol. *Environmental Science & Technology, 34*(20), 4313-4319. doi:10.1021/es9907109

Cubison, M. J., Ervens, B., Feingold, G., Docherty, K. S., Ulbrich, I. M., Shields, L., . . . Jimenez, J. L. (2008). The influence of chemical composition and mixing state of Los Angeles urban aerosol on CCN number and cloud properties. *Atmospheric Chemistry and Physics, 8*(18), 5649-5667. doi:10.5194/acp-8-5649-2008

Davis, K. J., Gamage, N., Hagelberg, C. R., Kiemle, C., Lenschow, D. H., & Sullivan, P. P. (2000). An Objective Method for Deriving Atmospheric Structure from Airborne Lidar Observations. *Journal of Atmospheric and Oceanic Technology, 17*(11), 1455-1468. doi:10.1175/1520-0426(2000)017<1455:aomfda>2.0.co;2

Deng, Z. Z., Zhao, C. S., Ma, N., Ran, L., Zhou, G. Q., Lu, D. R., & Zhou, X. J. (2013). An examination of parameterizations for the CCN number concentration based on in situ measurements of aerosol activation properties in the North China Plain. *Atmospheric Chemistry and Physics, 13*(13), 6227-6237. doi:10.5194/acp-13-6227-2013

Dick, W. D., Saxena, P., & Mcmurry, P. H. (2000). Estimation of water uptake by organic compounds in submicron aerosols measured during the Southeastern Aerosol and Visibility Study. *Journal of Geophysical Research: Atmospheres, 105*(D1), 1471-1479. doi:10.1029/1999jd901001

Duplissy, J., Decarlo, P. F., Dommen, J., Alfarra, M. R., Metzger, A., Barmpadimos, I., . . . Baltensperger, U. (2011). Relating hygroscopicity and composition of organic aerosol particulate matter. *Atmospheric Chemistry and Physics, 11*(3), 1155-1165. doi:10.5194/acp-11-1155-2011

Duplissy, J., Gysel, M., Alfarra, M. R., Dommen, J., Metzger, A., Prevot, A. S., . . . Baltensperger, U. (2008). Cloud forming potential of secondary organic aerosol under

near atmospheric conditions. *Geophysical Research Letters, 35*(3). doi:10.1029/2007gl031075

Dusek, U., Frank, G. P., Hildebrandt, L., Curtius, J., Schneider, J., Walter, S., . . . Andreae, M. O. (2006). Size Matters More Than Chemistry for Cloud-Nucleating Ability of Aerosol Particles. *Science, 312*(5778), 1375-1378. doi:10.1126/science.1125261

Ehn, M., Petäjä, T., Aufmhoff, H., Aalto, P., Hämeri, K., Arnold, F., . . . Kulmala, M. (2006). Hygroscopic properties of ultrafine aerosol particles in the boreal forest: diurnal variation, solubility and the influence of sulfuric acid. *Atmospheric Chemistry and Physics Discussions, 6*(5), 9937-9965. doi:10.5194/acpd-6-9937-2006

Engelhart, G. J., Asa-Awuku, A., Nenes, A., & Pandis, S. N. (2008). CCN activity and droplet growth kinetics of fresh and aged monoterpene secondary organic aerosol. *Atmospheric Chemistry and Physics, 8*(14), 3937-3949. doi:10.5194/acp-8-3937-2008

Ervens, B., Cubison, M. J., Andrews, E., Feingold, G., Ogren, J. A., Jimenez, J. L., . . . Allan, J. D. (2010). CCN predictions using simplified assumptions of organic aerosol composition and mixing state: a synthesis from six different locations. *Atmospheric Chemistry and Physics, 10*(10), 4795-4807. doi:10.5194/acp-10-4795-2010

Ervens, B., Cubison, M., Andrews, E., Feingold, G., Ogren, J. A., Jimenez, J. L., . . . Nenes, A. (2007). Prediction of cloud condensation nucleus number concentration using measurements of aerosol size distributions and composition and light scattering enhancement due to humidity. *Journal of Geophysical Research, 112*(D10). doi:10.1029/2006jd007426

Facchini, M. C., Mircea, M., Fuzzi, S., & Charlson, R. J. (1999). Cloud albedo enhancement by surface-active organic solutes in growing droplets. *Nature, 401*(6750), 257-259. doi:10.1038/45758

Fast, J., Zhang, Q., Tilp, A., Shippert, T., Parworth, C., & Mei, F. (2013). Organic Aerosol Component (OACOMP) Value-Added Product. doi:10.2172/1226569

Fiedler, V., Maso, M. D., Boy, M., Aufmhoff, H., Hoffmann, J., Schuck, T., . . . Kulmala, M. (2005). The contribution of sulphuric acid to atmospheric particle formation and growth: a comparison between boundary layers in Northern and Central Europe. *Atmospheric Chemistry and Physics, 5*(7), 1773-1785. doi:10.5194/acp-5-1773-2005

Flamant, C., Pelon, J., Flamant, P. H., Durand, P.(1997). Lidar determination of the entrainment zone thickness at the top of the unstable marine atmospheric boundary layer, Bound. Layer Meteor. 83, 247–284.

Flatau, P. J. (1997). Improvements in the discrete-dipole approximation method of computing scattering and absorption. *Optics Letters, 22*(16), 1205. doi:10.1364/ol.22.001205

Furutani, H., Dallosto, M., Roberts, G., & Prather, K. (2008). Assessment of the relative importance of atmospheric aging on CCN activity derived from field observations. *Atmospheric Environment, 42*(13), 3130-3142. doi:10.1016/j.atmosenv.2007.09.024

Gasparini, R., Collins, D. R., Andrews, E., Sheridan, P. J., Ogren, J. A., & Hudson, J. G. (2006). Coupling aerosol size distributions and size-resolved hygroscopicity to predict humidity-dependent optical properties and cloud condensation nuclei spectra. *Journal of Geophysical Research, 111*(D5). doi:10.1029/2005jd006092

Gasparini, R., Li, R., Collins, D. R., Ferrare, R. A., & Brackett, V. G. (2006). Application of aerosol hygroscopicity measured at the Atmospheric Radiation Measurement Programs Southern Great Plains site to examine composition and evolution. *Journal of Geophysical Research, 111*(D5). doi:10.1029/2004jd005448

Gerber, H. E., Hoppel, W. A., & Wojciechowski, T. A. (1977). Experimental Verification of the Theoretical Relationship between Size and Critical Supersaturation of Salt Nuclei. *Journal of the Atmospheric Sciences, 34*(11), 1836-1841. doi:10.1175/1520-0469(1977)034<1836:evottr>2.0.co;2

Ghan, S. J., & Collins, D. R. (2004). Use of In Situ Data to Test a Raman Lidar–Based Cloud Condensation Nuclei Remote Sensing Method. *Journal of Atmospheric and Oceanic Technology, 21*(2), 387-394. doi:10.1175/1520-0426(2004)021<0387:uoisdt>2.0.co;2

Ghan, S. J., Rissman, T. A., Elleman, R., Ferrare, R. A., Turner, D., Flynn, C., . . . Seinfeld, J. H. (2006). Use of in situ cloud condensation nuclei, extinction, and aerosol size distribution measurements to test a method for retrieving cloud condensation nuclei profiles from surface measurements. *Journal of Geophysical Research, 111*(D5). doi:10.1029/2004jd005752

Grandey, B. S., Stier, P., & Wagner, T. M. (2013). Investigating relationships between aerosol optical depth and cloud fraction using satellite, aerosol reanalysis and general circulation model data. *Atmospheric Chemistry and Physics, 13*(6), 3177-3184. doi:10.5194/acp-13-3177-2013

Gunthe, S. S., King, S. M., Rose, D., Chen, Q., Roldin, P., Farmer, D. K., . . . Pöschl, U. (2009). Cloud condensation nuclei in pristine tropical rainforest air of Amazonia: size-resolved measurements and modeling of atmospheric aerosol composition and CCN activity. *Atmospheric Chemistry and Physics, 9*(19), 7551-7575. doi:10.5194/acp-9-7551-2009

Gysel, M., Crosier, J., Topping, D. O., Whitehead, J. D., Bower, K. N., Cubison, M. J., . . . Coe, H. (2007). Closure study between chemical composition and hygroscopic growth of aerosol particles during TORCH2. *Atmospheric Chemistry and Physics, 7*(24), 6131-6144. doi:10.5194/acp-7-6131-2007

Gysel, M., Mcfiggans, G., & Coe, H. (2009). Inversion of tandem differential mobility analyser (TDMA) measurements. *Journal of Aerosol Science, 40*(2), 134-151. doi:10.1016/j.jaerosci.2008.07.013

Hallquist, M., Wenger, J. C., Baltensperger, U., Rudich, Y., Simpson, D., Claeys, M., . . . Wildt, J. (2009). The formation, properties and impact of secondary organic aerosol: current and emerging issues. *Atmospheric Chemistry and Physics Discussions, 9*(1), 3555-3762. doi:10.5194/acpd-9-3555-2009

Hartz, K. E., Tischuk, J. E., Chan, M. N., Chan, C. K., Donahue, N. M., & Pandis, S. N. (2006). Cloud condensation nuclei activation of limited solubility organic aerosol. *Atmospheric Environment, 40*(4), 605-617. doi:10.1016/j.atmosenv.2005.09.076

Hayden, K., Anlauf, K., Hoff, R., Strapp, J., Bottenheim, J., Wiebe, H., . . . Mckendry, I. (1997). The vertical chemical and meteorological structure of the boundary layer in the Lower Fraser Valley during Pacific 93. *Atmospheric Environment, 31*(14), 2089-2105. doi:10.1016/s1352-2310(96)00300-7

Haywood, J. M., & Shine, K. P. (1995). The effect of anthropogenic sulfate and soot aerosol on the clear sky planetary radiation budget. *Geophysical Research Letters, 22*(5), 603-606. doi:10.1029/95gl00075

Hersey, S. P., Sorooshian, A., Murphy, S. M., Flagan, R. C., & Seinfeld, J. H. (2009). Aerosol hygroscopicity in the marine atmosphere: a closure study using high-time-resolution, multiple-RH DASH-SP and size-resolved C-ToF-AMS data. *Atmospheric Chemistry and Physics, 9*(7), 2543-2554. doi:10.5194/acp-9-2543-2009

Hodshire, A. L., Lawler, M. J., Zhao, J., Ortega, J., Jen, C., Yli-Juuti, T., . . . Pierce, J. R. (2016). Multiple new-particle growth pathways observed at the US DOE Southern Great Plains field site. *Atmospheric Chemistry and Physics, 16*(14), 9321-9348. doi:10.5194/acp-16-9321-2016

Holmgren, H., Sellegri, K., Hervo, M., Rose, C., Freney, E., Villani, P., & Laj, P. (2014). Hygroscopic properties and mixing state of aerosol measured at the high altitude site Puy de Dôme (1465 m a.s.l.), France. *Atmospheric Chemistry and Physics Discussions, 14*(5), 6759-6802. doi:10.5194/acpd-14-6759-2014

Im, J., Saxena, V. K., & Wenny, B. N. (2001). An assessment of hygroscopic growth factors for aerosols in the surface boundary layer for computing direct radiative forcing. *Journal of Geophysical Research: Atmospheres, 106*(D17), 20213-20224. doi:10.1029/2000jd000152

Jefferson, A. (2010). Empirical estimates of CCN from aerosol optical properties at four remote sites. *Atmospheric Chemistry and Physics, 10*(14), 6855-6861. doi:10.5194/acp-10-6855-2010

Ji, Q., & Shaw, G. E. (1998). On supersaturation spectrum and size distributions of cloud condensation nuclei. *Geophysical Research Letters, 25*(11), 1903-1906. doi:10.1029/98gl01404

Jing, B., Tong, S., Liu, Q., Li, K., Wang, W., Zhang, Y., & Ge, M. (2016). Hygroscopic behavior of multicomponent organic aerosols and their internal mixtures with ammonium sulfate. *Atmospheric Chemistry and Physics, 16*(6), 4101-4118. doi:10.5194/acp-16-4101-2016

Jurányi, Z., Gysel, M., Duplissy, J., Weingartner, E., Tritscher, T., Dommen, J., . . . Baltensperger, U. (2009). Influence of gas-to-particle partitioning on the hygroscopic and droplet activation behaviour of α-pinene secondary organic aerosol. *Physical Chemistry Chemical Physics, 11*(36), 8091. doi:10.1039/b904162a

Kaku, K. C., Hegg, D. A., Covert, D. S., Santarpia, J. L., Jonsson, H., Buzorius, G., & Collins, D. R. (2006). Organics in the Northeastern Pacific and their impacts on aerosol hygroscopicity in the subsaturated and supersaturated regimes. *Atmospheric Chemistry and Physics, 6*(12), 4101-4115. doi:10.5194/acp-6-4101-2006

Kammermann, L., Gysel, M., Weingartner, E., Herich, H., Cziczo, D. J., Holst, T., . . . Baltensperger, U. (2010). Subarctic atmospheric aerosol composition: 3. Measured and modeled properties of cloud condensation nuclei. *Journal of Geophysical Research, 115*(D4). doi:10.1029/2009jd012447

King, S. M., Rosenoern, T., Shilling, J. E., Chen, Q., & Martin, S. T. (2007). Cloud Condensation Nucleus Activity of Secondary Organic Aerosol Particles Mixed with Sulfate. *Nucleation and Atmospheric Aerosols,* 1200-1204. doi:10.1007/978-1-4020-6475-3_238

King, S. M., Rosenoern, T., Shilling, J. E., Chen, Q., & Martin, S. T. (2009). Increased cloud activation potential of secondary organic aerosol for atmospheric mass loadings. *Atmospheric Chemistry and Physics, 9*(9), 2959-2971. doi:10.5194/acp-9-2959-2009

King, S. M., Rosenoern, T., Shilling, J. E., Chen, Q., Wang, Z., Biskos, G., . . . Martin, S. T. (2010). Cloud droplet activation of mixed organic-sulfate particles produced by the photooxidation of isoprene. *Atmospheric Chemistry and Physics Discussions, 10*(1), 213-244. doi:10.5194/acpd-10-213-2010

Köhler, H. (1936). The nucleus in and the growth of hygroscopic droplets. *Trans. Faraday Soc., 32*(0), 1152-1161. doi:10.1039/tf9363201152

Kuang, C., Mcmurry, P. H., & Mccormick, A. V. (2007). Dependence of Nucleation Rates on Sulfuric Acid Vapor Concentration in Diverse Atmospheric Locations. *Nucleation and Atmospheric Aerosols,* 57-61. doi:10.1007/978-1-4020-6475-3_11

Kumar, P. P., Broekhuizen, K., & Abbatt, J. P. (2003). Organic acids as cloud condensation nuclei: Laboratory studies of highly soluble and insoluble species. *Atmospheric Chemistry and Physics Discussions, 3*(1), 949-982. doi:10.5194/acpd-3-949-2003

Kuwata, M., Kondo, Y., Miyazaki, Y., Komazaki, Y., Kim, J. H., Yum, S. S., . . . Matsueda, H. (2008). Cloud condensation nuclei activity at Jeju Island, Korea in spring 2005. *Atmospheric Chemistry and Physics, 8*(11), 2933-2948. doi:10.5194/acp-8-2933-2008

Lance, S., Nenes, A., Mazzoleni, C., Dubey, M. K., Gates, H., Varutbangkul, V., . . . Jonsson, H. H. (2009). Cloud condensation nuclei activity, closure, and droplet growth kinetics of Houston aerosol during the Gulf of Mexico Atmospheric Composition and Climate Study (GoMACCS). *Journal of Geophysical Research, 114*. doi:10.1029/2008jd011699

Lance, S., Raatikainen, T., Onasch, T., Worsnop, D. R., Yu, X., Alexander, M. L., . . . Nenes, A. (2012). Aerosol mixing-state, hygroscopic growth and cloud activation efficiency during MIRAGE 2006. *Atmospheric Chemistry and Physics Discussions, 12*(6), 15709-15742. doi:10.5194/acpd-12-15709-2012

Levin, E. J., Prenni, A. J., Palm, B. B., Day, D. A., Campuzano-Jost, P., Winkler, P. M., . . . Smith, J. N. (2014). Size-resolved aerosol composition and its link to hygroscopicity at a forested site in Colorado. *Atmospheric Chemistry and Physics, 14*(5), 2657-2667. doi:10.5194/acp-14-2657-2014

Liu, J., & Li, Z. (2014). Estimation of cloud condensation nuclei concentration from aerosol optical quantities: influential factors and uncertainties. *Atmospheric Chemistry and Physics, 14*(1), 471-483. doi:10.5194/acp-14-471-2014

Liu, J., Zheng, Y., Li, Z., & Cribb, M. (2011). Analysis of cloud condensation nuclei properties at a polluted site in southeastern China during the AMF-China Campaign. *Journal of Geophysical Research, 116*. doi:10.1029/2011jd016395

Liu, P. F., Zhao, C. S., Göbel, T., Hallbauer, E., Nowak, A., Ran, L., . . . Wiedensohler, A. (2011). Hygroscopic properties of aerosol particles at high relative humidity and their

diurnal variations in the North China Plain. *Atmospheric Chemistry and Physics Discussions, 11*(1), 2991-3040. doi:10.5194/acpd-11-2991-2011

Liu, P. S., Leaitch, W. R., Banic, C. M., Li, S., Ngo, D., & Megaw, W. J. (1996). Aerosol observations at Chebogue Point during the 1993 North Atlantic Regional Experiment: Relationships among cloud condensation nuclei, size distribution, and chemistry. *Journal of Geophysical Research: Atmospheres, 101*(D22), 28971-28990. doi:10.1029/96jd00445

Low, R. D. (1969). A Generalized Equation for the Solution Effect in Droplet Growth. *Journal of the Atmospheric Sciences, 26*(3), 608-611. doi:10.1175/1520-0469(1969)026<0608:agefts>2.0.co;2

Lowe, P. R., Ficke, J. M. (1974). The computation of saturation vapor pressure, Environmental Prediction Research Facility, Naval Postgraduate School, Monterey, CA, Technical Paper 4-74.

Magi, B. I., Hobbs, P. V., Schmid, B., & Redemann, J. (2003). Vertical profiles of light scattering, light absorption, and single scattering albedo during the dry, biomass burning season in southern Africa and comparisons of in situ and remote sensing measurements of aerosol optical depths. *Journal of Geophysical Research: Atmospheres, 108*(D13). doi:10.1029/2002jd002361

Manninen, H. E., Nieminen, T., Asmi, E., Gagné, S., Häkkinen, S., Lehtipalo, K., . . . Kulmala, M. (2010). EUCAARI ion spectrometer measurements at 12 European sites – analysis of new particle formation events. *Atmospheric Chemistry and Physics, 10*(16), 7907-7927. doi:10.5194/acp-10-7907-2010

Maso, M. D., Kulmala, M., Riipinen, I., Wagner, R., Hussein, T., Aalto, P. P., and Lehtinen, K. E. J.(2005). Formation and growth of fresh atmospheric aerosols: eight years of aerosol size distribution data from SMEAR II, Hyytiälä, Finland, Boreal Environment Research 10: 323–336.

McDonald, J. E. (1953). Erroneous cloud-physics application of Raoult's law, Journal of meteorology, 10, 68-70.

Mcfiggans, G., Alfarra, M. R., Allan, J., Bower, K., Coe, H., Cubison, M., . . . Fuzzi, S. (2005). Simplification of the representation of the organic component of atmospheric particulates. *Faraday Discussions, 130*, 341. doi:10.1039/b419435g

Mcmurry, P. H., & Stolzenburg, M. R. (1989). On the sensitivity of particle size to relative humidity for Los Angeles aerosols. *Atmospheric Environment (1967), 23*(2), 497-507. doi:10.1016/0004-6981(89)90593-3

Medina, J., Nenes, A., Sotiropoulou, R. P., Cottrell, L. D., Ziemba, L. D., Beckman, P. J., & Griffin, R. J. (2007). Cloud condensation nuclei closure during the International Consortium for Atmospheric Research on Transport and Transformation 2004 campaign: Effects of size-resolved composition. *Journal of Geophysical Research, 112*(D10). doi:10.1029/2006jd007588

Meier, J., Wehner, B., Massling, A., Birmili, W., Nowak, A., Gnauk, T., . . . Wiedensohler, A. (2009). Hygroscopic growth of urban aerosol particles in Beijing (China) during wintertime: a comparison of three experimental methods. *Atmospheric Chemistry and Physics Discussions, 9*(2), 6889-6927. doi:10.5194/acpd-9-6889-2009

Menut, L., Flamant, C., Pelon, J., & Flamant, P. H. (1999). Urban boundary-layer height determination from lidar measurements over the Paris area. *Applied Optics, 38*(6), 945. doi:10.1364/ao.38.000945

Meyer, N. K., Duplissy, J., Gysel, M., Metzger, A., Dommen, J., Weingartner, E., . . . Ristovski, Z. D. (2009). Analysis of the hygroscopic and volatile properties of ammonium sulphate seeded and unseeded SOA particles. *Atmospheric Chemistry and Physics, 9*(2), 721-732. doi:10.5194/acp-9-721-2009

Mircea, M., Facchini, M. C., Decesari, S., Cavalli, F., Emblico, L., Fuzzi, S., . . . Artaxo, P. (2005). Importance of the organic aerosol fraction for modeling aerosol hygroscopic growth and activation: a case study in the Amazon Basin. *Atmospheric Chemistry and Physics, 5*(11), 3111-3126. doi:10.5194/acp-5-3111-2005

Mircea, M., Facchini, M. C., Decesari, S., Fuzzi, S., & Charlson, R. J. (2002). The influence of the organic aerosol component on CCN supersaturation spectra for different aerosol types. *Tellus B, 54*(1), 74-81. doi:10.1034/j.1600-0889.2002.00256.x

Moore, R. H., Bahreini, R., Brock, C. A., Froyd, K. D., Cozic, J., Holloway, J. S., . . . Nenes, A. (2011). Hygroscopicity and composition of Alaskan Arctic CCN during April 2008. *Atmospheric Chemistry and Physics, 11*(22), 11807-11825. doi:10.5194/acp-11-11807-2011

Münkel, C., & Rasanen, J. (2004). New optical concept for commercial lidar ceilometers scanning the boundary layer. *Remote Sensing of Clouds and the Atmosphere IX*. doi:10.1117/12.565540

Münkel, C., Eresmaa, N., Räsänen, J., & Karppinen, A. (2006). Retrieval of mixing height and dust concentration with lidar ceilometer. *Boundary-Layer Meteorology, 124*(1), 117-128. doi:10.1007/s10546-006-9103-3

Murphy, S. M., Agrawal, H., Sorooshian, A., Padró, L. T., Gates, H., Hersey, S., . . . Seinfeld, J. H. (2009). Comprehensive Simultaneous Shipboard and Airborne Characterization of Exhaust from a Modern Container Ship at Sea. *Environmental Science & Technology, 43*(13), 4626-4640. doi:10.1021/es802413j

Nakao, S., Tang, P., Tang, X., Clark, C. H., Qi, L., Seo, E., . . . Cocker, D. (2013). Density and elemental ratios of secondary organic aerosol: Application of a density prediction method. *Atmospheric Environment, 68*, 273-277. doi:10.1016/j.atmosenv.2012.11.006

Nemesure, S., Wagener, R., & Schwartz, S. E. (1995). Direct shortwave forcing of climate by the anthropogenic sulfate aerosol: Sensitivity to particle size, composition, and relative humidity. *Journal of Geophysical Research, 100*(D12), 26105. doi:10.1029/95jd02897

Nemitz, E., Dorsey, J. R., Flynn, M. J., Gallagher, M. W., Hensen, A., Erisman, J., . . . Sutton, M. A. (2009). Aerosol fluxes and particle growth above managed grassland. *Biogeosciences, 6*(8), 1627-1645. doi:10.5194/bg-6-1627-2009

Padró, L. T., Moore, R. H., Zhang, X., Rastogi, N., Weber, R. J., & Nenes, A. (2012). Mixing state and compositional effects on CCN activity and droplet growth kinetics of size-resolved CCN in an urban environment. *Atmospheric Chemistry and Physics, 12*(21), 10239-10255. doi:10.5194/acp-12-10239-2012

Parworth, C., Fast, J., Mei, F., Shippert, T., Sivaraman, C., Tilp, A., . . . Zhang, Q. (2015). Long-term measurements of submicrometer aerosol chemistry at the Southern Great Plains (SGP) using an Aerosol Chemical Speciation Monitor (ACSM). *Atmospheric Environment, 106*, 43-55. doi:10.1016/j.atmosenv.2015.01.060

Peng, C., Chan, M. N., & Chan, C. K. (2001). The Hygroscopic Properties of Dicarboxylic and Multifunctional Acids: Measurements and UNIFAC Predictions. *Environmental Science & Technology, 35*(22), 4495-4501. doi:10.1021/es0107531

Peng, C., Jing, B., Guo, Y., Zhang, Y., & Ge, M. (2016). Hygroscopic Behavior of Multicomponent Aerosols Involving NaCl and Dicarboxylic Acids. *The Journal of Physical Chemistry A, 120*(7), 1029-1038. doi:10.1021/acs.jpca.5b09373

Pennington, M. R., Bzdek, B. R., Depalma, J. W., Smith, J. N., Kortelainen, A., Ruiz, L. H., . . . Johnston, M. V. (2013). Identification and quantification of particle growth channels during new particle formation. *Atmospheric Chemistry and Physics, 13*(20), 10215-10225. doi:10.5194/acp-13-10215-2013

Petters, M. D., & Kreidenweis, S. M. (2007). A single parameter representation of hygroscopic growth and cloud condensation nucleus activity. *Atmospheric Chemistry and Physics, 7*(8), 1961-1971. doi:10.5194/acp-7-1961-2007

Petters, M. D., Prenni, A. J., Kreidenweis, S. M., Demott, P. J., Matsunaga, A., Lim, Y. B., & Ziemann, P. J. (2006). Chemical aging and the hydrophobic-to-hydrophilic conversion of carbonaceous aerosol. *Geophysical Research Letters, 33*(24). doi:10.1029/2006gl027249

Pirjola, L., Laaksonen, A., Aalto, P., & Kulmala, M. (1998). Sulfate aerosol formation in the Arctic boundary layer. *Journal of Geophysical Research: Atmospheres, 103*(D7), 8309-8321. doi:10.1029/97jd03079

Porter, J. N., Lienert, B. R., Sharma, S. K., Lau, E., & Horton, K. (2003). Vertical and Horizontal Aerosol Scattering Fields over Bellows Beach, Oahu, during the SEAS Experiment*. *Journal of Atmospheric and Oceanic Technology, 20*(10), 1375-1387. doi:10.1175/1520-0426(2003)020<1375:vahasf>2.0.co;2

Prenni, A. J., Petters, M. D., Kreidenweis, S. M., Demott, P. J., & Ziemann, P. J. (2007). Cloud droplet activation of secondary organic aerosol. *Journal of Geophysical Research, 112*(D10). doi:10.1029/2006jd007963

Pruppacher, H. R., & Klett, J. D. (2011). *Microphysics of clouds and precipitation*. Dordrecht: Springer.

Quaas, J., Ming, Y., Menon, S., Takemura, T., Wang, M., Penner, J. E., . . . Schulz, M. (2009). Aerosol indirect effects – general circulation model inter-comparison and evaluation with satellite data. *Atmospheric Chemistry and Physics, 9*(22), 8697-8717. doi:10.5194/acp-9-8697-2009

Quinn, P. K., Bates, T. S., Coffman, D. J., & Covert, D. S. (2008). Influence of particle size and chemistry on the cloud nucleating properties of aerosols. *Atmospheric Chemistry and Physics, 8*(4), 1029-1042. doi:10.5194/acp-8-1029-2008

Raymond, T. M. (2002). Cloud activation of single-component organic aerosol particles. *Journal of Geophysical Research, 107*(D24). doi:10.1029/2002jd002159

Raymond, T. M. (2003). Formation of cloud droplets by multicomponent organic particles. *Journal of Geophysical Research, 108*(D15). doi:10.1029/2003jd003503

Rissler, J., Swietlicki, E., Zhou, J., Roberts, G., Andreae, M. O., Gatti, L. V., & Artaxo, P. (2004). Physical properties of the sub-micrometer aerosol over the Amazon rain forest during the wet-to-dry season transition - comparison of modeled and measured CCN concentrations. *Atmospheric Chemistry and Physics, 4*(8), 2119-2143. doi:10.5194/acp-4-2119-2004

Rissler, J., Vestin, A., Swietlicki, E., Fisch, G., Zhou, J., Artaxo, P., & Andreae, M. O. (2006). Size distribution and hygroscopic properties of aerosol particles from dry-season biomass burning in Amazonia. *Atmospheric Chemistry and Physics, 6*(2), 471-491. doi:10.5194/acp-6-471-2006

Roberts, G. C. (2002). Sensitivity of CCN spectra on chemical and physical properties of aerosol: A case study from the Amazon Basin. *Journal of Geophysical Research, 107*(D20). doi:10.1029/2001jd000583

Roberts, G. C., Day, D. A., Russell, L. M., Dunlea, E. J., Jimenez, J. L., Tomlinson, J. M., . . . Clarke, A. D. (2010). Characterization of particle cloud droplet activity and composition in the free troposphere and the boundary layer during INTEX-B. *Atmospheric Chemistry and Physics, 10*(14), 6627-6644. doi:10.5194/acp-10-6627-2010

Roberts, G., Mauger, G., Hadley, O., & Ramanathan, V. (2006). North American and Asian aerosols over the eastern Pacific Ocean and their role in regulating cloud condensation nuclei. *Journal of Geophysical Research, 111*(D13). doi:10.1029/2005jd006661

Rogers, R. R., & Yau, M. K. (1989). *A short course in cloud physics* (3rd ed.). Oxford: Butterworth-Heinemann.

Rose, D., Gunthe, S. S., Mikhailov, E., Frank, G. P., Dusek, U., Andreae, M. O., & Pöschl, U. (2008). Calibration and measurement uncertainties of a continuous-flow cloud condensation nuclei counter (DMT-CCNC): CCN activation of ammonium sulfate and sodium chloride aerosol particles in theory and experiment. *Atmospheric Chemistry and Physics, 8*(5), 1153-1179. doi:10.5194/acp-8-1153-2008

Rose, D., Nowak, A., Achtert, P., Wiedensohler, A., Hu, M., Shao, M., . . . Pöschl, U. (2010). Cloud condensation nuclei in polluted air and biomass burning smoke near the mega-city Guangzhou, China – Part 1: Size-resolved measurements and implications for the modeling of aerosol particle hygroscopicity and CCN activity. *Atmospheric Chemistry and Physics, 10*(7), 3365-3383. doi:10.5194/acp-10-3365-2010

Ross, K. E., Piketh, S. J., Bruintjes, R. T., Burger, R. P., Swap, R. J., & Annegarn, H. J. (2003). Spatial and seasonal variations in CCN distribution and the aerosol-CCN relationship over southern Africa. *Journal of Geophysical Research: Atmospheres, 108*(D13). doi:10.1029/2002jd002384

Russell, L. M., Flagan, R. C., & Seinfeld, J. H. (1995). Asymmetric Instrument Response Resulting from Mixing Effects in Accelerated DMA-CPC Measurements. *Aerosol Science and Technology, 23*(4), 491-509. doi:10.1080/02786829508965332

Saxena, P., & Hildemann, L. M. (1996). Water-soluble organics in atmospheric particles: A critical review of the literature and application of thermodynamics to

identify candidate compounds. *Journal of Atmospheric Chemistry, 24*(1), 57-109. doi:10.1007/bf00053823

Schaap, M., Loon, M. V., Brink, H. M., Dentener, F. J., & Builtjes, P. J. (2004). Secondary inorganic aerosol simulations for Europe with special attention to nitrate. *Atmospheric Chemistry and Physics, 4*(3), 857-874. doi:10.5194/acp-4-857-2004

Schäfer, K., Emeis, S., Junkermann, W., & Münkel, C. (2005). Evaluation of mixing layer height monitoring by ceilometer with SODAR and microlight aircraft measurements. *Remote Sensing of Clouds and the Atmosphere X, 5979*, 442-452. doi:10.1117/12.627932

Seinfeld, J. H., & Pandis, S. N. (2016). *Atmospheric chemistry and physics: from air pollution to climate change* (2nd ed.). Hoboken, NJ: John Wiley & Sons, Inc.

Sellegri, K., Umann, B., Hanke, M., & Arnold, F. (2005). Deployment of a ground-based CIMS apparatus for the detection of organic gases in the boreal forest during the QUEST campaign. *Atmospheric Chemistry and Physics, 5*(2), 357-372. doi:10.5194/acp-5-357-2005

Shantz, N. C., Leaitch, W. R., Phinney, L., Mozurkewich, M., & Toom-Sauntry, D. (2008). The effect of organic compounds on the growth rate of cloud droplets in marine and forest settings. *Atmospheric Chemistry and Physics, 8*(19), 5869-5887. doi:10.5194/acp-8-5869-2008

Shinozuka, Y., Clarke, A. D., Decarlo, P. F., Jimenez, J. L., Dunlea, E. J., Roberts, G. C., . . . Zhou, J. (2009). Aerosol optical properties relevant to regional remote sensing of CCN activity and links to their organic mass fraction: airborne observations over Central Mexico and the US West Coast during MILAGRO/INTEX-B. *Atmospheric Chemistry and Physics, 9*(18), 6727-6742. doi:10.5194/acp-9-6727-2009

Shulman, M. L., Jacobson, M. C., Carlson, R. J., Synovec, R. E., & Young, T. E. (1996). Dissolution behavior and surface tension effects of organic compounds in nucleating cloud droplets. *Geophysical Research Letters, 23*(3), 277-280. doi:10.1029/95gl03810

Sihto, S., Kulmala, M., Kerminen, V., Maso, M. D., Petäjä, T., Riipinen, I., . . . Lehtinen, K. E. (2006). Atmospheric sulphuric acid and aerosol formation: implications from atmospheric measurements for nucleation and early growth mechanisms. *Atmospheric Chemistry and Physics, 6*(12), 4079-4091. doi:10.5194/acp-6-4079-2006

Smith, J. N., Dunn, M. J., Vanreken, T. M., Iida, K., Stolzenburg, M. R., Mcmurry, P. H., & Huey, L. G. (2008). Chemical composition of atmospheric nanoparticles formed from nucleation in Tecamac, Mexico: Evidence for an important role for organic species in nanoparticle growth. *Geophysical Research Letters, 35*(4). doi:10.1029/2007gl032523

Stanier, C. O., Khlystov, A. Y., & Pandis, S. N. (2004). Nucleation Events During the Pittsburgh Air Quality Study: Description and Relation to Key Meteorological, Gas Phase, and Aerosol Parameters Special Issue of Aerosol Science and Technology on Findings from the Fine Particulate Matter Supersites Program. *Aerosol Science and Technology, 38*(Sup1), 253-264. doi:10.1080/02786820390229570

Steyn, D.G., M. Baldi, and R.M. Hoff, (1999). The Detection of Mixed Layer Depth and Entrainment Zone Thickness from Lidar Backscatter Profiles. *J. Atmos. Oceanic Technol.,* 16, 953–959, doi.org/10.1175/1520-0426(1999)016<0953:TDOMLD>2.0.CO;2

Stolzenburg, M. R. (1988). *An ultrafine aerosol size distribution measuring system* (Unpublished doctoral dissertation). University of Minnesota.

Stolzenburg, M. R., Mcmurry, P. H., Sakurai, H., Smith, J. N., Mauldin, R. L., Eisele, F. L., & Clement, C. F. (2005). Growth rates of freshly nucleated atmospheric particles in Atlanta. *Journal of Geophysical Research, 110*(D22). doi:10.1029/2005jd005935

Stroud, C. A., Nenes, A., Jimenez, J. L., Decarlo, P. F., Huffman, J. A., Bruintjes, R., . . . Nandi, S. (2007). Cloud Activating Properties of Aerosol Observed during CELTIC. *Journal of the Atmospheric Sciences, 64*(2), 441-459. doi:10.1175/jas3843.1

Stull, R. B. (1988). *An introduction to boundary layer meteorology*. Berlin: Springer.

Suni, T., Kulmala, M., Hirsikko, A., Bergman, T., Laakso, L., Aalto, P. P., . . . Tadros, C. (2008). Formation and characteristics of ions and charged aerosol particles in a native Australian Eucalypt forest. *Atmospheric Chemistry and Physics, 8*(1), 129-139. doi:10.5194/acp-8-129-2008

Svenningsson, B., Rissler, J., Swietlicki, E., Mircea, M., Bilde, M., Facchini, M. C., . . . Rosenørn, T. (2006). Hygroscopic growth and critical supersaturations for mixed aerosol particles of inorganic and organic compounds of atmospheric relevance. *Atmospheric Chemistry and Physics, 6*(7), 1937-1952. doi:10.5194/acp-6-1937-2006

Svenningsson, I. B., Hansson, H.-C., Wiedensohler, A., Ogren, J. A., Noone K. J., & Hallberg, A. (1992) Hygroscopic growth of aerosol particles in the Po Valley, Tellus B: Chemical and Physical Meteorology, *44*(5), 556-569, doi: 10.3402/tellusb.v44i5.15568

Swietlicki, E., Hansson, H., Hämeri, K., Svenningsson, B., Massling, A., Mcfiggans, G., . . . Kulmala, M. (2008). Hygroscopic properties of submicrometer atmospheric aerosol particles measured with H-TDMA instruments in various environments–a review. *Tellus B, 60*(3). doi:10.3402/tellusb.v60i3.16936

Swietlicki, E., Zhou, J., Covert, D. S., Hameri, K., Busch, B., Vakeva, M., . . . Stratmann, F. (2000). Hygroscopic properties of aerosol particles in the north-eastern Atlantic during ACE-2. *Tellus B, 52*(2), 201-227. doi:10.1034/j.1600-0889.2000.00036.x

Tang, I. N., & Munkelwitz, H. R. (1994). Water activities, densities, and refractive indices of aqueous sulfates and sodium nitrate droplets of atmospheric

importance. *Journal of Geophysical Research, 99*(D9), 18801-18,808. doi:10.1029/94jd01345

Tao, W., Chen, J., Li, Z., Wang, C., & Zhang, C. (2012). Impact of aerosols on convective clouds and precipitation. *Reviews of Geophysics, 50*(2). doi:10.1029/2011rg000369

Tjernström, M. (2007). Is There a Diurnal Cycle in the Summer Cloud-Capped Arctic Boundary Layer? *Journal of the Atmospheric Sciences, 64*(11), 3970-3986. doi:10.1175/2007jas2257.1

Tunved, P. (2006). High Natural Aerosol Loading over Boreal Forests. *Science, 312*(5771), 261-263. doi:10.1126/science.1123052

Twomey, S. (1959). The nuclei of natural cloud formation part II: The supersaturation in natural clouds and the variation of cloud droplet concentration. *Geofisica Pura e Applicata, 43*(1), 243-249. doi:10.1007/bf01993560

Vakkari, V., Laakso, H., Kulmala, M., Laaksonen, A., Mabaso, D., Molefe, M., . . . Laakso, L. (2011). New particle formation events in semi-clean South African savannah. *Atmospheric Chemistry and Physics, 11*(7), 3333-3346. doi:10.5194/acp-11-3333-2011

Vanreken, T. M. (2003). Toward aerosol/cloud condensation nuclei (CCN) closure during CRYSTAL-FACE. *Journal of Geophysical Research, 108*(D20). doi:10.1029/2003jd003582

Virkkula, A., Hirsikko, A., Vana, M., Aalto, P., Hillamo, R., & Kulmala, M. (2007). Charged Particle size distributions and analysis of particle formation events at the Finnish Antarctic research station Aboa. *Boreal Environment Research, 12*(3), 397-408.

Wang, J., Cubison, M. J., Aiken, A. C., Jimenez, J. L., & Collins, D. R. (2010). The importance of aerosol mixing state and size-resolved composition on CCN concentration

and the variation of the importance with atmospheric aging of aerosols. *Atmospheric Chemistry and Physics Discussions, 10*(5), 11751-11793. doi:10.5194/acpd-10-11751-2010

Wang, J., Lee, Y., Daum, P. H., Jayne, J., & Alexander, M. L. (2008). Effects of aerosol organics on cloud condensation nucleus (CCN) concentration and first indirect aerosol effect. *Atmospheric Chemistry and Physics Discussions, 8*(3), 9783-9818. doi:10.5194/acpd-8-9783-2008

Wang, M., Ghan, S., Ovchinnikov, M., Liu, X., Easter, R., Kassianov, E., . . . Morrison, H. (2011). Aerosol indirect effects in a multi-scale aerosol-climate model PNNL-MMF. *Atmospheric Chemistry and Physics Discussions, 11*(1), 3399-3459. doi:10.5194/acpd-11-3399-2011

Wang, X. Y., & Wang, K. C. (2014). Estimation of atmospheric mixing layer height from radiosonde data. *Atmospheric Measurement Techniques, 7*(6), 1701-1709. doi:10.5194/amt-7-1701-2014

Weber, R. J., Marti, J. J., Mcmurry, P. H., Eisele, F. L., Tanner, D. J., & Jefferson, A. (1997). Measurements of new particle formation and ultrafine particle growth rates at a clean continental site. *Journal of Geophysical Research: Atmospheres, 102*(D4), 4375-4385. doi:10.1029/96jd03656

Weber, R. J., Mcmurry, P. H., Mauldin, L., Tanner, D. J., Eisele, F. L., Brechtel, F. J., . . . Baumgardner, D. (1998). A study of new particle formation and growth involving biogenic and trace gas species measured during ACE 1. *Journal of Geophysical Research: Atmospheres, 103*(D13), 16385-16396. doi:10.1029/97jd02465

Wiscombe, W. J., & Grams, G. W. (1976). The Backscattered Fraction in two-stream Approximations. *Journal of the Atmospheric Sciences, 33*(12), 2440-2451. doi:10.1175/1520-0469(1976)033<2440:tbfits>2.0.co;2

Wulfmeyer, V. (1999). Investigation of Turbulent Processes in the Lower Troposphere with Water Vapor DIAL and Radar–RASS. *Journal of the Atmospheric Sciences, 56*(8), 1055-1076. doi:10.1175/1520-0469(1999)056<1055:iotpit>2.0.co;2

Yli-Juuti, T., Nieminen, T., Hirsikko, A., Aalto, P. P., Asmi, E., Hõrrak, U., . . . Riipinen, I. (2011). Growth rates of nucleation mode particles in Hyytiälä during 2003−2009: variation with particle size, season, data analysis method and ambient conditions. *Atmospheric Chemistry and Physics, 11*(24), 12865-12886. doi:10.5194/acp-11-12865-2011

Zappoli, S., Andracchio, A., Fuzzi, S., Facchini, M., Gelencsér, A., Kiss, G., . . . Zebühr, Y. (1999). Inorganic, organic and macromolecular components of fine aerosol in different areas of Europe in relation to their water solubility. *Atmospheric Environment, 33*(17), 2733-2743. doi:10.1016/s1352-2310(98)00362-8

Zeng, X., Brunke, M. A., Zhou, M., Fairall, C., Bond, N. A., & Lenschow, D. H. (2004). Marine Atmospheric Boundary Layer Height over the Eastern Pacific: Data Analysis and Model Evaluation. *Journal of Climate, 17*(21), 4159-4170. doi:10.1175/jcli3190.1

Zhang, R., Khalizov, A., Wang, L., Hu, M., & Xu, W. (2011). Nucleation and Growth of Nanoparticles in the Atmosphere. *Cheical Reviews, 123*(3), 1957-2011. doi: 10.1021/cr2001756

Zhang, X., Mcmurray, P., Hering, S., & Casuccio, G. (1993). Mixing characteristics and water content of submicron aerosols measured in Los Angeles and at the Grand Canyon. *Atmospheric Environment. Part A. General Topics, 27*(10), 1593-1607. doi:10.1016/0960-1686(93)90159-v

Zheng, J., Hu, M., Zhang, R., Yue, D., Wang, Z., Guo, S., . . . Zhu, T. (2011). Measurements of gaseous $H_2SO_4$ by AP-ID-CIMS during CAREBeijing 2008 Campaign. *Atmospheric Chemistry and Physics Discussions, 11*(2), 5019-5042. doi:10.5194/acpd-11-5019-2011